The Convective Desalination of Sea Ice

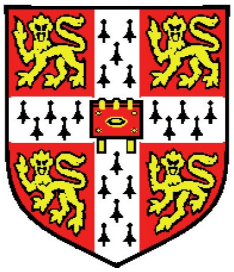

David W. Rees Jones

Christ's College

University of Cambridge

This dissertation is submitted for the degree of

Doctor of Philosophy

December 2013

This dissertation is the result of my own work and includes nothing which is the outcome of work done in collaboration except where specifically indicated in the text.

David W. Rees Jones

The Convective Desalination of Sea Ice

David W. Rees Jones

This thesis aims to improve our understanding of the fundamental processes affecting the growth of sea ice in the polar oceans in order to improve climate models. Newly formed sea ice contains a significant amount of salt as liquid brine in the interstices of an ice matrix. My focus is on one of the processes by which the salt content of sea ice decreases, namely *convective desalination*, which is also often called gravity drainage by geophysicists.

Modelling convective desalination requires an understanding not only of the thermodynamics of sea-ice growth but also of its internal fluid dynamics. This thesis considers a class of physical systems called mushy layers, of which sea ice is an example. Mushy layers are multi-component systems consisting of a porous matrix of solid phase whose interstices contain the same substance in the liquid phase. I develop a mathematical description of these systems in terms the of mushy-layer equations and explore the appropriate boundary conditions at a mush–liquid interface.

I develop a simple Chimney-Active-Passive (CAP) model of convection in mushy layers for arrays of liquid chimneys in two and three dimensions. This allows the interstitial fluid flow and salt flux from the mushy layer to be determined in terms of the dimensionless parameters of the system. I discuss important mathematical and physical aspects of the CAP model.

I then explain the physics of gravity drainage from sea ice, elucidating the connection between downward flow through liquid brine channels (chimneys) and a convective upwelling in the rest of the ice that is sustained by horizontal density differences and provides the fluid to replace that which drains from the ice. I use the CAP model to determine the convective upwelling velocity mathematically, deriving a new, physical parameterization of gravity drainage. I test my predictions by investigating previous laboratory observations of the propagation of dye fronts.

Finally, I take a one-dimensional, thermodynamic sea-ice model of the kind currently used in coupled climate models and parameterize convective desalination using the CAP model. The parameterization allows determination of physical properties and salt fluxes from sea ice dynamically, corresponding to the calculated, evolving salinity of the sea ice, in contrast to older, established models that prescribe a fixed salinity. I find substantial differences compared to previous models, particularly in terms of predicted salt fluxes from sea ice. I explain the likely implications and potential advantages of my parameterization for climate models.

Acknowledgements

Firstly, I would like to thank my supervisor, Grae Worster, for his encouragement, wisdom and support throughout my PhD, and for his emphasis on clear exposition. Secondly, I very much appreciated the stimulating atmosphere of the ITG and DAMTP; among others, I enjoying working with John Lister, Jerome Neufeld and Duncan Hewitt, with whom I shared a lively office as well as the study of convection in a porous medium. Finally, I would like to acknowledge the practical and financial support provided by the department and my college, Christ's.

The breath of God produces ice,
and the broad waters become frozen. (Job 37:10)

Contents

Chapter 1

Overview

'Out of sight, out of mind'? Sea ice is far removed from substantial human settlement. But though confined to the most extreme latitudes and temperatures on Earth, sea ice is a dynamically evolving feature of the polar regions. Formed at the interface between ocean and atmosphere, sea ice regulates the transfer of heat between these two principal components of the physical climate system. Evolving in space and time, sea ice has thermal and mechanical properties that must be updated dynamically for a faithful representation within climate models. Such models are vital tools to help people everywhere predict, avoid and mitigate the risks of climate change. Therefore, sea ice has profound implications, not only for those living in the polar regions, but also for those living anywhere on Earth. For example, recent changes in the Arctic sea ice have been associated with unusual weather patterns in European summers (Screen, 2013). Furthermore, the seasonal growth and retreat of sea ice causes massive salt fluxes into the seawater beneath. Salt fluxes cause ocean mixing and are a vital driver of the circulation of the Earth's ocean, which in turn affects the climate of the whole Earth. Sea-ice formation causes the Labrador Current, for example, which in part drives the North Atlantic Circulation, including the Gulf Stream). It also causes Antarctic Bottom Water to form, which lies at the bottom of all the major oceans.

Indeed, in terms of climate change caused by changes in greenhouse gases, the 'Arctic amplification,' in which temperatures in the Arctic rise faster than the global average, means that this region has offered an early warning of the potential impact of a changing climate. The summer ice cover has been retreating markedly,

and apparently at an accelerating rate (Comiso *et al.*, 2008), leading to a much greater proportion of first-year ice. This robust feature of climate models and the observational record over the last three decades is driven by anthropogenic greenhouse gas emissions (Notz & Marotzke, 2012) and is linked to feedbacks involving sea ice and snow cover (Holland & Bitz, 2003; Screen & Simmonds, 2010), providing a strong motivation to study sea-ice processes. Interestingly, this picture is not replicated in the Antarctic, where the ice cover has expanded modestly, indicating that other processes (such as changes in the winds) can cause different patterns of variation in the two hemispheres (Holland & Kwok, 2012).

To address the challenges of sea-ice modelling, this thesis considers a wider class of physical systems called mushy layers, of which sea ice is a particular example. Mushy layers are multiphase systems consisting of a reactive porous matrix of solid phase whose interstices contain the same substance in the liquid phase. We develop a mathematical description of these systems in terms of governing equations derived from fundamental physics, and use it to model processes of interest to polar geophysics.

Newly formed sea ice contains a significant amount of salt as liquid brine in the interstices of the ice matrix, which is essentially pure frozen water. The salt content of sea ice is observed to decrease over time because of a variety of processes. Our focus is on one of these processes called 'convective desalination,' which is often called gravity drainage by geophysicists. Modelling this process requires an understanding not only of the thermodynamics of sea-ice growth, but also of its internal fluid dynamics.

Chapter 2 explains motivations for sea-ice modelling, particularly focusing on the interactions between sea ice and the physical climate of the polar regions. These interactions can be both direct and indirect, and give rise to both positive and negative feedbacks to changes in the polar climate, which we discuss in light of the significant observed changes and predicted future changes. Related to this, we review the significance of sea ice to coupled climate models, and discuss current modelling approaches. This survey of the field highlights the need to develop a simple, physically based parameterization of convective desalination for sea-ice models.

Mushy-layer theory (chapter 3) provides the mathematical framework for

modelling multiphase systems, such as sea ice. It adopts a continuum approach, averaging physical variables over a representative (control) volume containing both solid ice and liquid brine. Although sea ice contains a large number of different dissolved salts, for many purposes it can be thought of as a two-component system, called a binary alloy within mushy-layer theory. We derive continuum equations for mass, heat, salt and momentum conservation and explore simpler, idealized versions of these equations relevant to the convective desalination of sea ice. The boundary conditions of these governing equations are often subtle and depend on the interstitial fluid flow and whether the mushy layer is freezing or melting. Therefore, we consider a simple, forced corner-flow configuration that allows us to exhibit each possible type of boundary condition and explore the physical relevance of these to subsequent work.

Convective desalination of sea ice is associated with the formation of liquid brine channels. These narrow, approximately vertical structures are examples of a general feature of convecting mushy layers which, in that context, are called chimneys. In chapter 4 we develop a new, simple model of convection in a mushy layer. The key insight is that we can describe a mushy layer in terms of a liquid *chimney* (in which the flow can be determined analytically), an *active* region in which the horizontal density gradient drives a convective flow and a *passive* region that essentially supplies the fluid that replaces the fluid that drains from the ice through chimneys. These simplifications give rise to the *Chimney-Active-Passive* (CAP) model, and we proceed to apply the model to regular arrays of chimneys in two and three dimensions. This allows the interstitial fluid flow and salt flux from the mushy layer to be determined in terms of the dimensionless parameters of the system.

The CAP model has a number of interesting features. Exploring the mathematical structure of the model in more detail yields important, general physical insights. In chapter 5, we consider an isolated chimney in an infinite mushy layer. We derive boundary-layer solutions that are closely related to the active region of the CAP model and explain why a boundary-layer model alone cannot describe all of the essential physics of mushy-layer convection. Secondly, we examine the existence and uniqueness of the solutions of the equations governing the CAP model. This study shows more precisely why exactly we need an active region

coupled to a passive region in order to describe properly convection. Finally, we find a complete asymptotic solution of the CAP model in the limit of large latent heat. This acts as a helpful test of our model and allows us to clarify the role of latent heat in mushy-layer convection.

While the previous chapters are deliberately general, in chapter 6 we begin to apply this general framework to understand gravity drainage in sea ice. We discuss various mechanisms by which sea ice desalinates and explain our focus on gravity drainage in the context of physical arguments and previous studies. We explain the physics of gravity drainage, elucidating the connection between downward flow through liquid brine channels and a convective upwelling in the rest of the ice that is sustained by horizontal density differences and provides the fluid to replace that which drains from the ice. We use the CAP model to determine the convective upwelling velocity mathematically, deriving a new, physical parameterization of this process in terms of two tuning parameters. In using the CAP model, we are translating an idealized, steady result to the transient situation of sea-ice growth. We test our predictions by investigating the experiments of Eide & Martin (1975) and Chen (1995), explaining previously unexplained features of these.

Having determined the convective upwelling velocity associated with gravity drainage of sea ice, we use this to determine the evolution of the salinity field of sea ice in a one-dimensional, thermodynamic model of sea-ice growth. In chapter 7, we develop such a model in the context of previous thermodynamic sea-ice models, namely those based on Maykut & Untersteiner (1971) that prescribe, rather than determine, the salinity field. We use mushy-layer theory to derive the governing equations and the CAP model to parameterize convection. We discuss and provide details of the numerical approach adopted. Finally, we present a broad suite of results in situations relevant to laboratory tank experiments in order to test our model. We consider the difference between fixed and variable-chill cooling and analyse the behaviour of our model. An emerging pattern of discrepancies between theory and experiments suggests a weakness in the candidate porosity–permeability relationship, and we seek to resolve this question by analysing a wider class of experimental results.

CICE: the Los Alamos Sea Ice Model (Hunke & Lipscomb, 2008) is a widely-

used example of a fixed-salinity sea-ice model based on Maykut & Untersteiner (1971) via Bitz & Lipscomb (1999). Therefore, in chapter 8, we compare their governing equations with those derived from mushy-layer theory presented in the previous chapter, as well as alternative definitions of salt flux. We compare the predictions of fixed-salinity models with our new dynamic-salinity model, for growth into a finite tank and an infinite ocean. We also investigate theoretically the dependence of sea-ice thickness on sea-ice salinity. These studies allow us to investigate the likely implications for climate models of incorporating our dynamic-salinity model of sea ice in terms of sea-ice thickness and salt fluxes.

In chapter 9 we draw these themes together, synthesising the principal conclusions from the previous chapters, reflecting on the issues posed at the outset of this thesis, and outlining the likely implications of our research and major research questions that remain to be addressed in this field.

Chapter 2

Sea-Ice Modelling

2.1 Sea ice and the polar climate

In the depths of the polar winter, vast tracts of the ocean freeze, forming or thickening a layer of sea ice. This seasonal cycle brings substantial changes to both the Arctic Ocean and the seas surrounding Antarctica. In the Arctic Ocean, for instance, at its September minimum, the areal extent of the sea ice is some 5 million square kilometres, while at its March maximum, the ice covers some 15 million square kilometres. On top of this strong seasonal variation, there is a trend towards lower areal extent (especially in the summer) on a decadal timescale, associated with global climate change (reviewed in Weeks, 2010). The recent indications are that this trend is accelerating (Comiso *et al.*, 2008), which leads us to expect that the proportion of first-year ice (ice that is newly frozen in a given year) in the future will continue to rise. Since a substantial proportion of the ice is new each year, any change in the atmospheric and ocean conditions could lead to rapid change in the amount of sea ice. Therefore, sea ice is an important, sensitive and changing component of the polar climate system.

Sea ice differs from lake ice in that it is formed from saltwater and, as the ice freezes, a porous matrix forms in which saltwater remains within the interstices of the solid ice (shown in darker grey in figure 2.1). Therefore, sea ice is a multiphase system.

Both sea and lake ice can, in some sense, be grown in the laboratory: in the

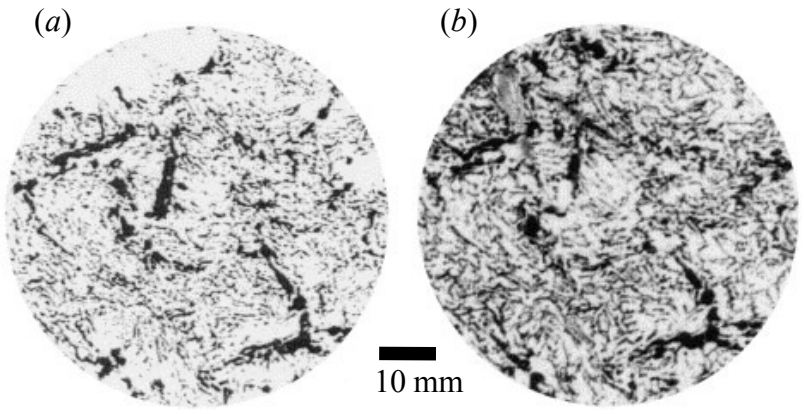

Figure 2.1: The porous nature of sea ice, adapted from Eicken *et al.* (2000), showing (in darker grey) liquid pores in a horizontal cross section of sea ice, both as a visual image (a) and as an MRI image (b).

former case by freezing a solution containing certain salts (principally sodium chloride, but also magnesium chloride, magnesium sulphate, calcium sulphate and potassium sulphate, and trace amounts of others) in proportions relevant to the polar oceans (Neumann, 1966). However, there is an important sense in which the resulting ice would not be sea ice. (Neither, for that matter, would the resulting fresh ice be lake ice.) For sea ice forms in a particular physical context, the Earth's polar oceans, and as such does not exist independently of the climate and geography of these regions. Thus in this chapter we focus on the geophysical context, as this shapes the applicability and likely impact of our new model of sea ice. Then in subsequent chapters, we use general theory and analogue laboratory experiments to develop physically consistent models of sea ice.

2.1.1 The Arctic and Antarctic

The combination of thermal forcing and atmospheric dynamics (McIntyre, 2000) causes the frigid temperatures required for sea-ice formation in the winter. In this respect, the Arctic and Antarctic share a fundamental similarity. However, in many ways the poles differ as much from each other as from more temperate latitudes.

Perhaps the most immediate way to appreciate this difference is to compare maps of the two regions, as shown in figures 2.2 and 2.3. These bathymetric maps are adapted from GEBCO, the General Bathymetric Chart of the Oceans. As an aside, it is interesting to note that the details of these maps are incomplete and there is an ongoing international effort to integrate different data sources consistently and fill gaps in coverage. This effort has resulted in the International Bathymetric Chart of the Arctic Ocean (IBCAO) and the forthcoming International Bathymetric Chart of the Southern Ocean (IBSCO) (see, respectively, Jakobsson *et al.*, 2012; Arndt & Schenke, 2012). Indeed, recent advances are not limited to mapping: the development of satellite technology has greatly increased our knowledge of sea ice and this should open the possibility of new data to test sea-ice models.

Antarctica is a frozen continent, covered by massive ice sheets of 14×10^6 km^2, ringed by the Southern Ocean. By contrast, the Arctic is an ocean basin, covered seasonally by sea ice, ringed (incompletely) by the North American and Eurasian continents. These differences affect not only how sea ice forms, but also the influence of the formation and melting of sea ice on the climates of these different regions.

The central Arctic basin itself covers some 12×10^6 km^2, divided into the deep Canadian and Eurasian sub-basins by the relatively shallow Lomonosov ridge. The Eurasian basin is fringed by a wide continental shelf (600–800 km) while the Canadian basin has only a narrow shelf. Although there are a number of inlets to the Arctic basin, Fram Strait (2600 m deep, 600 km wide) is the sole deep inlet; apart from this inlet, the basin is effectively landlocked.

The exchange flow through Fram Strait comprises the northerly West Spitzbergen Current (WSC) and the southerly East Greenland Current (EGC). These currents interact with sea ice directly and indirectly. In particular, the EGC transports a large volume of sea ice into the Atlantic Ocean (2200 km^3 per year on average in the 1990s, Kwok *et al.* (2004), although the older estimate of Aagaard & Carmack (1989) is higher) and the WSC transports relatively warm, salty water from the Atlantic Ocean (called Atlantic Water, AW) into the Arctic. This AW feeds a layer of water (the Atlantic layer) that lies between surface water layer (Polar Water, PW) up to 200 m depth and the deep water beneath about

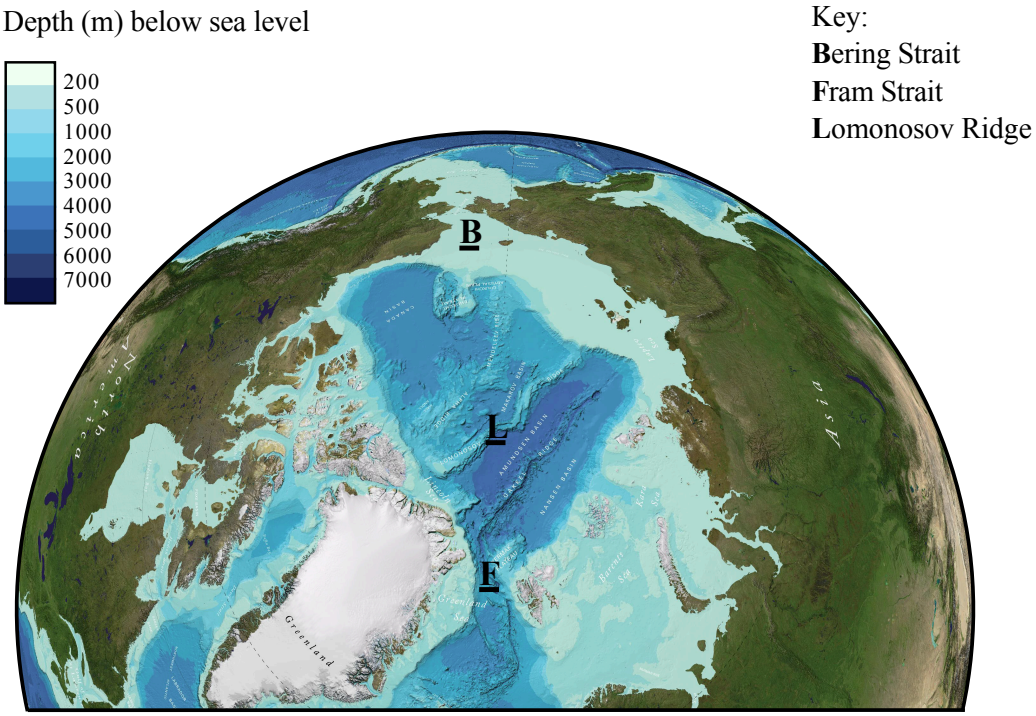

Figure 2.2: The bathymetry of the Arctic Ocean, adapted from GEBCO, the General Bathymetric Chart of the Oceans, `www.gebco.net/general_interest/bathymetry_visualisations.html`, as is figure 2.3. The narrow Lomonosov Ridge separates the Canadian basin from the Eurasian basin. The only deep inlet to the Arctic basin, Fram Strait, lies to the east of Greenland. At the opposite side of the basin, the Bering Strait provides a narrow inlet.

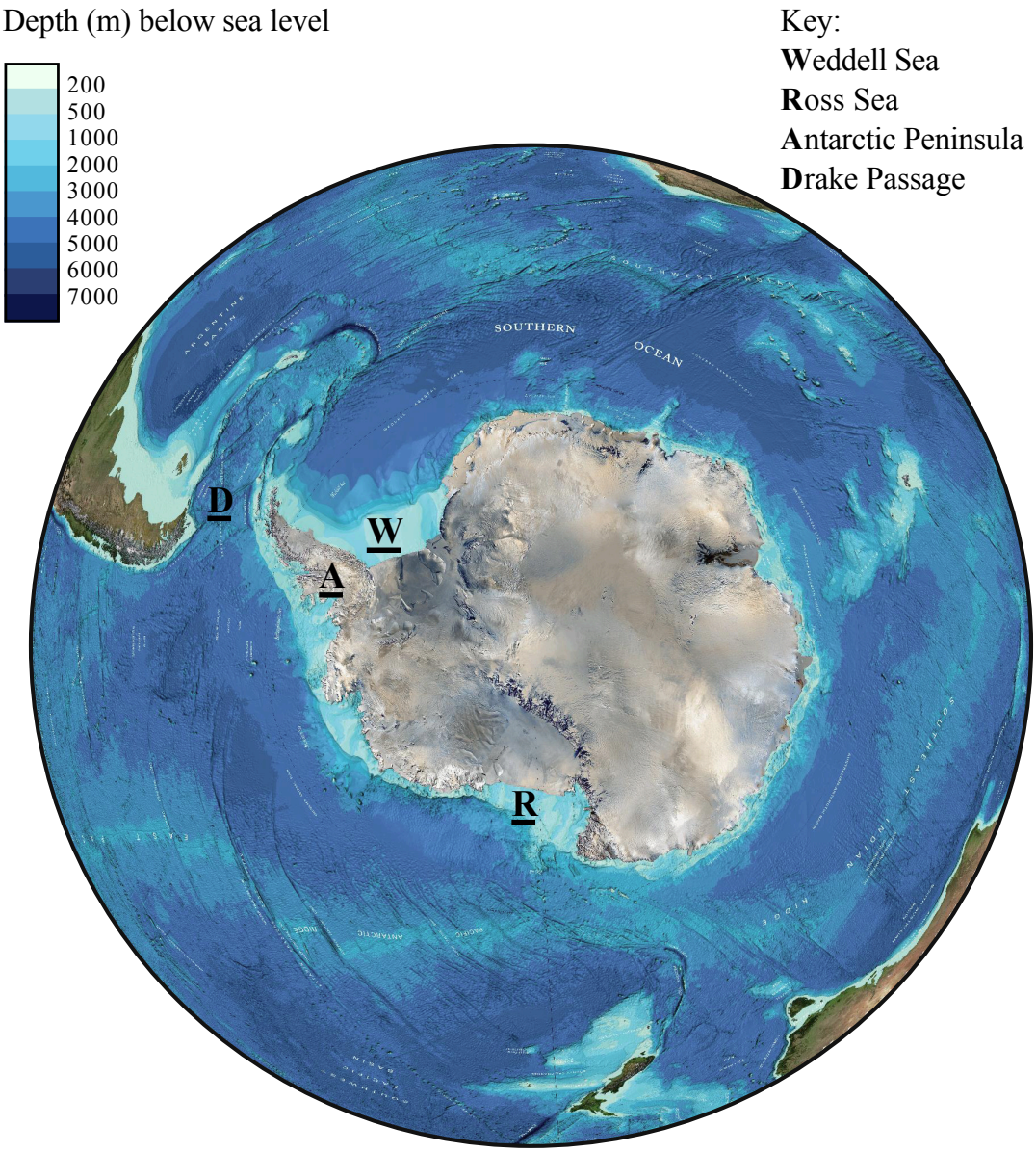

Figure 2.3: The bathymetry of the Southern Ocean around Antarctica. The Weddell and Ross Seas, partially covered by the Ronne-Filchner Ice Shelf and Ross Ice Shelf respectively, are also covered with sea ice in the winter and are significant regions of bottom-water formation. The interaction of Antarctic Circumpolar Current (ACC) with the shelf and the presence of a coastal countercurrent (driven by coastal low pressure weather systems) establishes gyres within these seas that transport sea ice. The Antarctic Peninsula extends from around 74–63°S and causes the ACC to divert northwards through Drake Passage.

800m (Coachman & Aagaard, 1974). As the WSC flows northward, it plunges under the surface due to cooling from the atmosphere and the melting of sea ice in that region. Together with the high salinity of AW compared to PW, which is freshened by inputs from several large rivers as well as a small, relatively fresh inflow through the Bering Strait, this establishes a very stable stratification in the Arctic Ocean (*e.g.* Perkin & Lewis, 1984; Cokelet *et al.*, 2008). This stratification inhibits vertical mixing and so reduces the convective heat flux from the warm Atlantic layer to the surface layer, which would otherwise inhibit sea-ice formation.

The effectively landlocked nature of the Arctic basin affects the transport of sea ice within it. At least historically, it permitted a significant region of old pack ice to persist through several summer-melt cycles at the highest latitudes, especially off the north coast of Greenland and the islands of the Canadian Arctic. This ice would drift slowly under the cyclonic action of the Beaufort Gyre before being exported through Fram Strait. Recent reductions in the extent of sea ice are associated with a reduction in this so-called 'multi-year ice' (ice that persists over more than one season) and we return to the subject of the changing climate as this motivates much of the interest in sea-ice processes, including convective desalination.

The Antarctic is something of a mirror image. The Antarctic continent is surrounded by the circumpolar Southern Ocean, which covers some 35×10^6 km^2. The topography of this ocean is far from simple, as shown by figure 2.3. The Ross and Weddell Seas, which are the only significant regions of continental shelf, lie at the terminus of ice shelves and seem to be responsible for large amount of marine ice formation in the form of platelet (frazil) ice. Strong katabatic winds maintain open water polynyas that also contribute to rapid ice formation, since there is minimal insulation between ocean and atmosphere from existing ice. However, gyres within these seas circulate ice within them and then further northwards, out to sea, which contributes to their melting and leads to even less persistence of multi-year ice than in the Arctic.

The complex topography also affects the ocean currents around Antarctica. In particular, the Antarctic Circumpolar Current (ACC), driven by very strong westerly winds below the coastal latitudes, splits into multiple jets and is partially

blocked by the Antarctic Peninsula. This current is far stronger – tens of times stronger according to the estimates of Weeks (2010) – than the WSC and EGC in the Arctic and is of great significance to the global climate as it transports momentum, salt and heat and is connected to all the oceans of the Earth (Nowlin & Klinck, 1986).

Many important features of the water masses of the Southern Ocean are long established. Sverdrup *et al.* (1942) summarizes these elegantly and we reproduce his summary diagram in figure 2.4. As we have seen, there is substantial sea-ice formation on the continental shelves, and the segregated brine and cold air temperatures combine to create a layer of extremely dense Antarctic Bottom Water (AABW) that mixes to some extent with deep water before flowing out under each of the Earth's oceans, giving rise to a very stable stratification that, to some extent, inhibits mixing.

In conclusion, the contrasting geography of Antarctica results in an even greater seasonal cycle, with ice cover varying from 3–18$\times 10^6$ km^2. At both poles, the strong (increasingly strong in the Arctic) seasonal cycle means that processes affecting first-year ice need to be modelled carefully.

2.1.2 Interactions between sea ice and the physical climate

Sea ice interacts with the main components of the Earth's physical climate system – the ocean and the atmosphere – in a number of important ways. Although only a few meters thick, sea ice plays an important role in the climate system since it has a higher albedo than open water, insulates the polar oceans, and stores latent heat (reviewed in Weeks, 2010). In particular, the albedo (which characterizes the proportion of the sun's radiation that is reflected) of open ocean is less than 0.1, whereas it is 0.5–0.7 for sea ice and even higher (0.75–0.85) for snow-covered ice (Perovich, 1996). Due to the insulating effect of the ice, the net heat flux to the atmosphere can be 1–2 orders of magnitude greater for open water or very thin ice compared to multi-year ice (Maykut, 1978). Thus, in the winter, the atmosphere can be substantially colder than the upper layer of the ocean. Furthermore, the high latent heat capacity is such that it requires about 300J to

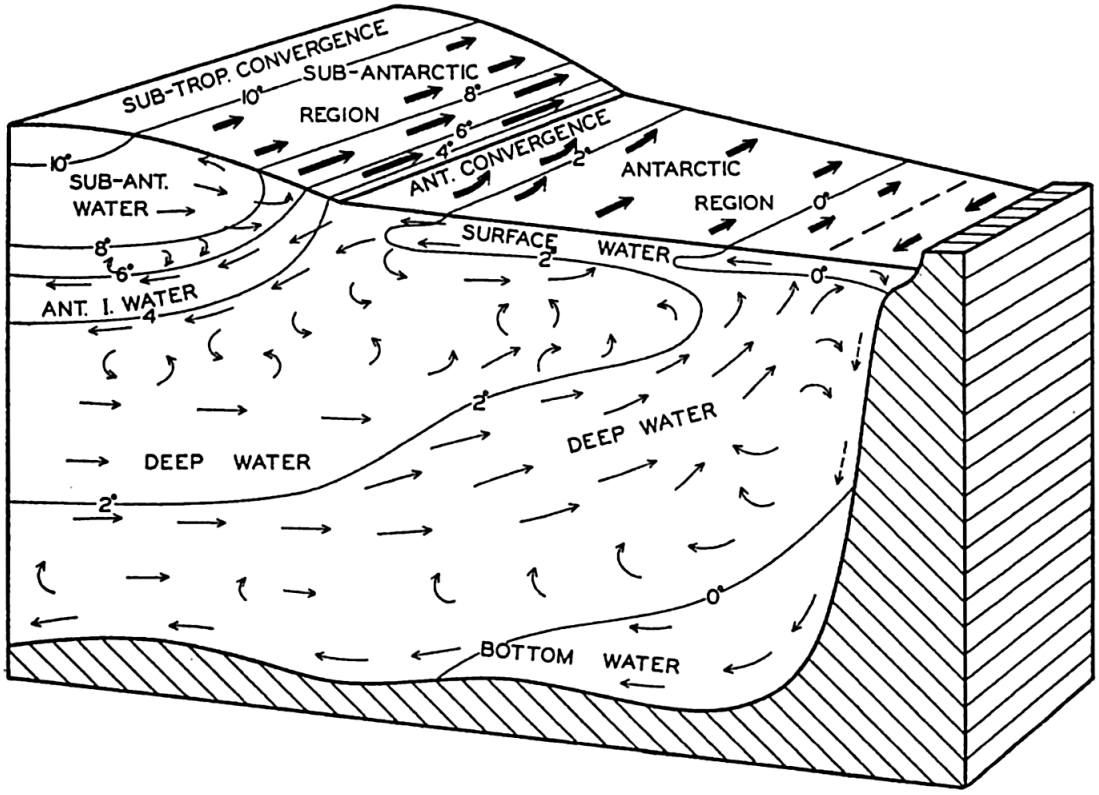

Figure 2.4: From Sverdrup *et al.* (1942): the currents and water masses of the Antarctic regions. The contours are isotherms of 0–10°C in increments of 2°C. Note particular that the region of sub-zero water near the coast of Antarctica on the right of the figure is a region of strong ice production, which leads to the production of bottom water, indicated by the dashed arrows.

melt a cubic centimetre of ice, whereas it requires just 2J to raise the temperature of a cubic centimetre of ice by one degree Celsius, or 4J for water (*cf.* table 7.1).

When the ice begins to melt and open water returns, polar waters absorb more radiation, leading to further warming and melting of the ice. The reverse occurs during the polar winter. This feedback mechanism could potentially lead to accelerated global climate change and so must be carefully modelled. However, there is some evidence from experiments conducted on climate models that the damping effect of ice insulation (in which thinner ice increases thermal heat transfer by conduction and so increases ice production) can lead to sea-ice recovery (Tietsche *et al.*, 2011).

The formation of sea ice is also an important driver of the thermohaline circulation of the oceans. When ice forms from saltwater, water is preferentially incorporated into the solid phase relative to salt, a process called segregation. The rejected salt causes an increase in the density of sea water where ice forms, leading to downward flow (see the discussion of AABW above, although in the Arctic the downward flow typically penetrates only the upper PW). Globally, the vertical transport of salt downwards, matched by mixing in lower latitudes, is an integral part of thermohaline circulation. Regionally, it is a crucial salt flux for the polar oceans, comparable to the (negative) salt fluxes from rivers and ice-sheet melting, and drives vertical mixing of the upper layer of the ocean. The surface salt flux from sea ice has been measured to be as high as 1–2 kg/m^2/day for new ice (Notz & Worster, 2008). Salt fluxes are known to be sensitive to short-term changes in the external forcing (Widell *et al.*, 2006; Jardon *et al.*, 2013). Consequently, the representation of salt fluxes significantly affects the salinity structure of the ocean in climate models (Vancoppenolle *et al.*, 2005, 2009*b*). Indeed, modelling the Arctic halocline (a cold layer with a strong salinity gradient) is a persistent problem in climate models (Holloway *et al.*, 2007) and seems to be connected with modelling how salt fluxes from sea ice mix the ocean (Nguyen *et al.*, 2009).

We seek to understand the flux of cold salty water from growing sea ice caused by segregation. This does not happen instantaneously, at the interface between the ice and ocean, as new ice forms. Instead sea ice is a porous medium (see figure 2.1) and the bulk-salinity field is continuous across the ice–ocean interface (Notz &

Worster, 2008). However, the brine in the pores of the ice becomes increasingly salty as the water continues to solidify, which creates a compositional density gradient that can drive convection within and out of the ice, through liquid brine channels. Of the mechanisms for salt fluxes from sea ice described by Untersteiner (1968), convection within the ice called 'gravity drainage' is dominant, at least during the winter growth season (Notz & Worster, 2009), as we discuss in chapter 6. However, this dynamic process is inadequately represented in current models of sea ice. We aim to address this deficiency by developing a simple, cheap-to-implement model in chapter 7.

While our research is principally concerned with the physical aspects of sea ice, increasingly the physical climate is being considered as part of a broader 'Earth system' that also incorporates biological and chemical elements, such as in the Community Earth System Model (Hurrell *et al.*, 2013). The polar oceans are a rich region for primary production and the role that sea ice plays in this biosphere is an area of active research. It seems that the liquid channels within the ice itself are important habitats for various algae because of their high salinity and nutrient content and convective desalination may help to supply the nutrients that sustain primary production – so our work is likely to have impacts beyond the physical climate.

2.2 Challenges in sea-ice modelling

Sea ice forms a dynamic interface between the ocean and atmosphere, and so constitutes an integral aspect of any coupled climate model (Gent, 2012). As we have seen, it plays a significant role in the climate of the polar regions.

Within coupled climate models, sea ice is typically accounted for by using a small modelling component that is coupled to ocean and atmosphere models. The sea-ice component accounts for the thermodynamic growth and melting of ice, the movement of ice due to wind stress, its response to internal stresses, lateral melting and the formation of pressure ridges (*e.g.* Hunke & Lipscomb, 2008; Vancoppenolle *et al.*, 2009*a*,*b*). In this thesis, we restrict attention to the thermodynamic growth of ice and analyze the one-dimensional thermodynamic model of ice growth that calculates the change of an ice-thickness distribution.

Thermodynamic growth accounts for much of the change at the thin-ice end of this distribution, which is particularly important for salt fluxes, as these are much stronger for thinner ice.

In models derived from Maykut & Untersteiner (1971), including Bitz & Lipscomb (1999) which is used in CICE: the Los Alamos Sea Ice Model (Hunke & Lipscomb, 2008), thermodynamic growth is determined by solving an equation for conservation of heat within sea ice

$$\overline{c}\frac{\partial T}{\partial t} = \frac{\partial}{\partial z}\left(\overline{k}\frac{\partial T}{\partial z}\right) - \frac{\partial}{\partial z}F_{\mathrm{rad}}, \tag{2.1}$$

in which the thermal properties of ice, its heat capacity $\overline{c}$ and conductivity $\overline{k}$, depend on the temperature T and bulk salinity S of the ice. Here, and throughout this thesis, I use 'ice' to refer to porous sea ice containing both liquid brine and solid (pure water) ice. F_{rad} is the flux of penetrating solar radiation. Thus the thermal properties of sea ice are composed of those of the solid and liquid phases that make up sea ice. Fixed-salinity models used in older, established sea-ice models are deficient in that, while the temperature is determined as part of the solution, the bulk salinity is prescribed. A further potential deficiency arises in that the thermodynamic properties of sea ice depend only indirectly on ice salinity; rather, they depend directly on the fraction of solid ice, which depends on ice salinity.

In prescribing S, it is common to choose a fixed value or profile with low salinity more appropriate to multi-year ice. For instance, in version 4 of CICE: the Los Alamos Sea Ice Model (Hunke & Lipscomb, 2008), the default choice is

$$S_i(\zeta) = 0.5 \times 3.2\left[1 - \cos\left(\pi\zeta^{0.407/(\zeta+0.573)}\right)\right], \tag{2.2}$$

where $\zeta = z/h$ is the position relative to the total depth of the ice. It is common, as an alternative, to choose a uniform salinity of 4 or 5 ppt (Holloway *et al.*, 2007). The validity of this choice is questionable, especially in significantly different future climatic conditions when the proportion of first-year ice may be much greater. In sea-ice models that use a 'zero-layer' approximation (Semtner, 1976) to equation (2.1), a fixed-salinity model is arguably the only sensible choice. How-

ever, the recent trend towards multilayer models of sea ice opens the possibility of determining the salinity field dynamically. It is important to emphasize that this needs to be done in a simple way; for instance the models in the Arctic Ocean Model Intercomparison Project (AOMIP) use at most 4 vertical grid points when integrating equation (2.1) (Holloway *et al.*, 2007).

Equation (2.1) and equations for heat conservation at the interfaces of the ice determine its growth rate $\dot{h}$. The salt flux F_S is usually then determined from the growth rate independently of the actual evolution the sea-ice salinity. Thus if the salinity field of the sea-ice is assumed to be constant in time, the salt flux

$$F_S = \dot{h}\Delta S, \tag{2.3}$$

where ΔS is the difference between the ocean salinity and the average sea-ice salinity. Indeed, in CICE, the average salinity for calculating the salt flux is specified independently of the prescribed salinity profile for calculating growth. In common with many AOMIP models, it takes an average salinity of 4 ppt, which is significantly lower than is typical for first-year ice.

These deficiencies have led much recent interest in dynamically determining the salinity of sea ice, both from those working at the small scale (Oertling & Watts, 2004; Wells *et al.*, 2011) and others working at polar-ocean scale (Vancoppenolle *et al.*, 2009*b*, 2010; Jeffery *et al.*, 2011; Saenz & Arrigo, 2012; Turner *et al.*, 2013; Griewank & Notz, 2013).

One central goal of this thesis is to develop a one-dimensional model for the thermodynamic growth of sea ice starting with the phase-averaged equations for heat and salt conservation. In the absence of gravity drainage, Feltham *et al.* (2006) have shown that these equations are essentially equivalent to equation (2.1). Therefore, we aim to develop a new model in which we determine the strength of gravity drainage within sea ice dynamically.

Chapter 3

Mushy-Layer Theory

3.1 Introduction to binary alloys

Two-component mixtures (called binary alloys) exhibit richer behaviour than one-component systems as the temperature, pressure or composition of the mixture is varied: they are subject to a number of different thermodynamic and fluid dynamical processes that we will explore in this chapter. Particularly relevant to sea-ice formation, there is the possibility of segregation when the alloy is solidified. Thus when saltwater is solidified, it is energetically unfavourable to incorporate salt into the solid crystals, so the solid crystals are essentially pure water and the remaining solution becomes increasingly concentrated in salt. The consequent increase in the density of the solution can drive an convective flow.

The behaviour of a binary alloy is best summarized by a phase portrait which shows the *equilibrium* phase or phases at given temperature T, pressure p and bulk composition S (called salinity when referring to sea ice). In the geophysical and experimental situations with which we are principally concerned, the dependence on pressure can be neglected so we can consider a two-dimensional section through the phase portrait at a fixed representative pressure.

Figure 3.1 shows one generic phase portrait of a type especially relevant to aqueous salt solutions. The liquidus curve separates the region of phase space where the mixture is purely liquid from the region where solid and liquid co-exist. Below the solidus, the binary alloy is completely solid but in the form of a solid

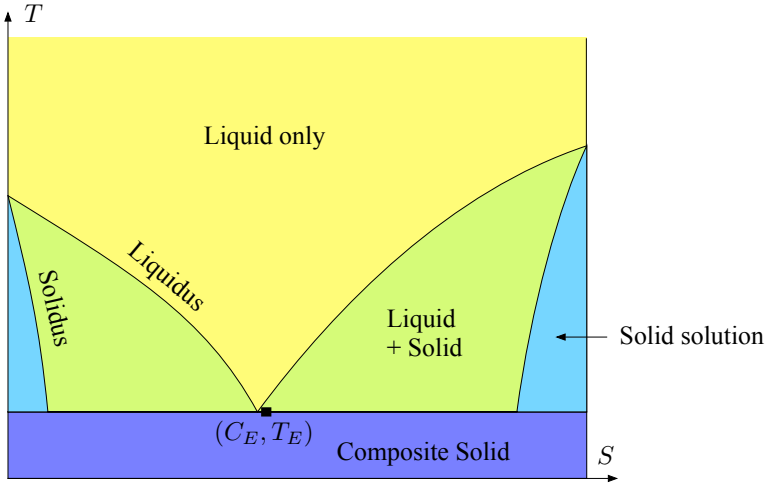

Figure 3.1: Phase portrait of a binary alloy at constant pressure, particularly relevant to aqueous salt solutions. Below the eutectic temperature T_E, the binary alloy is completely solidified and a composite containing crystals of both components is formed. Note that $C_E = C_L(T_E)$.

solution, in which molecules of one component are incorporated into the lattice of the other. Beneath the eutectic temperature T_E, a composite solid forms. This consists of crystals of both solid solutions.

The liquidus and solidus curves that separate these regions can be expressed as functions of temperature T by the relations $C = C_L(T)$ and $C = C_S(T)$ respectively. Between the solidus and liquidus, the solid fraction ϕ satisfies

$$\phi C_S(T) + (1 - \phi)C_L(T) = S. \tag{3.1}$$

Strictly, if the composition is measured in parts per thousand (ppt), ϕ is a solid mass fraction (which is only equal to the solid volume fraction if the densities of the phases are equal). Nevertheless, we will usually not make this distinction, as it is usually small in the situations we consider.

Returning to the concept of segregation, we can define a segregation coefficient k_D by the approximation

$$C_S(T) = k_D C_L(T). \tag{3.2}$$

Note that $k_D = 0$ for saltwater, since salt is completely segregated from ice

crystals, and any salt in sea ice is contained within interstitial brine.

3.2 Introduction to mushy layers

If a binary alloy is liquid at temperature and salinity below the liquidus, it is said to be 'constitutionally supercooled.' This situation happens generically at a planar solidification front because heat diffuses more rapidly than solute in most alloys. Supercooling is a metastable state and is typically relieved by morphological instability of the phase boundary.

Mullins & Sekerka (1964) considered a binary alloy that is steady in the frame of the solid–liquid interface and investigated sinusoidal perturbations to a planar interface. They derived a criterion for an instability that is driven by supercooling but stabilized by the surface energy of the interface. If the solidification rate is sufficiently rapid, as occurs in sea-ice formation, then the planar interface is unstable.

This instability causes a highly convoluted dendritic interface to form between the solid and liquid phases, as shown in figure 3.2. Solidification and dissolution occur across a large surface area until local thermodynamic equilibrium is achieved (supercooling is completely relieved). The concentration of the interstitial liquid and the temperature lie on the equilibrium liquidus curve in figure 3.1. The region containing both solid and liquid phases is called a mushy layer.

Our principal motivation in this thesis is sea-ice modelling but mushy layers arise in a number of industrial, geophysical and astrophysical situations. Industrially, when casting metal alloys, convection within the mushy layer is responsible for macrosegregation, which is a variation in the composition of a casting (Beckermann *et al.*, 2000). Here, the solidification must be controlled in order to suppress this undesirable effect. Geologically, mushy-layer theory (generalized to account for a melt with many more than two components) may be helpful in understanding observed features when igneous intrusions solidify (Huppert, 2000). Furthermore, there are indications that the solid core of some planets may retain a small quantity of trapped melt – thermodynamic estimates indicate that this should be the case, although there is considerable uncertainty. Indeed, there may also be a thin region at the boundary between the inner and outer core of

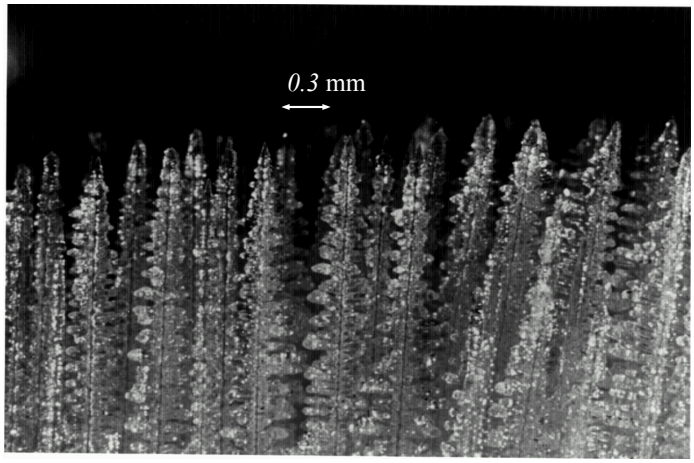

Figure 3.2: Adapted from Worster (1997). The dendritic structure of the solid phase when aqueous ammonium chloride is solidified.

the Earth where convection within the mush is important in understanding the transport of light elements from the inner core that can contribute to driving the geodynamo that generates the Earth's magnetic field (Fearn *et al.*, 1981). Therefore, the study of convection within mushy layers has a broad range of applications and has been considered by researchers across these fields. These can provide important insights into sea-ice modelling.

3.3 Mushy-layer equations

The interface between the solid and liquid phases in a mushy layer is highly convoluted. Therefore, instead of tracking the solid crystals separately, the approach taken by mushy-layer theory, as reviewed in Worster (1992*a*, 2000), is to average over a control volume that contains both solid and liquid phases. These averaged quantities are summarized in table 3.1. In general the material properties of the two phases differ. These are summarized in table 3.2.

This continuum approach allows us to write down continuum field equations for conservation of mass, heat and solute. Mass conservation is described by

$$(\rho_s - \rho_l)\frac{\partial \phi}{\partial t} + \rho_l \nabla \cdot \boldsymbol{u} = 0. \tag{3.3}$$

Table 3.1: Variables in mushy-layer theory

Variable	Definition
$T(\boldsymbol{x}, t)$	local mean temperature
$C(\boldsymbol{x}, t)$	local mean concentration of the interstitial fluid
$S(\boldsymbol{x}, t)$	local bulk concentration averaged over both phases
$\phi(\boldsymbol{x}, t)$	average (volume) fraction occupied by the solid phase
$\boldsymbol{u}(\boldsymbol{x}, t)$	Darcy velocity

Table 3.2: Material properties in mushy-layer theory

Properties	Definition
ρ_l, ρ_s	density of the liquid and solid phases, respectively
k_l, k_s	thermal conductivities
D_l, D_s	diffusivities of salt
$(c_p)_l$, $(c_p)_s$	specific heat capacities per unit mass
c_l, c_s	(*alternatively*) heat capacities per unit volume
$\mathcal{L}$	latent heat per unit mass of solid formed
C_S	concentration of the solid phase
Π	permeability of the mushy layer

The difference in densities between the phase drives a divergent flow $\boldsymbol{u}$ (the Darcy velocity) as the mushy layer solidifies, even though the interstitial fluid flow is divergence-free.

Heat conservation is described by

$$\overline{\rho c_p}\frac{\partial T}{\partial t} + (\rho c_p)_l \boldsymbol{u}\cdot\nabla T = \nabla\cdot(\overline{k}\nabla T) + \rho_s\mathcal{L}\frac{\partial \phi}{\partial t}, \tag{3.4}$$

which is a phase-averaged advection–diffusion equation with an additional term due to latent heat release as the solid fraction changes. In this expression $\overline{\rho c_p} = \phi(\rho c_p)_s + (1-\phi)(\rho c_p)_l$ is the heat capacity of a mushy layer. Since dendrites in mushy layers usually align with temperature gradients, it is usual in mushy-layer theory to take $\overline{k} = \phi k_s + (1-\phi)k_l$ – a form which is appropriate to laminates and is an upper bound for the thermal conductivity of an arbitrary crystal structure (Batchelor, 1974) – and neglect the fact that $\overline{k}$ could be an anisotropic tensor.

Salt conservation is described by

$$(1-\phi)\frac{\partial C}{\partial t} + \boldsymbol{u}\cdot\nabla C = \nabla\cdot(\overline{D}\nabla C) + (C-C_S)\frac{\partial \phi}{\partial t}, \tag{3.5}$$

where the diffusivity of solute $\overline{D} = \phi D_s + (1-\phi)D_l \approx (1-\phi)D_l$, since $D_s \ll D_l$ typically. This system is closed with equation (3.1) for ϕ. The liquidus condition,

$$T = T_L(C), \tag{3.6}$$

discussed above and shown in figure 3.1, couples equations (3.4, 3.5) such that they constitute two equations for the two independent variables T and ϕ. Equivalently, the independent variables are T and S and equation (3.5) becomes:

$$\frac{\partial S}{\partial t} + \boldsymbol{u}\cdot\nabla C = \nabla\cdot(\overline{D}\nabla C), \tag{3.7}$$

with $C = C_L(T)$.

The mushy layer is a porous medium so we use Darcy's law to describe the flow. As we discuss later, this applies in the interior of a mushy layer but might not hold near an interface where the solid fraction is zero (Le Bars & Worster, 2006). In general, the permeability Π is an anisotropic tensor but if for simplicity we assume it is isotropic then Darcy's law gives

$$\mu\boldsymbol{u} = \Pi(-\nabla p + \rho_l \boldsymbol{g}). \tag{3.8}$$

3.3.1 Ideal mushy-layer equations

Although physical binary alloys form mushy layers that require these full equations for an accurate description, we can better understand the mathematical structure of these equations by considering the case of an ideal binary alloy. In this idealization, we assume that the phases have the same material and thermal properties and that the liquidus is linear

$$T_L(C) = -mC, \tag{3.9}$$

of gradient $(-m)$. This sign is appropriate to the left side of figure 3.1 but the theory applies equally to the other side where the liquidus temperature increases with concentration. We also assume that segregation is complete $k_D = 0$, so $C_S = 0$. Furthermore, we take the solute diffusivity D_l to be much less than the thermal diffusivity $\kappa = k/\rho c_p$, which means that we can neglect solute diffusion in the equation for salt conservation (3.5). Since C is coupled to T by the liquidus condition, we are not neglecting the highest derivative in equation (3.5) in a singular fashion.

If we use a linear equation of state for density $\rho = \rho_0 \left[1 + \beta(C - C_0)\right]$, where C_0 is some appropriate reference concentration and $T_0 = T_L(C_0)$, and an extended Boussinesq approximation in which we neglect density variation except in the buoyancy term in Darcy's law (3.8) and assume constant permeability $\Pi = \Pi_0$, then the ideal mushy-layer equations are (Worster, 1997, 2000)

$$\nabla \cdot \boldsymbol{u} = 0, \tag{3.10}$$

$$\frac{\partial T}{\partial t} + \boldsymbol{u} \cdot \nabla T = \kappa \nabla^2 T - \frac{\mathcal{L}}{c_p} \frac{\partial \phi}{\partial t}, \tag{3.11}$$

$$(1 - \phi)\frac{\partial C}{\partial t} + \boldsymbol{u} \cdot \nabla C = -(C - C_S)\frac{\partial \phi}{\partial t}, \tag{3.12}$$

$$T - T_0 = -m(C - C_0), \tag{3.13}$$

$$\mu \boldsymbol{u} = \Pi_0 \left[-\nabla p - \rho_0 g \beta (C - C_0)\boldsymbol{e}_z\right]. \tag{3.14}$$

These equations have been studied analytically and numerically in various cases and have been used to interpret several experimental results. Most pertinently, linear stability analysis (Worster, 1992*b*) indicates that the dominant dimensionless parameter governing the onset of convection in a mushy layer is a type of Rayleigh number R_m, which we define below. This parameter relates the available gravitational potential energy (dominated by the interstitial salinity gradient) to the dissipation caused by thermal diffusion and fluid viscosity. A Rayleigh number can be used to interpret the onset of convection in the experiments of Wettlaufer *et al.* (1997*a*) and the confinement of convection to a lower layer of sea ice (Notz & Worster, 2008).

However, the fully-developed convecting state with liquid chimneys is not

amenable to complete analytical treatment. Therefore, several studies (Schulze & Worster, 1998; Chung & Worster, 2002; Wells *et al.*, 2010, 2013) solve the steady ideal mushy-layer equations numerically with a prescribed periodic, planar array of chimneys. These solutions typically use analytic approximations to account for the liquid melt region and the difficult free-surface problem of the chimney–mush interface. The computational complexity of numerical models, even in planar geometry and with other considerable simplifications, means that they are not directly applicable to predictive sea-ice modelling. In sea ice, the brine channel spacing is of the order of centimetres and so is utterly unresolvable in climate models. Therefore, in chapter 4, we will develop semi-analytical convective solutions of these equations in a simple modelling framework.

3.3.2 Directional solidification – steady ideal mushy-layer equations

Directional solidification is a configuration that admits steady solutions of the ideal mushy-layer equations. This set-up can also be studied experimentally (Peppin *et al.*, 2007) and their apparatus is shown in figure 3.3.

In the directional solidification arrangement, a solidification cell is pulled downwards through fixed heat exchangers at a constant speed V in the negative z-direction. There is a steady state in the laboratory frame where the solid phase has velocity $-V\boldsymbol{e}_z$. We non-dimensionalize lengths with respect to the thermal length scale κ/V, times with κ/V^2, velocities with V and introduce a single dimensionless variable θ for temperature and salinity (because of the linear liquidus condition that couples these). Then the steady ideal mushy-layer equations are

$$\nabla \cdot \boldsymbol{u} = 0, \tag{3.15}$$

$$\boldsymbol{u} \cdot \nabla\theta - \frac{\partial\theta}{\partial z} = \nabla^2\theta - \mathcal{S}\frac{\partial\phi}{\partial z}, \tag{3.16}$$

$$\boldsymbol{u} \cdot \nabla\theta - (1-\phi)\frac{\partial\theta}{\partial z} = -(\theta - \mathcal{C})\frac{\partial\phi}{\partial z}, \tag{3.17}$$

$$\boldsymbol{u} = -R_m(\nabla p + \theta\boldsymbol{e}_z). \tag{3.18}$$

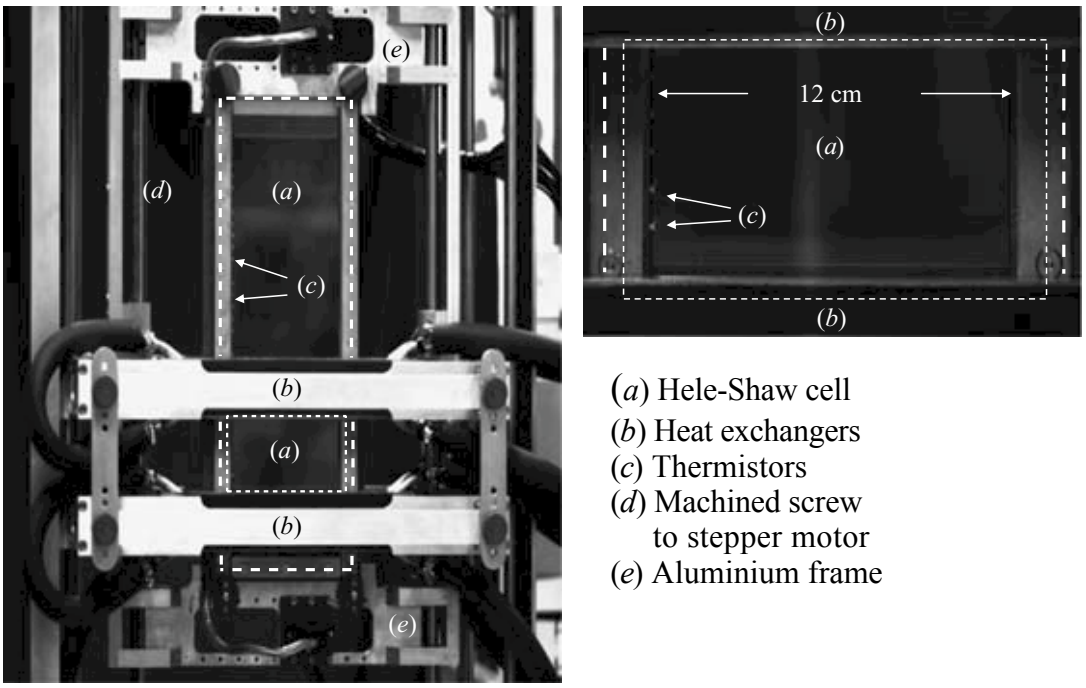

Figure 3.3: The directional solidification apparatus developed by Peppin *et al.* (2007). The motors can be adjusted to pull the Hele-Shaw cell (a) downwards (say) at various speeds between the fixed heat exchangers (b).

The dimensionless temperature and concentration

$$\theta = \frac{T - T_L(C_0)}{\Delta T} = \frac{C - C_0}{\Delta C}. \tag{3.19}$$

The Stefan number $\mathcal{S} = \mathcal{L}/(c_p \Delta T)$ is the ratio of latent heat $\mathcal{L}$ release to driving temperature gradient $\Delta T = T_L(C_0) - T_E$ and specific heat c_p. The compositional ratio is $\mathcal{C} = (C_S - C_E)/\Delta C$, where $\Delta C = C_0 - C_E$.

In a planar geometry, we can write $\boldsymbol{u} = (-\psi_z, \psi_x)$, since $\nabla \cdot \boldsymbol{u} = 0$. Note that, throughout this thesis, subscript x, z denote partial derivatives. Eliminating the pressure in Darcy's law (3.18), we find

$$\nabla^2 \psi = -R_m \theta_x, \tag{3.20}$$

where

$$R_m = \frac{\beta \Delta C g \Pi_0}{\nu V} \tag{3.21}$$

is the mush Rayleigh number, with gravitational acceleration g and the kinematic viscosity of the liquid phase ν. This important dimensionless parameter relates the driving compositional density difference for convective to the dissipation caused by convection within the mush, and so governs the onset of convection within a mushy layer (Worster, 1992*b*). Note that the thickness of a mushy layer in this configuration is controlled by thermal diffusion, so if we introduce $H = \kappa/V$ as this length scale, we can write

$$R_m = \frac{\beta \Delta C g \Pi_0 H}{\nu \kappa}, \tag{3.22}$$

which is more recognisably a Rayleigh number for convection in a porous medium.

We consider the further idealization $\mathcal{C} \gg 1$. In this limit, the salt conservation equation (3.17) determines the solid fraction ϕ through

$$\boldsymbol{u} \cdot \nabla \theta - \theta_z = \mathcal{C} \phi_z \tag{3.23}$$

and so determines the latent heat release term in the heat conservation equation (3.16). Therefore we can decouple equations (3.16) and (3.17) to obtain a

combined thermal equation (Worster, 2000; Huppert & Worster, 2012)

$$\Omega\,(\boldsymbol{u}\cdot\nabla\theta-\theta_z)=\nabla^2\theta, \tag{3.24}$$

where $\Omega = 1 + \mathcal{S}/\mathcal{C}$ is the factor by which the heat capacity of a mushy layer is enhanced by latent heat release. We later generalize this concept to non-ideal mushy layers.

3.4 Boundary conditions

The boundary conditions at the mush–liquid interface are one of the subtlest aspects of solving the mushy-layer equations. This is associated with the difficulty of specifying the location of the interface consistently with the continuum approximation made. Thus an interfacial region of thickness comparable to the pore scale lies outside the scope of the formal continuum approximation inherent in the mushy-layer equations.

Furthermore, the appropriate boundary conditions depend on the relative velocities of the solid and liquid phases and that of the mush–liquid interface; although some individual cases had been considered previously, the first systematic derivation of all four possible cases was given by Schulze & Worster (2005).

Nevertheless, some boundary conditions apply to every possible type of situation. Firstly, temperature is continuous across the interface

$$[T]_l^m = 0. \tag{3.25}$$

Secondly, heat is conserved at the interface and we can integrate the equation of heat conservation (3.4), which also applies in the liquid region with $\phi = 0$, across the interface to show that

$$\rho_s\mathcal{L}\phi_m V = [\overline{k}\boldsymbol{n}\cdot\nabla T]_l^m, \tag{3.26}$$

where V is the velocity of the interface relative to the solid phase in the direction normal to the interface (from mush to liquid). Note that this V is equivalent to the pulling speed introduced in section 3.3.2. Thus, if the solid fraction at

the interface ϕ_m is non-zero, there is a discontinuous change in the conductive heat flux because of latent heat release at the interface. Thirdly, salt is conserved at the interface, and we can integrate the equation of solute conservation (3.5) across the interface to show that

$$-[C]_l^m U_n = \phi_m (C_m - C_S) V, \tag{3.27}$$

where U_n is the velocity of the liquid relative to the mush–liquid interface, and subscripts m and l denote quantities evaluated on the mush and liquid sides of the interface respectively. So if $[C]_l^m = 0$ (the interstitial concentration is continuous), then $\phi_m = 0$ at the interface and vice versa. Note that we have neglected diffusion of salt, which may not be appropriate at an interface.

As we have emphasized, the interstitial concentration within the mushy layer is coupled to the temperature field and thus the equation of solute conservation (3.5) determines the solid fraction ϕ. The equation for ϕ is hyperbolic and characteristics follow the solid phase. Therefore, if the mushy layer is freezing ($V > 0$), we must specify the solid fraction at the mush–liquid interface, whereas if it is dissolving ($V < 0$), we must specify the solid fraction at some other boundary away from the interface. In the latter case, it is inconsistent to impose, *a priori*, $\phi = 0$ at the mush–liquid interface, since ϕ must be determined at the interface as part of the solution.

Similarly, in the liquid melt, in the absence of solute diffusion, characteristics are streamlines. Therefore, in the case of 'outflow' ($U_n > 0$, flow from mush to liquid), $[C]_l^m = 0$, since any discontinuity in the concentration field would be advected away from the interface. Thus the temperature at the interface determines the interstitial concentration C_m, which, given the flow field, determines the concentration everywhere in the liquid. However, in the care of 'inflow' ($U_n > 0$, flow from liquid to mush), we must impose a boundary condition on concentration away from the mush. This determines the concentration C_l, and in general the concentration field is discontinuous across the interface. Therefore, outflow requires $\phi_m = 0$, but not inflow.

As shown in Schulze & Worster (2005), these conditions of heat and salt conservation are insufficient to determine the location of the interface for a freezing

mushy layer, $V > 0$. (In the other case, $V < 0$, there is an additional imposed condition at the mush–solid boundary.) Therefore, motivated by the fact that a mushy layer grows to alleviate constitutional supercooling, we apply a condition of marginal equilibrium as follows.

For inflow, $U_n < 0$, the marginal equilibrium condition extends the liquidus condition into the liquid such that the temperature satisfies

$$T_l = T_L(C_l). \tag{3.28}$$

Since the temperature is continuous (equation 3.25), $C_l = C_m$, and hence $\phi_m = 0$.

However, for outflow, $U_n > 0$, the marginal equilibrium condition requires that

$$DT/Dt = 0 \tag{3.29}$$

at the mush–liquid interface, where D/Dt is a Lagrangian derivative. This condition is justified as follows. Outflow requires $\phi_m = 0$. The concentration is constant along a streamline, and a fluid parcel is moving into the melt, so $\mathrm{D}T/\mathrm{D}t \geq 0$ on the liquid side of the interface. But $\phi_m = 0$ so by equation (3.26) $[\boldsymbol{n} \cdot \nabla T] = 0$ as well as $[T] = 0$. (Here we have used the fact that $\overline{k} = k_l$ at the interface, since $\phi_m = 0$.) Therefore $\mathrm{D}T/\mathrm{D}t \geq 0$ on the mush side also. C is coupled to T through the liquidus condition, so $\mathrm{D}C/\mathrm{D}t \geq 0$ on the mush side. (Note that this sign is reversed if the liquidus has negative slope.) However, equation (3.5) for salt conservation within the mush with $\overline{D} = 0$ can be rearranged to

$$\frac{\mathrm{D}C}{\mathrm{D}t} = \phi\frac{\partial C}{\partial t} + (C - C_S)\frac{\partial \phi}{\partial t}. \tag{3.30}$$

Now $\phi \geq 0$ and $\frac{\partial \phi}{\partial t} \geq 0$ since it is zero on the interface and we are solidifying. Furthermore, $\frac{\partial C}{\partial t} \leq 0$ and $C - C_S \leq 0$ (these signs are reversed if the liquidus has negative slope), so $\mathrm{D}C/\mathrm{D}t \leq 0$ on the mush side. Therefore $\mathrm{D}C/\mathrm{D}t = \mathrm{D}T/\mathrm{D}t = 0$ at the interface.

3.5 Solidification with a corner flow

The appropriate boundary conditions at a mush–liquid interface depend on both thermodynamics and fluid dynamics. However, the latter are complicated at the boundary between a porous medium and a liquid because the averaging used to derive Darcy's law for fluid flow does not apply over a transition region of thickness comparable to the pore scale. It is important to note that we cannot interrogate this region too precisely within the continuum approximation. Nevertheless, is important to have a continuous velocity across the mush–liquid interface for thermodynamic reasons, particularly in applying the marginal equilibrium condition. However, in treating the mushy layer and bulk liquid region as two separate domains, a potential problem arises in that there may be a discontinuity in the tangential velocity (a slip) at the interface.

Therefore, in this section, we take the approach of Le Bars & Worster (2006) of extending Stokes equation (for viscous flow) into a transition region inside the mushy layer of dimensionless thickness

$$\delta = c\mathcal{D}^{1/2}, \tag{3.31}$$

where the Darcy number $\mathcal{D}$ is the permeability of the mushy layer that has been non-dimensionalized with respect to the square of an appropriate macroscopic lengthscale that is also used in non-dimensionalizing δ. For $c = O(1)$, this was shown to give comparable results to the Darcy-Brinkman equation that smooths the transition between liquid and mush by having one equation governing the flow in both regions. The transition region effectively allows a slip to occur across it, while retaining a continuous velocity. However, it is not intended to to constitute a complete description of the fluid mechanics at a mush–liquid interface, and is introduced solely for thermodynamic reasons.

An additional problem arises in that the marginal equilibrium boundary condition is fundamentally two-dimensional. Thus we consider a particular 'toy' problem that has a two-dimensional flow, and yet can be studied in a one-dimensional fashion. This problem was originally formulated by D. Conroy and M. G. Worster (*cf.* the report Conroy & Worster, 2006). Here, we develop that study by also

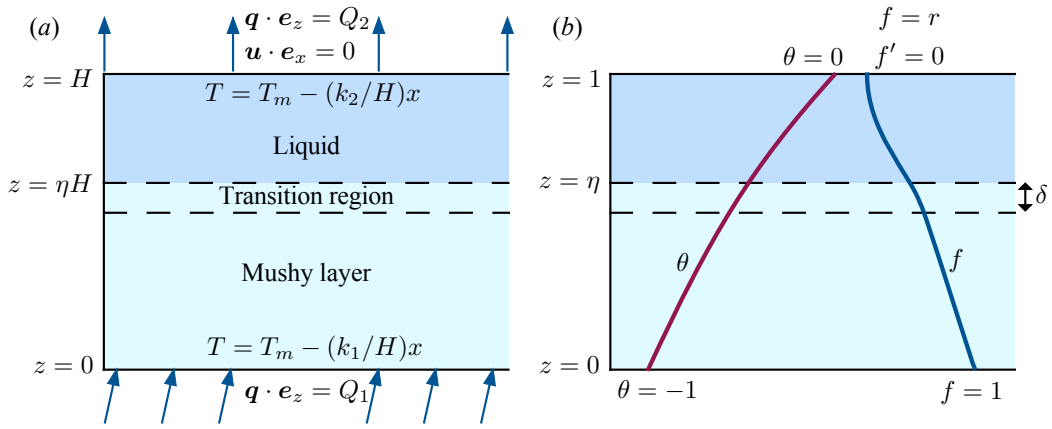

Figure 3.4: Problem formulation in (a) dimensional variables and (b) dimensionless variables.

considering the case of dissolving mushy layers (rather than only freezing ones) and greatly simplifying the study of the marginal equilibrium condition by taking the asymptotic limit $\mathcal{D} \to 0$ to explain why solutions only exist in particular reasons of parameter space. This toy problem allows us to explore and clarify the marginal equilibrium condition in a much simpler system than the convective mushy layer equations that we consider in the following chapter.

3.5.1 Problem formulation

In order to investigate all four types of boundary condition, we consider a forced flow problem and neglect natural convection. We consider a semi-infinite rectangular channel of width H in a directional solidification configuration (with the pulling velocity V perpendicular to the semi-infinite boundaries). We impose boundary temperatures $T = T_m - (k_{1,2}/H)x$, $0 < x < \infty$, on two permeable walls, where x is the distance down the channel. We impose $k_1 > k_2$ such that the lower wall, which is adjacent to a mushy layer, is colder than the upper wall, which is adjacent to a liquid melt that occupies a fraction $1 - \eta$ of the channel, as shown in figure 3.4a. To control the flow, we impose the material flux $Q_{1,2}$ at the permeable walls, where the material flux $\boldsymbol{q} = \boldsymbol{u} - V\boldsymbol{e}_z$. We also impose no horizontal velocity at the upper wall in the figure.

Figure 3.4*b* shows the dimensionless version of this problem. In this section, we non-dimensionalize lengths with respect to the dimensional channel width H, and material fluxes with respect to Q_1. This choice introduces the Péclet number

$$Pe = Q_1 H/\kappa \tag{3.32}$$

into the dimensionless ideal mushy-layer equations (3.15–3.18). Henceforth, x and z denote dimensionless lengths. The appropriate macroscopic lengthscale is H so the Darcy number in this problem is

$$\mathcal{D} = \Pi_0/H^2. \tag{3.33}$$

The ratio of imposed fluxes

$$r = Q_2/Q_1 \tag{3.34}$$

determines the direction of the flow. So $r < 1$ corresponds to a flow in the positive x-direction. We restrict attention to the case $r > 0$ so that the direction of the imposed flow does not change.

Motivated by the separable solution for Stokes flow in a corner (Batchelor, 1967), we seek a solution for the dimensionless material flux in the form

$$\boldsymbol{q} = [-xf'(z), f(z)]\,. \tag{3.35}$$

In the liquid and transition region the flow satisfies the Stokes equation $\nabla^2\boldsymbol{u} = \nabla p$. Note that the streamfunction associated with the Darcy velocity $\boldsymbol{u}$ is $\psi = xf(z) + x$. Eliminating the pressure, we find that Stokes equation becomes $f^{(4)}(z) = 0$. In the mushy layer, the flow satisfies Darcy's law (3.8), which in the absence of convection becomes $(f'/\Pi)' = 0$. In the simplest case of uniform permeability $\Pi = \Pi_0$, the solution is

$$f = C_0 z + 1 \qquad 0 \le z \le \eta - \delta, \tag{3.36}$$

$$f = B_0(1-z)^3 + A_0(1-z)^2 + r \qquad \eta - \delta \le z \le 1, \tag{3.37}$$

where A_0, B_0, and C_0 are constants that can be readily determined by applying mass conservation, no-slip and continuity of pressure at the mush–liquid interface,

respectively

$$[f] = 0, \qquad [f'] = 0, \qquad f''' = -f'/\mathcal{D}, \qquad (z = \eta - \delta). \tag{3.38}$$

We find that

$$A_0 = -3B_0 \left[\frac{1 - \eta + \delta}{2} + \frac{\mathcal{D}}{1 - \eta + \delta} \right], \tag{3.39}$$

$$B_0 = \frac{2(r-1)}{(1 - \eta + \delta)^3 + 6\mathcal{D}(1 + \eta - \delta)}, \tag{3.40}$$

$$C_0 = 6\mathcal{D}B_0. \tag{3.41}$$

Note that, in the case of uniform permeability, f is independent of θ and ϕ, so is independent of the thermodynamics of the problem. Note that $\delta = 0$ ($c = 0$ in $\delta = c\mathcal{D}^{1/2}$) is equivalent to the no-slip condition at the mush–liquid interface. Our choice $c = O(1)$ means that the streamfunction f is continuously differentiable (while its second derivative is not continuous). This means that there are well-defined streamlines at the mush–liquid interface, essential to imposing the marginal equilibrium condition.

The significant feature of this two-dimensional problem that allows us to treat it in a one-dimensional fashion is that the imposed vertical temperature gradient ΔT scales linearly with x. In particular

$$\Delta T = (k_1 - k_2)x. \tag{3.42}$$

We choose units such that $T_m = 0$ and write

$$T = -k_2 x + \Delta T\theta(z) = (k_1 - k_2)x(\theta - \mathcal{T}), \tag{3.43}$$

where $\mathcal{T} = k_2/(k_1 - k_2) > 0$ gives a measure of the ratio of horizontal to vertical temperature gradients at the top boundary.

The steady ideal mushy-layer equations (3.16, 3.17) give

$$f\theta' - f'(\theta - \mathcal{T}) = \frac{\theta''}{Pe} - \mathcal{S}\mathcal{V}\phi', \tag{3.44}$$

$$f\theta' - f'(\theta - \mathcal{T}) = -\mathcal{V}\left[\phi(\theta - \mathcal{T})\right]', \tag{3.45}$$

where $\mathcal{V} = V/Q_1$ represents the ratio of the solidification rate to the imposed flow. The Stefan number $\mathcal{S} = \mathcal{L}/(c_p(k_1 - k_2)x)$, so we can neglect latent heat release at sufficiently large x. We therefore take $\mathcal{S} \ll 1$ and neglect this term completely.

Equation (3.44) is also the thermal equation for the liquid region, where $\phi = 0$. Salt conservation in the liquid region is governed by $\boldsymbol{q} \cdot \nabla C = 0$ in the absence of diffusion, so

$$C \propto xf(z). \tag{3.46}$$

Equation (3.45) has a first integral

$$\phi = \frac{1}{Pe_V}\frac{\theta' + \phi_c}{\mathcal{T} - \theta}, \tag{3.47}$$

where $Pe_V = VH/\kappa = \mathcal{V}Pe$ is a Péclet number based on the solidification rate and ϕ_c is a constant determined by the relevant boundary conditions discussed below. Thus the solid fraction is inversely proportional to the solidification rate V.

3.5.2 Boundary conditions

The dimensionless boundary conditions on temperature are

$$\theta(0) = -1, \qquad \theta(1) = 0, \qquad [\theta]_l^m = 0, \qquad [\theta']_l^m = 0, \tag{3.48}$$

since $\mathcal{S} \ll 1$, so latent heat release at the interface is insignificant.

Dissolving outflow. If $V < 0$, $U_n > 0$, dissolution means that characteristics of ϕ propagate towards the mush–liquid interface, so ϕ must be specified at $z = 0$

$$\phi(0) = \phi_0, \tag{3.49}$$

where ϕ_0 is some imposed value, which allows us to eliminate ϕ_c. Imposing the solid fraction at $z = 0$ is equivalent to imposing a bulk concentration $S_0 = (1 - \phi_0)\, k_1 x/m$ there. We define α_1 by $S_0 = \alpha_1 x/m$. Conservation of solute at the mush–liquid interface requires that

$$[C]_m^l = 0 \Rightarrow \phi_m = 0, \tag{3.50}$$

whereby we can determine η.

Dissolving inflow. If $V < 0$, $U_n < 0$, equation (3.49) continues to apply. However, when the flow is from liquid to mush, we must impose the concentration at $z = 1$, and then use conservation of solute (3.27) to determine ϕ_m.

$$\phi_m = \frac{[C]_m^l}{C_m} \frac{f(\eta)}{\mathcal{V}}, \tag{3.51}$$

where $C_l = C(\eta^+)$ is determined by $\boldsymbol{q}\cdot\nabla C = 0$ in the liquid region and a boundary condition specifying C at $z = 1$. In particular, if we impose $C = (\alpha_2/m)x$ at the upper plate, then

$$C_l = x \frac{\alpha_2}{m} \frac{f(\eta)}{f(1)}, \tag{3.52}$$

and so

$$\phi_m = \left(-\mathcal{T}_C \frac{f(\eta)}{f(1)} \frac{1}{\theta(\eta) - \mathcal{T}} - 1 \right) \frac{f(\eta)}{\mathcal{V}}, \tag{3.53}$$

where $\mathcal{T}_C = \alpha_2/(k_1 - k_2)$. As noted previously, in general $\phi_m \neq 0$.

Freezing outflow. If $V > 0$, $U_n > 0$, equation (3.50) applies, which can also be used to eliminate ϕ_c in equation (3.47). However, it is no longer appropriate to apply a condition on ϕ at $z = 0$. Instead, we employ the marginal equilibrium criterion

$$\boldsymbol{q} \cdot \nabla\theta = 0 \qquad (z = \eta). \tag{3.54}$$

Freezing Inflow. If $V > 0$, $U_n > 0$, we impose the concentration at $z = 1$ thereby fixing the solute field C_l at $z = \eta^+$ (equation 3.52). In this case, marginal equilibrium $T(\eta) = T_L(C_l)$ gives an interfacial temperature

$$\theta_i = \mathcal{T} - \mathcal{T}_C \frac{f(\eta)}{f(1)}. \tag{3.55}$$

Additionally, C is continuous since $T = T_L(C)$ on both sides of the interface and T is continuous. Hence equation (3.50) applies and determines ϕ_c.

3.5.3 Results for one-dimensional flow

By varying Q_1 and Q_2, our configuration (figure 3.4) realizes all the possible types of flow at the mush–liquid interface in a two-dimensional fashion. However, it is simpler to first consider the one-dimensional problem, which is relevant to several of the possible cases, to illustrate a number of important physical principles.

If $r = 1$, ($Q_1 = Q_2 \equiv Q$, say) then $f = 1$ (the flow is vertical) and the governing equations (3.44, 3.45) become

$$\theta' = \frac{\theta''}{Pe} \qquad 0 \le z \le 1, \tag{3.56}$$

$$\theta' = -\mathcal{V}\left[\phi(\theta - \mathcal{T})\right]' \qquad 0 \le z \le \eta. \tag{3.57}$$

Integrating (3.56), we find the temperature

$$\theta(z) = \frac{e^{zPe} - e^{Pe}}{e^{Pe} - 1}, \tag{3.58}$$

so the shape of the temperature profile depends on the sign of $Pe = QH/\kappa$, which is positive for outflow and negative for inflow. Equation (3.58) gives the location of the interface

$$\eta = \frac{\log\left[\theta_i(e^{Pe} - 1) + e^{Pe}\right]}{Pe}, \tag{3.59}$$

in terms of the interfacial temperature $\theta_i = \theta(\eta)$, and has a unique solution for all $-1 \le \theta_i \le 0$.

Integrating (3.57), we find that the solid fraction satisfies

$$\mathcal{V}\phi(\theta - \mathcal{T}) = -\theta + \phi_c, \tag{3.60}$$

where the constant ϕ_c is determined by the relevant boundary conditions. We consider the four different cases identified previously.

Dissolving outflow. We use the boundary conditions (3.49, 3.50) to elimi-

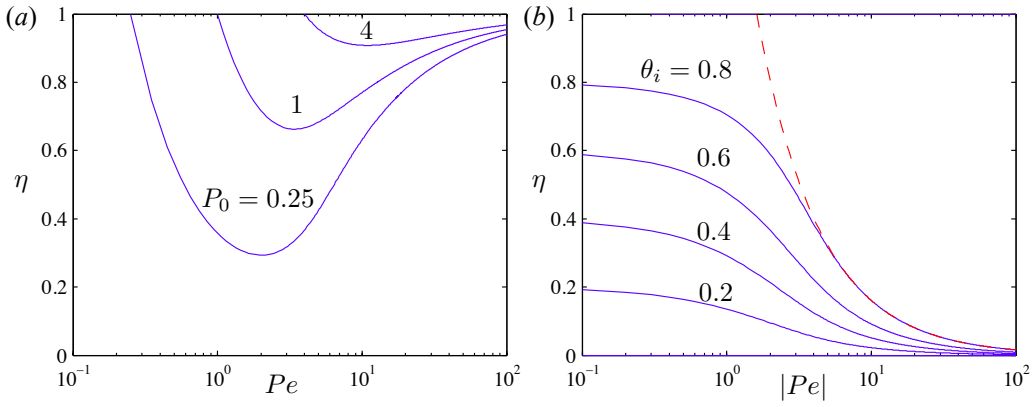

Figure 3.5: Exact solutions for the interface location η in the case of: (a) dissolving outflow and (b) freezing inflow. In (a) we show variation with imposed flow $Pe = QH/\kappa$ at various values of $P_0 = Pe_V\phi_0(1+\mathcal{T})$, which increases as solidification becomes more significant. In (b) we show variation at various values of θ_i, which is controlled thermodynamically according to equation (3.64). The asymptotic behaviour (equation 3.66) at large $|Pe|$ is indicated by the dashed red curve.

nate ϕ_c and find

$$\theta_i = -1 + (-\mathcal{V})\phi_0(1+\mathcal{T}), \tag{3.61}$$

which determines η from equation (3.59). There are a number of important features of this solution, as shown in figure 3.5(a). In this case, $\mathcal{V} < 0$, so $\theta_i \geq -1$ as required. However, the condition that $\theta_i \leq 0$ means that there is a critical imposed flux below which there are no solutions:

$$\frac{Q}{-V} \geq (1+\mathcal{T})\phi_0 = \frac{T_L(S) - T|_{z=0}}{\Delta T}. \tag{3.62}$$

As we approach the critical flux from above, the mush fills the layer. Above the critical flux the mush thickness initially decreases (primarily due to a rapid drop in interface temperature), then eventually increases slowly towards 1. Indeed we have shown that $\eta \to 1$ as $Pe \to \infty$ by simple asymptotic analysis of (3.59).

Dissolving inflow. This case is degenerate in that the prescribed solid fraction at the lower wall and prescribed concentration at the upper wall gives two independent measures of the solid fraction at the mush–liquid interface, which

are consistent if and only if

$$1+\mathcal{T}-\mathcal{T}_C = \mathcal{V}\phi_0(1+\mathcal{T}) \Leftrightarrow [T|_{z=0} - T_L(S)|_{z=1}] = \mathcal{V}\,[T_L(S)|_{z=0} - T|_{z=0}] \quad (3.63)$$

independently of η. This degeneracy arises because the condition of salt conservation at the interface is redundant and so no longer determines η.

Freezing outflow. In this one dimensional problem, streamlines of $\boldsymbol{q}$ are vertical, but isotherms are always curved towards the positive x-direction, so they can never be tangent, so the marginal equilibrium condition (3.54) is never satisfied. This motivates detailed consideration of the two-dimensional problem in section 3.5.4.

Freezing inflow. The boundary condition (3.55) implies that the interface temperature

$$\theta_i = \mathcal{T} - \mathcal{C}_r. \quad (3.64)$$

To ensure that this lies in the correct range, we require

$$k_1 \geq \alpha_2 \geq k_2 \Leftrightarrow T|_{z=0} \leq T_L(S)|_{z=1} \leq T|_{z=1}\,. \quad (3.65)$$

If these conditions are is satisfied, then the temperature of the interface is set entirely thermodynamically. We then determine the position of the interface from equation (3.59), as shown in figure 3.5. We analyse (3.59) asymptotically to show

$$\eta \sim 1+\theta_i \quad \text{as} \quad |Pe| \to 0, \qquad \eta \sim \log(-1/\theta_i)/|Pe| \quad \text{as} \quad |Pe| \to \infty. \quad (3.66)$$

The interface position η decreases slowly with the strength of the flow $|Pe|$ between these two limits.

However, the solid fraction depends on the fluid flow. Applying (3.50), we eliminate ϕ_c and find that ϕ increases monotonically away from the mush–liquid interface. So $\phi \leq 1$ is satisfied provided $\phi(0) \leq 1$, so

$$(-\mathcal{V}) \geq \frac{\mathcal{T}-\mathcal{T}_C+1}{1+\mathcal{T}} = 1 - \frac{\alpha_2}{k_1}. \quad (3.67)$$

Thus there is a minimum solidification rate required for physically meaningful solutions.

3.5.4 Results in the case of freezing outflow

The case of a freezing outflow is especially significant for our study because it occurs in the case of flow into a chimney caused by convection within a mushy layer analysed in chapter 4. Being able to investigate the marginal equilibrium condition relevant to freezing outflow, which requires that streamlines are tangent to isotherms at the mush–liquid interface, is also one of the main reasons to introduce a two-dimensional problem. Therefore, in terms of two-dimensional flow, we focus exclusively on freezing outflow.

Our analysis highlights two crucial issues. Firstly, the existence of a solution to the full problem (including the marginal equilibrium condition (3.54), which with equation (3.44) implies that $\theta''(\eta) = 0$) requires $\theta''(0) < 0$. The marginal case $\theta''(0) = 0$ is the exact linear solution to (3.44), which occurs if and only if

$$r = \frac{\mathcal{T}}{1+\mathcal{T}} < 1. \tag{3.68}$$

For higher values of r, $\theta''(0) > 0$, so a universal requirement for a steady solution is $r < 1$. Secondly, the existence of a transition zone of thickness $\delta = c\mathcal{D}^{1/2}$ is crucial to the existence of a solution.

Both of these features can be deduced asymptotically by taking the physically realistic limit of small Darcy number $\mathcal{D} \to 0$. Marginal equilibrium (3.54) gives

$$-f'(\eta) \sim \frac{f\theta'}{\mathcal{T}} \sim \frac{r\theta'(1)}{\mathcal{T}}. \tag{3.69}$$

But the conditions on the flow (3.38) give

$$f'''_+ \sim \frac{f'_-}{\mathcal{D}} \sim \frac{f'_+}{\mathcal{D}} \qquad (z = \eta - \delta) \tag{3.70}$$

where subscript + denotes the quantity on the transition zone side of the mush–transition zone interface and and subscript − the mush side. These scalings

combine to give

$$1 - \eta \sim a_0 \mathcal{D}^{1/2}, \tag{3.71}$$

where we determine the prefactor a_0 from the asymptotic solution for the flow $f(z)$ and equation (3.69). These yield the quadratic equation for a_0

$$a_0 \left(\frac{c}{2} + \frac{1}{a_0 + c} \right) = \frac{r\theta'(1)}{\mathcal{T}(1-r)}. \tag{3.72}$$

For any finite $c > 0$, this equation has exactly one positive solution a_0. However, for $c = 0$, there are no solutions. Therefore, the transition region is crucial for the existence of steady solutions to the problem.

To gain further insight into the existence of solutions, we differentiate (3.44) with respect to z, to find

$$\theta'''/Pe = f\theta'' - f''(\theta - \mathcal{T}). \tag{3.73}$$

In the mushy layer (excluding the narrow transition zone) $f'' = 0$ and $f > 0$, so θ'' has a definite sign. However, in the transition zone, $f'' \neq 0$ and θ'' changes rapidly (as $\mathcal{D}^{-1/2}$) to satisfy $\theta''(\eta) = 0$ (*cf.* figure 3.8*c*). Given that $\phi(\eta) = 0$, ϕ must increase as z decreases away from the interface $z = \eta$. From equations (3.44, 3.45), this requires $\theta''(\eta^-) < 0$, so $\theta''(0) < 0$, as claimed.

The physical reason why the transition region is crucial can also be inferred from equation (3.73). In the mushy layer, the horizontal velocity is uniform. However, in the transition region it decreases rapidly (*cf.* figures 3.8 and 3.9 for an example of this). This reduction means that horizontal and vertical advection of heat balance the mush–liquid interface, as required by the marginal equilibrium condition (3.54). (Note that only the horizontal velocity changes across the transition region to leading order as $\mathcal{D} \to 0$.)

Furthermore, this asymptotic analysis shows that f, f', θ, θ' and θ'' are all $O(1)$ in the Darcy number, so the full solution for θ and θ' can be found to leading order in the Darcy number by solving (3.44) with linear flow function $f(z) = 1 + C_0 z$ because the mush occupies almost all the domain. Now $C_0 \sim (r - 1)$ and for notational simplicity, we introduce a depth-dependent Péclet

number

$$P(z) = \frac{H\left[Q_1 + (Q_2 - Q_1)z\right]}{\kappa}, \tag{3.74}$$

and difference $\Delta P = P(0) - P(1) > 0$ (if $r < 1$). Then we find the exact solution for the temperature field

$$\theta(z) = \mathcal{T} + K_1 P + K_2 \left[\sqrt{\frac{\pi}{2\Delta P}} P \operatorname{erf}\left(\frac{P}{\sqrt{2\Delta P}}\right) + \exp\left(\frac{-P^2}{2\Delta P}\right)\right], \tag{3.75}$$

where K_1 and K_2 are constants. We determine the constants by imposing the boundary conditions $\theta(0) = -1$ and $\theta(1) = 0$. Thus there is a unique solution that satisfies the boundary conditions, except in the degenerate case of $P(0) = P(1)$ (*i.e.* $r = 1$, the one-dimensional case analysed in section 3.5.3). Note that equation (3.75) holds if $\Delta P < 0$ ($r > 1$), and gives real solutions in terms of the imaginary error function, which is defined by $\operatorname{erfi}(z) = -i \operatorname{erf}(iz)$, where i is the imaginary unit and $\operatorname{erf}(z)$ is the error function. Thus we fully and exactly determine $\theta'(1)$ in terms of Pe, r and $\mathcal{T}$, and hence fully determine a_0 from equation (3.72) in terms of the parameters of the system.

Figure 3.6 gives a regime diagram summarizing the existence of steady solutions in the case of freezing outflow. The sign of $\theta''(z)$ in the mushy layer, which determines the sign of ϕ, separates region **B**, where there are physically meaningful, steady solutions, from regions **A1** and **A2**. One further cause of the non-existence of steady solutions emerges. As Q_2 decreases, the thickness of the liquid region decreases (figure 3.7). For sufficiently large $\mathcal{T}$, the thickness can reach zero for finite Q_2 (equivalently a transect through the regime diagram has entered region **C**), below which there are no steady solutions. This phenomenon is caused by a relatively high conduction of heat in the negative x-direction, which can cause $\theta'(1)$ to become negative, which is inconsistent with marginal equilibrium (3.69).

We study this behaviour by considering the marginal case $\theta'(1) = 0$, which imposes

$$K_1 = -K_2 \sqrt{\frac{\pi}{2\Delta P}} \operatorname{erf}\left(\frac{P(1)}{\sqrt{2\Delta P}}\right). \tag{3.76}$$

To fix ideas, consider the special case $Q_2 = 0 \Leftrightarrow P(1) = 0$. This implies that

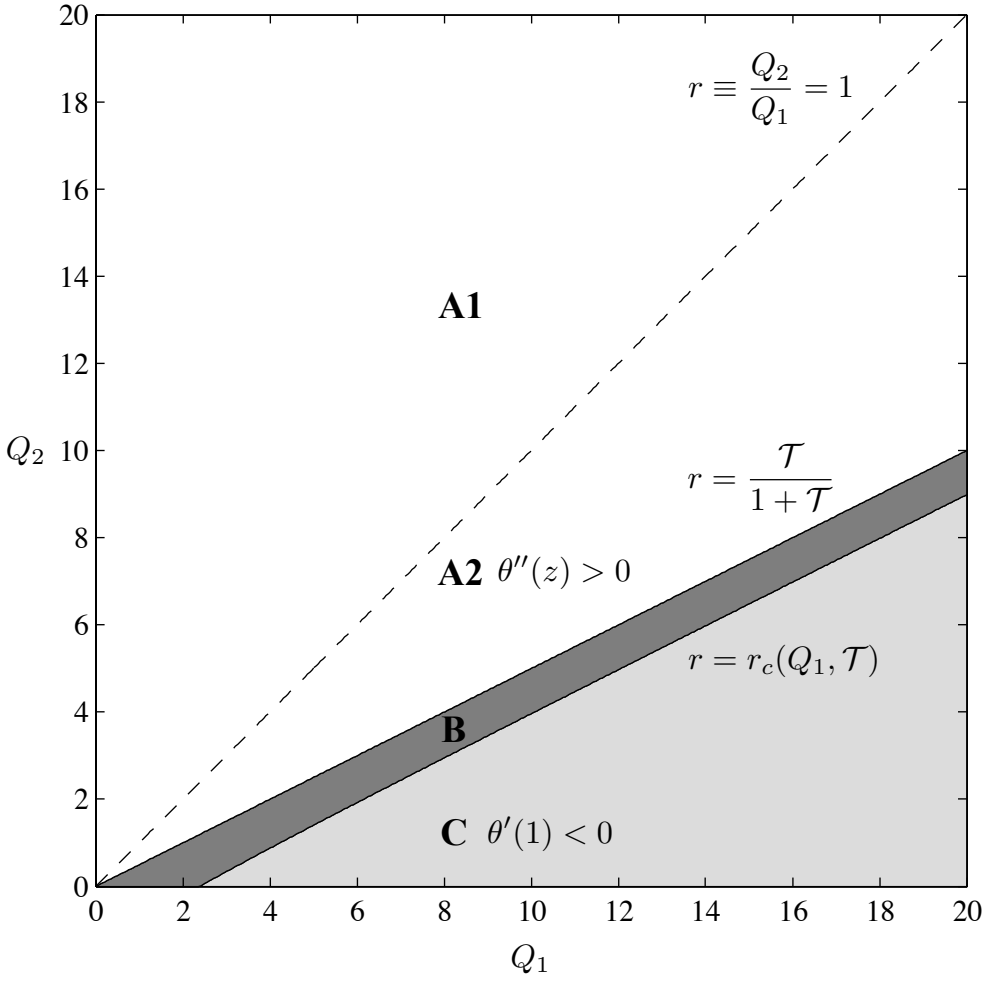

Figure 3.6: A regime diagram in the case of freezing outflow. In region **A1** and **A2**, $\theta'' > 0$ in the mushy layer, which is unphysical since it forces a negative solid fraction. This region is divided into two by the dashed line $r = 1$ ($Q_2 = Q_1$), which separates flow to the left (**A1**) from flow to the right (**A2**). In region **B**, for each pair (Q_1, Q_2), there is a unique physically meaningful solution with $\theta'' < 0$ in the mushy layer, and $\theta'(1) > 0$. The thickness of the liquid region decreases towards region **C**, in which $\theta'(1) < 0$, which means that marginal equilibrium cannot be satisfied. The other parameters are chosen such that $Pe = 1$ corresponds to $Q_1 = 1$, and $\mathcal{T} = 1$. This means that $P(0) = Q_1$ and $P(1) = Q_2$.

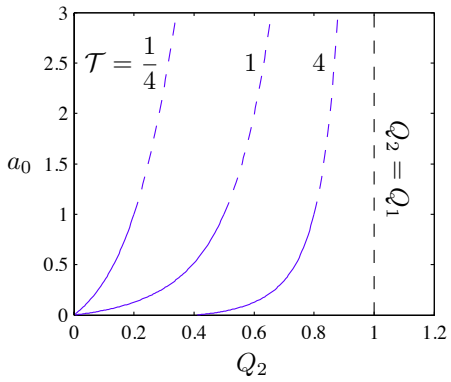

Figure 3.7: A transect through the regime diagram figure 3.6 showing the dependence of the width of the liquid region in equation (3.71) on Q_2 at fixed $Q_1 = 1$, for increasing $\mathcal{T}$. Note that the case $\mathcal{T} = 4$ exhibits both region **C** for small Q_2 and region **B** for larger Q_2. The dashed curves correspond to unphysical solutions in region **A2**, and the fact that this occurs at $a_0 = 1$ for each value of $\mathcal{T}$ is not significant because it is a consequence of the particular choice $c = 1$ in the scaling for the transition region width. All the curves approach infinity before $Q_2 \to Q_1 = 1$.

$K_1 = 0$. Then applying the boundary conditions of θ, we find a critical $\mathcal{T} = \mathcal{T}_C$ satisfying

$$\mathcal{T}_C = \left[\sqrt{\frac{\pi P(0)}{2}}\operatorname{erf}\left(\sqrt{\frac{P(0)}{2}}\right) + \exp\left(-\frac{P(0)}{2}\right) - 1\right]^{-1}. \tag{3.77}$$

Equivalently, this gives a critical $P_0(\mathcal{T})$ (*i.e.* input flux Q_1), above which there are no solutions. Note that $\mathcal{T}_C \sim 2/P(0)$ as $P(0) \to 0$ and $\mathcal{T}_C \sim \sqrt{2/\pi P(0)}$ as $P(0) \to \infty$.

More generally, we find a critical curve (dividing region **B** and **C**) – defined by, say, $P(1) = P(0)r_c(P(0), \mathcal{T})$ – that satisfies a transcendental equation

$$(1+\mathcal{T})\exp\left(-\frac{P(1)^2}{2\Delta P}\right) - \mathcal{T}\exp\left(-\frac{P(0)^2}{2\Delta P}\right) = \mathcal{T}\sqrt{\frac{\pi}{2\Delta P}}P(0)\left[\operatorname{erf}\left(\frac{P(0)}{\sqrt{2\Delta P}}\right) - \operatorname{erf}\left(\frac{P(1)}{\sqrt{2\Delta P}}\right)\right]. \tag{3.78}$$

We have proved that this equation has a solution for all $P(0)$ above the critical value determined earlier. Furthermore, we have shown asymptotically that, for large P,

$$r_c \sim \frac{\mathcal{T}}{\mathcal{T}+1}, \tag{3.79}$$

which also defines the top of region **B**. Thus the region of parameter space where solutions exist becomes asymptotically narrow for large imposed fluxes.

Within narrow region **B** of parameter space, there are solutions specified by equation (3.75), and we show a typical solution in the interior of the region in figure 3.8. Then in figure 3.9, we illustrate the marginal equilibrium condition by showing the tangency of streamlines and isotherms at the mush–liquid interface. For clarity of the liquid and transition regions, we have used a finite value of $\mathcal{D}$. More generally, this seems to slightly increase the size of the region in which physically meaningful solutions can be found from those shown in figure 3.6.

Throughout this section, we have not discussed the solid fraction further than noting that $\theta'' < 0$ in the mushy layer ensures $\phi > 0$. Equation (3.47) shows that

$$\phi = \frac{1}{Pe_V}\frac{\theta' - \theta'(\eta)}{\mathcal{T}-\theta}, \tag{3.80}$$

so ϕ increases as z decreases away from the mush–liquid interface. The requirement that $\phi \leq 1$ gives a critical Pe_V (or V) above which solutions are physically meaningful. One important feature of the case of freezing outflow is that both the size of the solid fraction in the mushy layer and also the concentration in the liquid region are determined everywhere by heat and salt conservation, and not by any imposed external boundary condition.

3.5.5 Conclusions

It is the subtle marginal equilibrium condition that is responsible for the particular (and in some respects peculiar) features of the case of freezing outflow. It imposes conditions on the solution that can only be satisfied in certain parameter regimes. It has the effect of requiring a very narrow liquid region, the size of which scales with $\mathcal{D}^{1/2}$. Dimensionally, the width scales with $\Pi_0^{1/2}$ and so decreases as the permeability of the mushy layer goes to zero. Thus in the formal

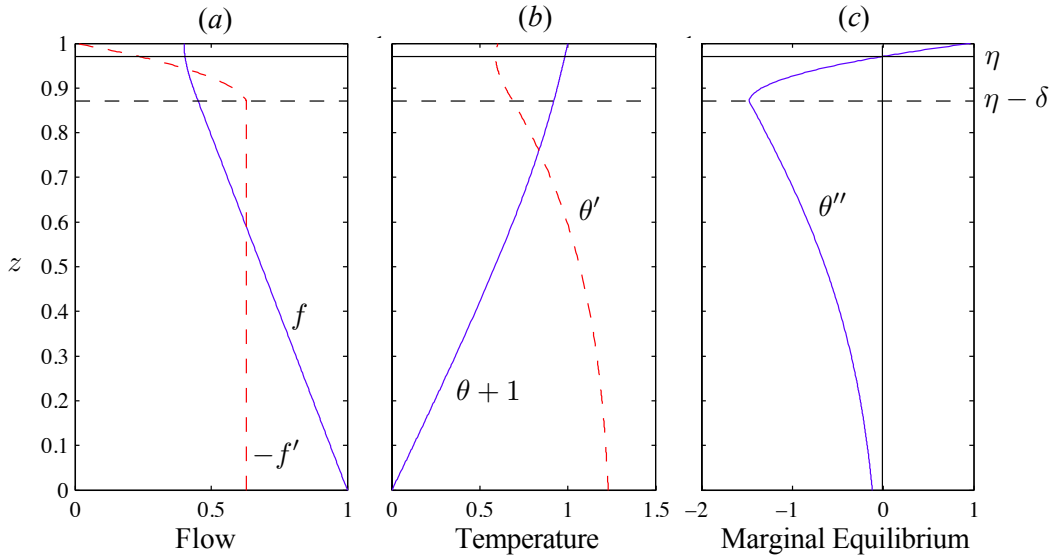

Figure 3.8: A typical solution in the case of freezing outflow at moderately small Darcy number $\mathcal{D} = 0.01$. The transition region between the dashed horizontal line and the solid horizontal line representing the mush–liquid interface has thickness $\delta = 0.1$. Other parameters are $Pe = 4$, $r = 0.4$ and $\mathcal{T} = 1$. (a) the flow function f and the negative of its derivative, showing changes in the vertical and horizontal velocities respectively. (b) the temperature and its derivative. (c) shows that θ'' becomes increasingly negative in the mushy layer and only starts to increase in the transition region, meaning that this region is vital to satisfying $\theta''(\eta) = 0$.

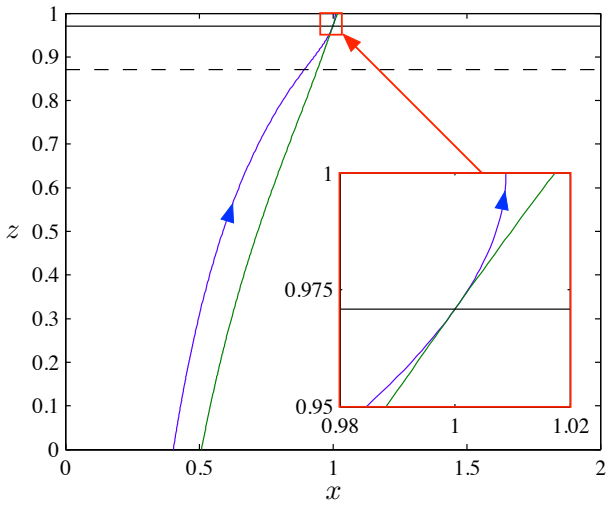

Figure 3.9: The marginal equilibrium condition: a streamline (blue with direction of flow indicated) and an isotherm (green). The marginal equilibrium condition (3.54) that $\boldsymbol{q} \cdot \nabla\theta = 0$ is shown by the tangency of the streamline and isotherm at the mush–liquid interface (see inset). Parameters are as in figure 3.8

asymptotic limit, the liquid region and transition region both scale with $\mathcal{D}^{1/2}$ (as indeed does the pore scale). Nevertheless, the physical mechanisms that give rise to the regime diagram (figure 3.6) still apply at moderate values of $\mathcal{D}$.

In contrast, in the next chapter we consider convection through channels driven by convection. Interestingly, in that case, we find a liquid region size that scales independently of permeability because the strength of convection also depends on the permeability of the mushy layer, indicating the important role that convection plays in keeping liquid chimneys open.

By considering the simple 'toy' problem of solidification with a corner flow, we have understood another feature important in convection. The need for transition region is physically associated with the need for a rapid change in the component of the velocity tangential to the mush–liquid interface. Similarly, in what we later term the active region near a vertical chimney in a mushy layer with convection, the vertical velocity changes sign. In this section, we needed a transition region to cause this change, but in the next two chapters it is convection that causes this change. Thus we can neglect the transition region in subsequent work.

Therefore, in this chapter, we have developed a general theory of mushy layers that we can apply to study convection in a mushy layer in the next chapter, and also clarified important aspects of the boundary conditions at a mush–liquid interface. The coupling of the equations governing heat and salt conservation through the liquidus condition was important in deriving the marginal equilibrium condition and also strongly constrained the region of parameter space in which steady solutions in the corner flow geometry exist. It is necessary to have a continuous normal and tangential velocity when applying the marginal equilibrium condition. Indeed, this was an assumption used in the derivation. In cases where a slip in the tangential velocity occurs between a liquid region and a mushy layer, this boundary condition can be applied by allowing the slip to occur across a transition region with a width that scales with $\mathcal{D}^{1/2}$. Indeed, in the case of a corner flow, this transition region is strictly necessary for the existence of steady solutions.

Chapter 4

Solute Transport in Mushy Layers

The content of this chapter has been published in the Journal of Fluid Mechanics (Rees Jones & Worster, 2013a).

4.1 Introduction

Mushy layers are multiphase systems, and the fluid dynamics of the interstitial liquid can have important influences on the mushy layer. In this chapter, we focus on solute transport within and from mushy layers. A vertical gradient in the density of the interstitial liquid can drive convection, leading to the formation of liquid channels called chimneys (Copley *et al.*, 1970). Convective flows within mushy layers transport solute, leading to segregation between the liquid melt and the mushy layer.

In this chapter, we develop a new simple model of convection in a mushy layer. We investigate the parametric dependence of solute fluxes in the context of convective solutions of the *ideal mushy-layer equations* (Worster, 1997, 2000) introduced in section 3.3.1. This model could be applied to solute transport in a number of fields such as the casting of metal alloys; however, we have been particularly motivated by sea-ice modelling, in which the simplicity of our new model is particularly important. The applicability of mushy-layer theory to sea-

ice modelling has been demonstrated by Feltham *et al.* (2006) and reviewed by Hunke *et al.* (2011).

The fully developed system with chimneys is not amenable to complete analytical treatment. Therefore, some have used an enthalpy-based approach where a single set of equations applies both to the mushy layer and to the liquid melt. Beckermann & Wang (1995) and Boettinger *et al.* (2002) review the use of this type of technique applied numerically to the casting of metal alloys, and Oertling & Watts (2004) apply this technique to sea-ice modelling. Others (Schulze & Worster, 1998; Chung & Worster, 2002; Wells *et al.*, 2010, 2013) have solved separate equations describing the mushy layer and the liquid melt. The computational complexity of such numerical approaches, even with considerable simplifications, means that they are not readily applicable to predictive sea-ice modelling. In sea ice, the spacing of brine channels is of the order of centimetres and so is unresolvable in present-day climate models.

Recently, Wells *et al.* (2010) investigated the dependence of solute flux on chimney spacing and suggested that the spacing takes the value that maximizes the flux. This dynamic *maximum-flux criterion* needs to be tested further but constitutes an objective and transparent way to determine the otherwise unknown chimney spacing. In section 4.2 we develop a simple theoretical framework for modelling fluxes though chimneys using the idealized steady-state solidification arrangement that we introduced in section 3.3.2. This steady-state arrangement can be applied to unsteady situations in which the evolution of the system is much slower than the convective turnover time, as discussed in chapter 6. In section 4.3, we make a patchwork of simplifying approximations, motivated by the case of high Rayleigh number, that captures the essential physics while rendering the problem analytically tractable. We use a vertically linear temperature profile, which would be a good approximation across a thin convecting layer at the bottom of sea ice. This linear profile allows us to find a scaled solution, reducing the full nonlinear two-dimensional internal convection problem to readily solved ordinary differential equations. In section 4.4, we investigate the behaviour of the solution for a planar array of chimneys and the dependence of flux on chimney spacing. Then in section 4.5, we apply the maximum-flux criterion to derive analytically the dependence of heat and solute fluxes on the mush Rayleigh number and on

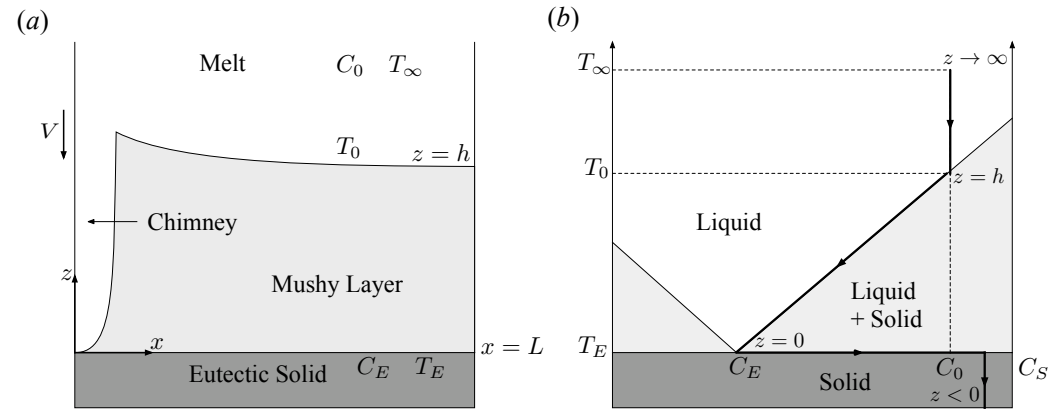

Figure 4.1: (a) diagram of the problem arrangement and (b) the phase diagram showing the phase of the binary alloy as a function of concentration and temperature. The arrows show a trajectory as the system evolves from melt to solid. Note that V is the speed at which the solidification cell is pulled downwards between fixed heat exchangers and equals the rate of solidification.

the other dimensionless parameters of the system.

Finally, in section 4.6, we generalize our model to three dimensions and demonstrate that an array of chimneys can be characterized by the average drainage area alone. We therefore solve the generalisation of our model in detail in an axisymmetric geometry and determine the relationship between solute flux, mush Rayleigh number and the other dimensionless parameters.

This work leads us to propose dimensional relationships not only for solute and heat fluxes through chimneys, but also for the vertical structure of the interstitial flow field and solid fraction distribution. In section 4.7, we discuss these relationships and introduce their applicability to sea-ice models. After chapter 5, the remainder of the thesis from chapter 6 onwards develops this idea further.

4.2 Problem formulation

We consider convection through a mushy layer and chimney as depicted in figure 4.1. A solidification cell, containing a binary alloy whose less dense component is preferentially rejected on solidification, is pulled downwards at a constant speed V through fixed heat exchangers. The steady state has a chimney centred on

$x = 0$ and chimney half-spacing L, as shown in figure 4.1a. The lower heat exchanger is held at the eutectic temperature T_E, below which the alloy freezes completely for all solute concentrations. The far field has temperature T_∞ and solute concentration $C_0 > C_E$, where C_E is the eutectic concentration. Let T_0 be the liquidus temperature corresponding to C_0 and let C_S be the concentration of the solid phase. These quantities are shown in figure 4.1b, which also shows the trajectory through the phase diagram as the system evolves from melt ($z > h$), to mushy layer ($0 < z < h$) and then to solid $z < 0$. The liquidus is assumed to be linear with slope $\Gamma > 0$.

Note that this situation is dynamically equivalent to saltwater (with $C_0 < C_E$) in a cell pulled upwards towards a eutectic heat exchanger, since, in the case of saltwater, the more dense component is preferentially rejected on solidification.

4.2.1 Governing equations

The governing equations were introduced in section 3.3.2. Here we summarize the important equations for this chapter. The single variable

$$\theta = (T - T_E)/\Delta T = (C - C_E)/\Delta C \tag{4.1}$$

describes both temperature T and interstitial concentration C, which is it at local thermodynamic equilibrium. The temperature obeys a combined heat equation

$$\Omega \boldsymbol{u} \cdot \nabla\theta = \nabla^2\theta, \tag{4.2}$$

where

$$\Omega = 1 + \mathcal{S}/\mathcal{C} \tag{4.3}$$

is the factor by which the heat capacity of a mushy layer is enhanced by latent heat release, and $\mathcal{S}$ and $\mathcal{C}$ are the Stefan number and compositional number introduced in section 3.3.2.

Under the further assumption $\mathcal{C} \gg 1$, salt conservation determines the solid fraction

$$\mathcal{C}\phi_z = \boldsymbol{u} \cdot \nabla\theta - \theta_z. \tag{4.4}$$

In a planar geometry the fluid flow is described by a streamfunction ψ of the Darcy velocity $\boldsymbol{u}$ that obeys a vorticity equation

$$\nabla^2\psi = -R_m\theta_x, \tag{4.5}$$

where

$$R_m = \frac{\beta\Delta C g\Pi_0}{\nu V} \gg 1 \tag{4.6}$$

is the mush Rayleigh number, which we assume to be large (frame advection is negligible compared to convective transport).

4.2.2 Boundary conditions

In section 3.4, we discussed the boundary conditions at a mush–liquid interface, such as the interface at the chimney. At the chimney wall, $x = a(z)$, the interstitial liquid flows from the mush into the chimney (the case of 'freezing outflow' from the previous chapter), so the solid fraction is zero there, and marginal equilibrium and heat conservation are expressed by

$$\boldsymbol{u}\cdot\nabla\theta = 0, \qquad \theta_x = (\psi - x)\theta_z \qquad (x = a), \tag{4.7a, b}$$

as shown by Schulze & Worster (1999). This calculation assumes that the chimney is narrow compared to its length, analogous to our asymptotic analysis in section 3.5.4. Conservation of mass at the chimney wall can be expressed by

$$\psi = \frac{a^3}{3\mathcal{D}}\left[\psi_x + R_m(\theta - \overline{C})\right] + a\psi_x \qquad (x = a), \tag{4.7c}$$

where $\overline{C}$ is the average concentration in the chimney (Chung & Worster, 2002). Their calculation uses the lubrication approximation to determine the flow in the chimney. The final term $a\psi_x$ can be neglected if the Darcy number

$$\mathcal{D} = \Pi_0 V^2/\kappa^2 \ll 1. \tag{4.8}$$

We adopt this simplification (taken before $R_m \gg 1$, which ensures $a \ll 1$ and so allows us to apply $(4.7a, b)$ at $x = 0$. Note that, *post hoc* in section 4.5.3, we find

that $a\psi_x$ is asymptotically negligible provided that $R_m^2\mathcal{D} \ll 1$.

Equation (4.7c) is structurally equivalent to the relation found by Schulze & Worster (1998) using a quadratic Polhausen approximation for the concentration field which allows integration of the flow equation (momentum conservation). In our variables, this is expressed by

$$\psi = \frac{a^3}{3\mathcal{D}}\left(\psi_x + R_m\frac{9}{20}\theta\right) \qquad (x = a),$$

which is structurally the same as (4.7c) except for the omitted term $a\psi_x$, which is asymptotically negligible if $\mathcal{D} \ll 1$, but important near the bottom of the chimney. Incidentally, in their numerical calculations, Wells *et al.* (2010, 2013) use the Polhausen approximation but retain $a\psi_x$. In this work we use equation (4.7c), although there is no great difference in terms of the solute flux associated with using the alternatives outlined here provided $R_m^2\mathcal{D} \ll 1$.

At $x = L$ (the dimensionless chimney half-spacing), we apply symmetry boundary conditions, namely

$$\boldsymbol{u}\cdot\boldsymbol{n} = 0 \Rightarrow \psi_z = 0, \qquad \boldsymbol{n}\cdot\nabla\theta = 0 \Rightarrow \theta_x = 0 \qquad (x = L). \tag{4.9a, b}$$

We also impose zero vertical velocity at the lower boundary with the eutectic solid,

$$\boldsymbol{u}\cdot\boldsymbol{n} = 0 \Rightarrow \psi_x = 0 \qquad (z = 0). \tag{4.10}$$

4.3 The Chimney-Active-Passive (CAP) model

We develop a simple model designed to capture the essential dynamics of convection using a patchwork of approximations in different regions (see figure 4.2) as follows.

Away from the chimney (section 4.3.1), we assume a vertically linear and horizontally uniform temperature field. There is no baroclinic torque, since the temperature is horizontally uniform, so this region is essentially 'passive', providing the fluid flux required by the actively convecting near-chimney region.

To determine the strength of this flow, we consider the 'active region' near

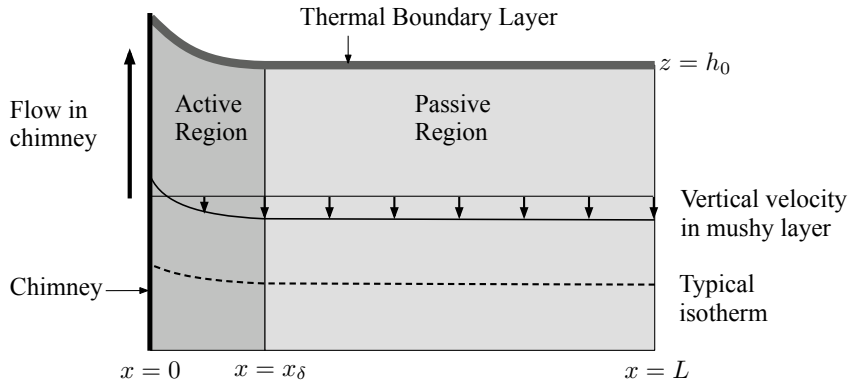

Figure 4.2: The CAP model – showing the active region $x < x_\delta$, passive region $x_\delta < x < L$ and thermal boundary layer to the melt above. The vertical component of the Darcy velocity is uniform and negative in the passive region, and most of the upward flow occurs in the chimney.

the chimney (section 4.3.2) where convection is driven by baroclinic torque. We find a scaled solution to the mushy-layer equations that also has linear vertical temperature variation, and we patch this to the passive region (section 4.3.3).

The flow field in the liquid region is computationally very expensive to find. Therefore we rather balance heat fluxes across a thermal boundary layer to the mush–liquid interface, as suggested by Fowler (1985) and implemented in some numerical studies (Schulze & Worster, 1998; Wells *et al.*, 2010). This gives us a Chimney-Active-Passive (CAP) model.

4.3.1 Passive region – analysis of the bulk mush

Away from the chimney we assume that the temperature field is directly proportional to z and has no horizontal variation. This automatically satisfies the symmetry boundary condition (4.9b). Consistently with this temperature field, we seek a solution for the flow field with horizontally uniform vertical velocity $w = \psi_x$. The streamfunction that satisfies the vorticity equation (4.5) and the boundary conditions (4.9a, 4.10) is

$$\psi \propto z(L - x). \tag{4.11}$$

In contrast to previous numerical studies (Schulze & Worster, 1998; Chung & Worster, 2002; Wells *et al.*, 2010), we do not impose a condition of constant pressure at $z = h$.

The passive region has a uniform depth h_0 since there is no horizontal temperature or vertical velocity variation in this region and the mush–liquid interface is at a constant temperature. The depth h_0 is determined by balancing advection and diffusion of heat across a thermal boundary layer at the mush–liquid interface. This gives (Fowler, 1985)

$$\boldsymbol{n} \cdot \nabla\theta = -\theta_\infty \boldsymbol{u} \cdot \boldsymbol{n} \qquad (z = h_0), \tag{4.12}$$

where $\theta_\infty = (T_\infty - T_0)/(T_0 - T_E)$.

The passive region has a simple structure and flow field, but the strength of this flow must be determined by considering the active region near the chimney.

4.3.2 Active region – scaled solution near the chimney

The reduced mushy-layer equations (4.2) and (4.5),

$$\nabla^2\psi = -R_m\theta_x, \qquad \Omega\boldsymbol{u} \cdot \nabla\theta = \nabla^2\theta, \tag{4.13}$$

admit a scaled solution

$$\psi = z\left(\frac{R_m}{\Omega h_0}\right)^{1/2}\Psi(\eta), \qquad \theta = \frac{z}{h_0}\Theta(\eta), \qquad \eta = x\left(\frac{R_m\Omega}{h_0}\right)^{1/2}, \tag{4.14}$$

that has the same vertical structure as the passive region. The mush–liquid interface is at $z = h(x) = h_0/\Theta(\eta)$.

In terms of the scaled variables (4.14), the reduced mushy-layer equations (4.13) give equations

$$\Theta'' = -\Psi\Theta' + \Psi'\Theta, \qquad \Psi'' = -\Theta', \tag{4.15a, b}$$

and the boundary conditions (4.7a, b) of marginal equilibrium and heat conser-

vation give

$$\Psi'\Theta = \Psi\Theta', \qquad \Theta' = \Psi\Theta/\Omega \qquad (\eta = 0). \tag{4.16a, b}$$

These can be combined to show that the vertical velocity Ψ' is always positive at the chimney wall.

We determine the width of the chimney from mass conservation $(4.7c)$ at the mush–chimney boundary $(x = a)$ as follows. We determine the average concentration in the chimney in terms of our scaled variables. We neglect solute diffusion in the chimney, so $\boldsymbol{u} \cdot \nabla C = 0$ and $C = C(\psi)$ only. Following Chung & Worster (2002), we use the approximation

$$\overline{C}(z) = \frac{1}{\psi(a(z), z)} \int_0^{\psi(a(z),z)} C(\psi)\, d\psi, \tag{4.17}$$

which gives $\overline{C}(z) = (z/2h_0)\Theta_0$ in our scaled variables, and we use the notation $\Theta_0 \equiv \Theta(0)$, for example. Then $(4.7c)$ implies that

$$a \sim \mathcal{D}^{1/3} R_m^{-1/6} \Omega^{-1/6} h_0^{1/6} \alpha, \quad \text{where } \alpha = \left[3\Psi_0/(\Psi_0' + \Theta_0/2)\right]^{1/3}. \tag{4.18}$$

It is important to note that the chimney width a is independent of z, so chimneys are predicted to be straight-sided. Previously unpublished work by J. Ashmore & M. G. Worster (see section 5.2) considers power-law background temperature profiles $\theta \sim z^b$ and shows that $a \sim z^{(1-b)/6}$. Therefore a straight-sided chimney is a consequence of the linear temperature profile we imposed in the passive region. Although our prediction of straight-sided chimneys is a consequence of this linear profile, it is somewhat encouraging to note that this corresponds to some experimental observations, such as those of Schulze & Worster (1998), reproduced in figure 4.3.

4.3.3 Patching conditions

Instead of matching the active and passive regions asymptotically, in our simple model we patch them at a position $x = x_\delta$ (shown in figure 4.2) that is internally determined by applying conditions of continuity of temperature, normal heat flux, normal velocity and pressure there.

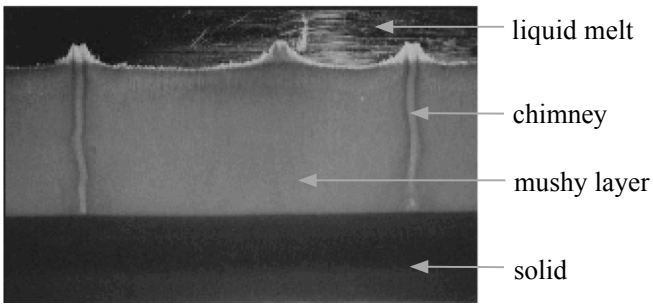

Figure 4.3: From Schulze & Worster (1998). Photograph of an ammonium-chloride solidification experiment, showing narrow vertical chimneys. Note that the mush–liquid interface is peaked near the chimneys and flat in the 'passive zone' further away, which corresponds to our model, shown in figure 4.2.

Let $\delta = x_\delta \left(R_m \Omega / h_0\right)^{1/2}$. Continuity of temperature and normal heat flux require that

$$\Theta(\delta) = 1, \qquad \Theta'(\delta) = 0. \tag{4.19a, b}$$

Then continuity of normal velocity determines the strength of convection in the passive region, so equation (4.11) for the streamfunction in the passive region becomes

$$\psi = z \left(\frac{R_m}{\Omega h_0}\right)^{1/2} \Psi(\delta) \left[\frac{L - x}{L - x_\delta}\right]. \tag{4.20}$$

Applying continuity of pressure, by integrating the vertical component of Darcy's law (3.18), allows us to determine x_δ through

$$L = \left(R_m \Omega / h_0\right)^{-1/2} F(\delta, \Omega)^{-1}, \text{ where } F(\delta, \Omega) \equiv \left(\delta - \Psi(\delta)/\Psi'(\delta)\right)^{-1}. \tag{4.21}$$

Note that $F(\delta, \Omega)$ is an implicit function of Ω, since Ω affects the active-region boundary conditions (4.16). Then equation (4.12) determines the depth of the layer

$$h_0 = \left(-\theta_\infty R_m \Psi'(\delta)\right)^{-1}. \tag{4.22}$$

Substituting this equation back into equation (4.21), we find

$$L = R_m^{-1} \theta_\infty^{-1/2} G(\delta, \Omega), \text{ where } G(\delta, \Omega) = F(\delta, \Omega)^{-1} \left(-\Omega \Psi'(\delta)\right)^{-1/2}. \tag{4.23}$$

4.3.4 Solute and heat fluxes

The flux of salt from the mushy layer to the liquid is equal to the total advective flux of salt into the chimney, which is determined from the solution of the active region. Each half chimney drains a region of mush of length L. Therefore, the average flux of solute per unit length in the x-direction is

$$F_{\text{Solute}} = \frac{1}{L}\int_0^h \left[\psi_z(\theta-1)\right]_{x=0} dz = -\frac{1}{2}R_m\frac{\Psi_0}{\Theta_0}F(\delta,\Omega). \tag{4.24}$$

Note that the solute flux is negative because it is solute-depleted fluid that emanates from the chimney (*cf.* figure 1*b*).

The dimensionless temperature difference between the top of the chimney and the far field is θ_∞ and by symmetry ψ vanishes at the centre of the chimney. Therefore the additional heat flux per unit length, due to convection through chimneys, is

$$F_{\text{Heat}} = \frac{1}{L}\int_0^a \left[\psi_x\theta_\infty\right]_{z=h} dx = -\theta_\infty R_m\frac{\Psi_0}{\Theta_0}F(\delta,\Omega). \tag{4.25}$$

Note that F_{Heat} is negative because the far-field temperature is greater than the temperature at the interface.

These relations can be simply expressed (still dimensionlessly) by

$$F_{\text{Solute}} = -R_m\gamma(\delta,\Omega), \tag{4.26}$$

$$F_{\text{Heat}} = -2\theta_\infty R_m\gamma(\delta,\Omega), \tag{4.27}$$

where

$$\gamma(\delta,\Omega) = \frac{1}{2}\frac{\Psi_0(\delta,\Omega)}{\Theta_0(\delta,\Omega)}F(\delta,\Omega). \tag{4.28}$$

4.3.5 Solutions to the boundary-value problem

The equations (4.15) and boundary conditions (4.16, 4.19, 4.21) constitute a boundary-value problem for the active region, which we solve using a fourth-order Runge–Kutta routine and a Newton-Raphson algorithm to update initial guesses for Ψ_0, Θ_0, and δ. The subsequent chapter (see section 5.3.2 in particular)

considers both the existence and uniqueness of solutions to this boundary-value problem. As discussed there, we restrict attention to solutions that have only one turning point $\Psi' = 0$ as these correspond to upwelling near the chimney and downwelling everywhere else, which is required for consistency with our formulation of the CAP model. This restriction is also consistent with the maximum-flux criterion discussed in section 4.5.

4.4 Results of the model

4.4.1 Discussion of results

The general form of the solution in the reduced CAP model is shown in figure 4.4. It is encouraging to note the similarity with some experiments, such as in figure 4.3, especially in terms of the shape of the mush–liquid interface. We find qualitative agreement with numerical results obtained by Chung & Worster (2002) and Wells *et al.* (2010). Our model reproduces the trend and main features of the dependence of solute flux and depth of the mushy layer found numerically. For example, figure 4.5*a*, *b* can be compared with figure 5*b*, *c* in Chung & Worster (2002).

However, this highly simplified model does not yield quantitative agreement with the results of Chung & Worster (2002). For instance, comparing the above figures, we consistently predict higher solute fluxes. It is not appropriate to undertake a full comparison because Chung & Worster (2002) use relatively high Darcy numbers and quite moderate Rayleigh numbers, a parameter regime in which we do not expect agreement, even before the differing assumptions. Instead, we identify the main causes of discrepancy.

Firstly, we deliberately chose to neglect frame advection in order to render the problem analytically tractable by scaled solution in the active region. However, it is certainly quantitatively important at low to moderate Rayleigh numbers and results in temperature profiles closer to the exponential profiles derived theoretically in the case of no convection (Hills *et al.*, 1983; Worster, 1991) than the linear profile we have assumed. Connected with this, we did not impose a constant pressure at $z = h$, unlike Chung & Worster (2002), which means that

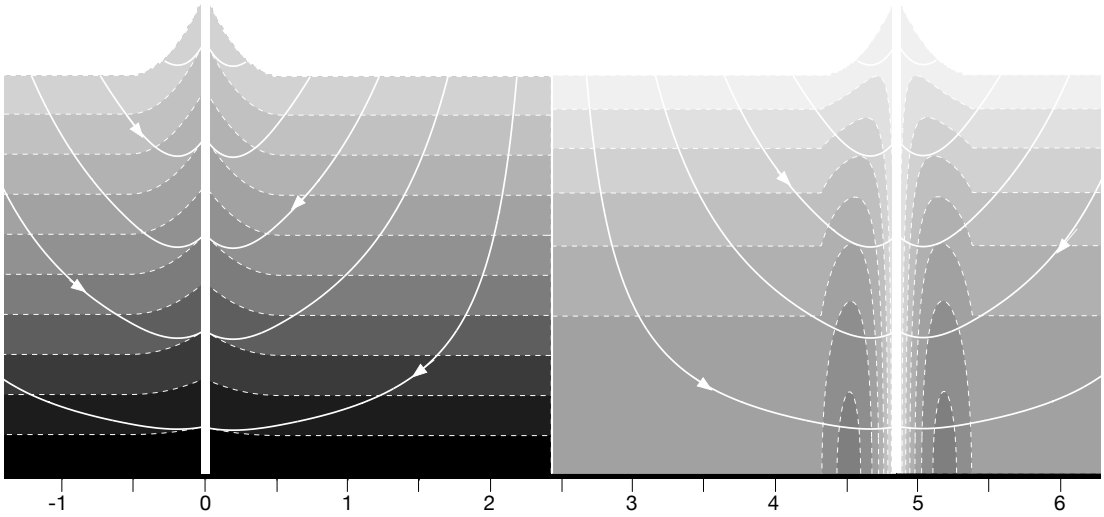

Figure 4.4: A typical solution of the CAP model, showing part of a periodic array of chimneys. Solid white streamlines have arrows that indicate the flow direction. Isotherms in steps of 0.1 (a) and contours of solid fraction in steps of 0.005 (b) are shown by dashed white curves. The latter start at $\phi = 0$ at the mush–liquid interface. For these parameters, chosen for consistency with Chung & Worster (2002), namely $R_m = 12$, $\theta_\infty = 0.4$, $\Omega = 3.5$ $\mathcal{C} = 15$ and $L = 2.426$, the active region occupies about 22% of the domain. The vertical and horizontal scales are the same, and the chimney width is formally zero as the Darcy number $\mathcal{D} \to 0$, but is shown indicatively.

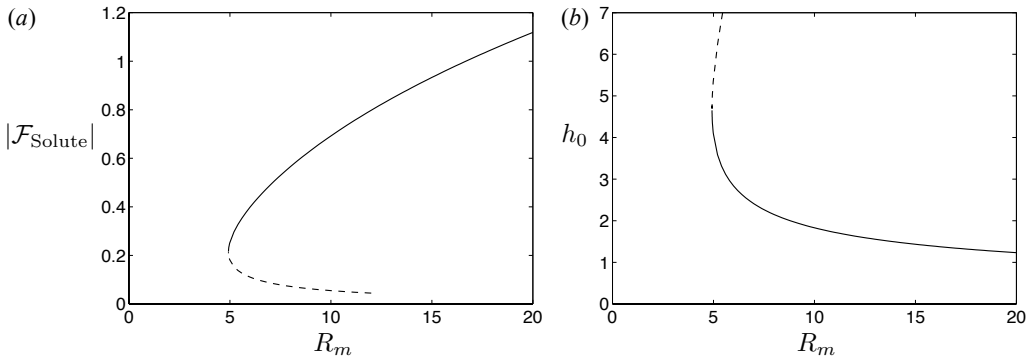

Figure 4.5: Dependence of (a) solute flux F_{Solute} and (b) depth of mush h_0 on Rayleigh number R_m at fixed $L = 2.16$, $\Omega = 1.33$, $\theta_\infty = 0.4$. It is believed that the dashed portions are unstable on the basis of the numerical work of Chung & Worster (2002).

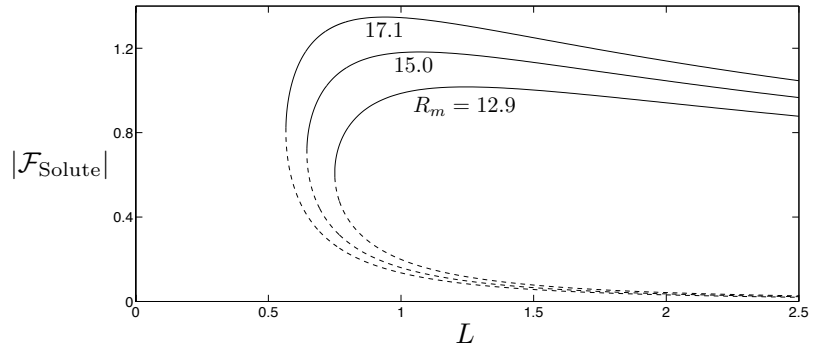

Figure 4.6: The dependence of solute flux on chimney spacing at three different values of R_m. Other parameters are as in figure 4.5. There is a well defined local maximum whose position moves to lower chimney spacing as R_m increases.

the horizontal velocity was not zero there and consequently the flow field has a slightly different shape.

Secondly, we decoupled the heat equation from the salt conservation equation through the effective specific heat capacity Ω and so have neglected the feedback on permeability, which we assumed constant.

4.4.2 Dependence on chimney spacing

The flux of solute and heat through a chimney depends on the size of the convecting cell. Increasing the chimney spacing increases the width of the active region, sustaining a larger flow driven by a greater temperature difference. Therefore the flux into an individual chimney is increased. However, while the average flux per unit length in the x-direction initially increases (above a minimum chimney spacing required to sustain flow), it eventually decreases. There is therefore a maximum flux at some moderate chimney spacing (see figure 4.6). In their numerical study, Wells *et al.* (2010, 2013) observed the existence of such maxima.

Note that for a fixed chimney spacing there is a critical Rayleigh number required to sustain convection as shown in figure 4.5*a* and observed previously (Schulze & Worster, 1998; Chung & Worster, 2002; Wells *et al.*, 2010, 2013). However, in contrast to their findings, as L is increased, this critical Rayleigh number continues to decrease to 0. Therefore, at every Rayleigh number, a sufficiently large box could sustain convection, and we find no overall critical

Rayleigh number. This discrepancy is likely to be caused by our neglect of frame advection, which dominates at low Rayleigh number.

4.5 Maximum-flux criterion

Thus far we have imposed the chimney half-spacing L; but this is undetermined *a priori*. Therefore, we employ the maximum-flux criterion suggested by Wells *et al.* (2010) that L takes the value that maximizes the solute flux from the mushy layer. This approach certainly allows us to compute an upper bound on the solute flux and importantly avoids artificially imposing a horizontal length scale.

As shown in figure 4.6, the flux is a well defined function of chimney spacing on each branch of solutions. Therefore, we combine equation (4.26) for the flux with equation (4.23) for the chimney spacing to find that

$$\left.\frac{\partial F_{\text{Solute}}}{\partial L}\right|_{R_m,\theta_\infty,\Omega} = -R_m^2\theta_\infty^{1/2}\left(\left.\frac{\partial G}{\partial \delta}\right|_{\Omega}\right)^{-1}\left.\frac{\partial \gamma}{\partial \delta}\right|_{\Omega}. \tag{4.29}$$

As illustrated in figure 4.7(a) and discussed further in the next chapter, section 5.4, $G(\delta,\Omega)$ is a well defined function of δ, and $\partial G/\partial\delta$ is strictly positive on the upper branch and strictly negative on the lower branch. Therefore

$$\left.\frac{\partial F_{\text{Solute}}}{\partial L}\right|_{R_m,\theta_\infty,\Omega} = 0 \qquad \Leftrightarrow \qquad \left.\frac{\partial \gamma}{\partial \delta}\right|_{\Omega} = 0. \tag{4.30}$$

4.5.1 Solute fluxes under the maximum-flux criterion

Figure 4.7b illustrates the existence of a unique maximum value of $\gamma(\delta,\Omega)$, which we denote $\gamma_c(\Omega)$. In the case $\Omega\to\infty$, we prove the uniqueness of the maximum in the next chapter, section 5.5. We can determine $\gamma_c(\Omega)$ once and for all by solving the active-region equations independently of all the other external parameters. Therefore, if the maximum-flux criterion holds, equations (4.26) and (4.27) imply

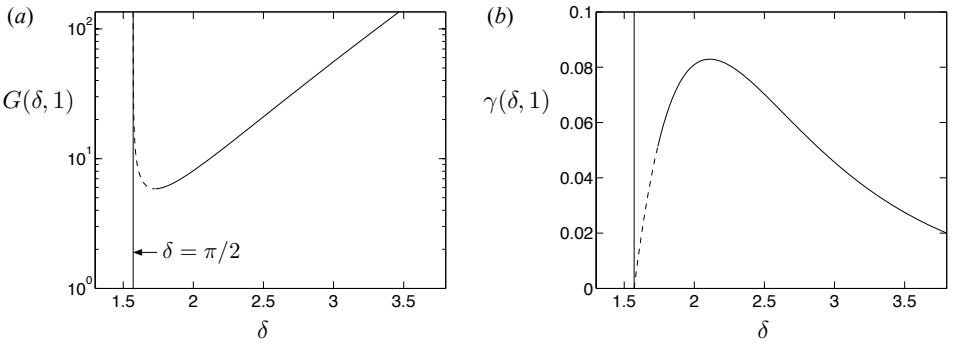

Figure 4.7: (a) shows $G(\delta, \Omega = 1)$, which is proportional to the chimney spacing. The global minimum corresponds to the minimum chimney spacing required to sustain convection. Above this, the two solutions to $G(\delta, \Omega) = G_0$ constant correspond to the two branches in figures 4.5 and 4.6, denoted by the dashed and solid curves. (b) shows $\gamma(\delta, \Omega = 1)$, which is proportional to the solute flux. Below the line $\delta = \pi/2$ there are no solutions of the boundary-value problem, indicating that there must be a finite active region where baroclinic torque occurs in order to drive convection. These results are derived in the next chapter, section 5.4.2.

that

$$F_{\text{Solute}} = -R_m \gamma_c(\Omega), \tag{4.31}$$

$$F_{\text{Heat}} = -2\theta_\infty R_m \gamma_c(\Omega). \tag{4.32}$$

An approximately linear relationship between solute flux and Rayleigh number has also been found using direct numerical simulation of the mushy-layer equations under the maximum-flux criterion (Wells *et al.*, 2010, 2013), although they found a cut-off at low R_m. At sufficiently high R_m, this difference can be neglected, and so our analytic derivation of this relationship under simplifying approximations provides additional assurance of the robustness of their numerical observation obtained by testing across a subset of parameter space.

Additionally, our model, combined with the maximum-flux criterion, reduces the parametric dependence by showing that the flux is independent of far-field temperature θ_∞. Importantly, we have also shown that while the width of the chimney $a \to 0$ in the limit of small Darcy number $\mathcal{D} \to 0$ (*cf.* equation 4.38 below), the flux tends to a constant value. Therefore, to leading order, the flux

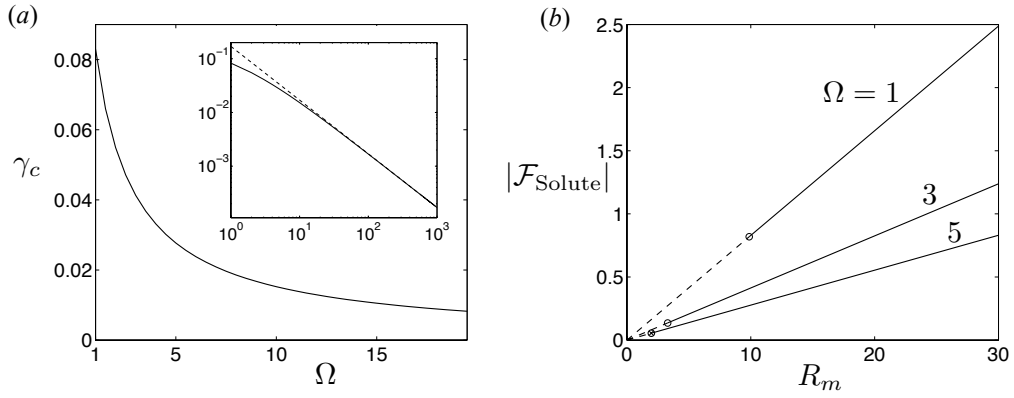

Figure 4.8: (a) The coefficient $\gamma_c(\Omega)$ in the expression for the maximum flux (4.31). Inset shows a log–log plot with the dashed asymptotic result $\gamma_c \sim \Omega^{-1}$, derived in the next chapter, see equation (5.75). (b) shows the relationship between solute flux and Rayleigh number with a cut-off indicated by o, determined from the condition $\Omega R_m = (\Omega R_m)_{\text{crit.}} = \pi^2$ (Huppert & Worster, 2012). Below this, a dashed curve indicates our model results.

depends only on the Rayleigh number and the effective specific heat capacity Ω.

4.5.2 Dependence on Ω

The coefficient $\gamma_c(\Omega)$ in equations (4.31, 4.32) decreases with Ω, as shown in figure 4.8. A high value of Ω, which corresponds to high *dimensional* effective specific heat capacity $c_p\Omega$, reduces the strength of convection within the mush and so reduces solute flux. Mathematically, this is as we expect from the boundary conditions (4.16a, b) which imply that the strength of convection scales with Ω^{-1}, a result that we prove in the next chapter, section 5.5.

However, linear stability analysis shows that the onset of convection is set by $\Omega R_m = (\Omega R_m)_{\text{crit.}}$ (Lapwood, 1948; Huppert & Worster, 2012). Therefore, large Ω makes convection more likely but decreases the resulting solute flux (figure 4.8b).

4.5.3 Vertical transport, solid fraction and length scales

In addition to determining the solute and heat fluxes through chimneys, our model also determines the interstitial velocity within the mushy layer. In particular, we

find that the vertical component w, which controls vertical salt transport within the ice matrix, is

$$w = \begin{cases} -R_m(z/h_0)\,[-\Psi'(\delta)] & \text{passive region } x \geq x_\delta, \\ -R_m(z/h_0)\,[-\Psi'(\eta(x))] & \text{active region } x \leq x_\delta. \end{cases} \tag{4.33}$$

Therefore, the vertical velocity w is proportional to the distance from the eutectic solid and proportional to the Rayleigh number. In the passive region w is independent of x and, since under the maximum-flux criterion $\Psi'(\delta)$ depends only on Ω, we can write

$$w = -R_m(z/h_0)w_c(\Omega), \quad \text{where } w_c(\Omega) = -\Psi'(\delta) > 0. \tag{4.34}$$

To determine the solid fraction ϕ, we integrate equation (4.4), neglecting frame advection, and find that

$$\phi = \begin{cases} w_c(\Omega)\,(R_m/2\mathcal{C})\,[1-(z/h_0)^2] & \text{passive region } x \geq x_\delta, \\ -\Theta''(\eta(x))\,(R_m/2\mathcal{C})\,[\Theta(\eta(x))^{-2}-(z/h_0)^2] & \text{active region } x \leq x_\delta. \end{cases} \tag{4.35}$$

These are equal at the patching boundary x_δ and satisfy the boundary condition $\phi = 0$ at the mush–liquid interface $z = h$. The vertical structure of the solid fraction is therefore quadratic, and contours of ϕ, as well as streamlines, are shown in figure 4.4.

In summary, scalings for the depth of the mush (from equation 4.22), chimney spacing (from equation 4.23), and chimney width (from equation 4.18) are

$$h_0 = R_m^{-1}\theta_\infty^{-1}h_c(\Omega), \tag{4.36}$$

$$L = R_m^{-1}\theta_\infty^{-1/2}L_c(\Omega), \tag{4.37}$$

$$a = R_m^{-1/3}\mathcal{D}^{1/3}\theta_\infty^{-1/6}a_c(\Omega). \tag{4.38}$$

The chimney width a is only weakly dependent on Ω (figure 4.9*b*, *c*). Furthermore, a is independent of the permeability, since both R_m and $\mathcal{D}$ are proportional to Π_0. This is significant because it is often hard to determine Π_0 precisely. The $\mathcal{D}^{1/3}$ scaling for chimney width a corresponds to the scaling of Schulze & Worster

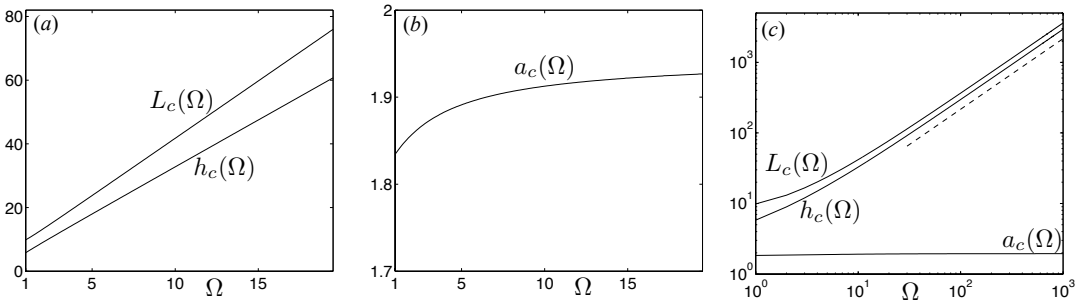

Figure 4.9: (a) The dependence of the horizontal and vertical length scales on Ω. Note also that $w_c = 1/h_c$. (b) The weak dependence of chimney width on Ω. These are shown for a larger range of Ω in (c). The dashed line has slope 1, and both L_c, $h_c \sim \Omega$. The aspect ratio $L_c/h_c \to 1.23$.

(1998) (and verified numerically by Chung & Worster, 2002), although the former paper proposes $a \sim R_m^{-2/9}$. This difference occurs because we have used the maximum-flux criterion to determine the overall horizontal length scale, rather than imposing the chimney spacing.

In equation $(4.7c)$, we assumed $a\psi_x$ was asymptotically negligible compared to ψ. Having determined all the relevant length scales, we observe that this is only valid if $R_m^2\mathcal{D} \ll 1$.

Wells *et al.* (2013) independently identified the scaling $a \sim R_m^{-1/3}\mathcal{D}^{1/3}$ if $R_m^2\mathcal{D} \ll 1$. However, they also proposed the scaling $a = O(R_m^{-1})$ in the limit $R_m^2\mathcal{D} \gg 1$, which comes from balancing ψ and $a\psi_x$ in equation $(4.7c)$. This limit is arguably somewhat problematic, and reflects a more general issue. The underlying continuum approximation of ideal mushy-layer theory can break down in this limit. Strictly speaking, we require that the pore scale is small compared to smallest macroscopic lengthscale in the problem. This means (non-dimensionally) that the chimney width

$$a \gg d \sim \mathcal{D}^{1/2}, \tag{4.39}$$

where d is a typical non-dimensionalized pore size and we have used that the dimensional pore size scales approximately like $\Pi^{1/2}$ (as in the standard Carmen-Kozeny formula). Equation (4.39) is self-consistently satisfied in the scaling $a \sim R_m^{-1/3}\mathcal{D}^{1/3}$ but not in the scaling $a \sim R_m^{-1}$ (although Wells *et al.* (2013) found that

the numerical prefactor was sufficiently small that the approximation is valid). Furthermore, we can determine the scaling for a typical pore Reynolds number

$$Re_p \sim R_m \, \mathcal{D}^{1/2} \sigma^{-1}, \tag{4.40}$$

where σ is the Prandtl number. These observations highlight the danger in investigating the behaviour of these equations at high R_m without ensuring that $R_m \, \mathcal{D}^{1/2}$ is small. Nevertheless these comments only apply to the chimney width, the rest of the calculations are (to leading order) independent of $\mathcal{D}$ and so are much more robust.

Figure 4.9*a*, *c* shows that h_c and L_c depend approximately linearly on Ω. This means the aspect ratio of the convecting cell $L/h_0 \sim \theta_\infty^{1/2}$, and suggests that the convecting cell has aspect ratio of order unity under the maximum-flux criterion. Order unity aspect ratios are often observed in experiments (see figure 4.3 for example).

4.6 Extension of the model to three dimensions

Mushy layers usually form in non-planar geometries, including in sea ice, so it is important to consider potential three-dimensional effects. The whole dynamics of the planar solution are driven by the structure of the active region near the chimney. This suggests that we can reasonably generalize to a three-dimensional mushy layer with distributed chimneys by finding an axisymmetric solution near the chimney and then patching onto an arbitrary passive region. The generalized CAP model is shown in figure 4.10.

In section 4.6.1, we consider an entirely axisymmetric problem in a domain bounded by an outer cylinder of radius R, directly extending the CAP model developed in section 4.3 for a planar geometry. Then in section 4.6.2, we investigate whether and how this can applied to a non-axisymmetric drainage area. Finally, in section 4.6.3, we present results in the axisymmetric geometry.

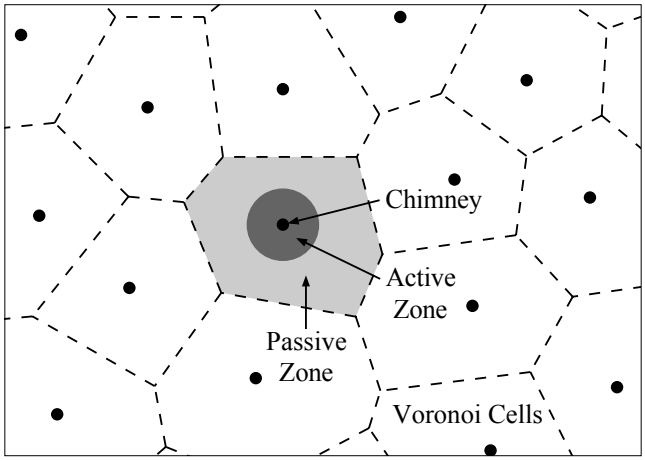

Figure 4.10: Drainage cells (Voronoi cells) in a three-dimensional section of mush, showing the chimneys (black), an active zone (dark grey) and a passive zone (light grey).

4.6.1 Axisymmetric chimney, active and passive zones

The axisymmetric versions of the heat conservation (4.2) and the vorticity equations (4.5) are

$$\Omega(-\psi_z\theta_r + \psi_r\theta_z) = (r\theta_r)_r + r\theta_{zz}, \qquad (\psi_r/r)_r + \psi_{zz}/r = -R_m\theta_r, \qquad (4.41a, b)$$

where in this section ψ denotes the Stokes streamfunction such that

$$\boldsymbol{u} = (-\psi_z/r)\boldsymbol{e}_r + (\psi_r/r)\boldsymbol{e}_z, \qquad (4.42)$$

where r denotes the radial coordinate from the centre of the chimney. The axisymmetric counterparts to the conditions of marginal equilibrium, heat conservation and mass conservation at the chimney boundary (4.7) are expressed by

$$\psi_r\theta_z = \psi_z\theta_r,\ \theta_r = \frac{\psi\theta_z}{r},\ \psi = \frac{a^4}{16\mathcal{D}}\left(\frac{\psi_r}{r} + R_m(\theta - \overline{C})\right) + \frac{a^2}{2}\frac{\psi_r}{r} \quad (r = a). \qquad (4.43a, b, c)$$

To determine a scaled solution for the active region near the chimney, we

introduce the scalings

$$\psi = z\frac{1}{\Omega}\Psi(\eta), \qquad \theta = \frac{z}{h_0}\Theta(\eta), \qquad \eta = r\left(\frac{R_m\Omega}{h_0}\right)^{1/2}, \tag{4.44}$$

where h_0 is the constant depth of the mushy layer in the passive region. This depth is determined by a balance of the heat fluxes across the thermal boundary layer in the liquid melt, as in the planar geometry, and satisfies

$$h_0 = (\theta_\infty R_m w_e)^{-1}, \quad \text{where} \quad w_e = -\Psi'(\delta)/\delta \tag{4.45}$$

is the negative vertical velocity into the passive region. Substituting the scaled variables into the governing equations (4.41), we obtain

$$-\Psi\Theta' + \Psi'\Theta = (\eta\Theta')', \qquad (\Psi'/\eta)' = -\Theta'. \tag{4.46a, b}$$

We employ the same techniques as in the planar geometry to show that $\overline{C} = (z/2h_0)\Theta(\alpha)$. The boundary conditions at the chimney wall (4.43) then become

$$\Psi'\Theta = \Psi\Theta', \quad \Theta' = \frac{\Psi\Theta}{\eta\Omega}, \quad \Psi = \frac{\alpha^4}{16E\Omega w_e}\left(\frac{\Psi'}{\eta} + \frac{\Theta}{2}\right) + \frac{\alpha^2}{2}\frac{\Psi'}{\eta} \quad (\eta = \alpha), \tag{4.47a, b, c}$$

where $\alpha \equiv a\,(R_m\Omega/h_0)^{1/2}$. The solution of the active region only depends on the dimensionless groups Ω and E, where

$$E = R_m^2\mathcal{D}\theta_\infty. \tag{4.48}$$

Note that, unlike in the planar geometry, the limit $\mathcal{D} \to 0$ can no longer be taken nonsingularly because of the geometric constriction of the flow discussed in section 4.6.3. Therefore we retain (4.47c) and use this additional boundary condition to determine the free boundary α.

The passive region is analogous to that in the planar geometry. We apply the conditions $\boldsymbol{u}\cdot\boldsymbol{n} = \boldsymbol{n}\cdot\nabla\theta = 0$ at an outer cylinder $r = R$ and assume a linear thermal field $\theta = z/h_0$. Then by the vorticity equation (4.41b) the Stokes streamfunction that corresponds to horizontally uniform vertical velocity

is $\psi \propto z(R^2 - r^2)$.

We apply the same four physical conditions as in the planar case to derive patching conditions at radius $r = r_\delta$. The thermal patching conditions are

$$\Theta(\delta) = 1, \qquad \Theta'(\delta) = 0, \tag{4.49a, b}$$

where $\delta = r_\delta \left(R_m \Omega / h_0\right)^{1/2}$. Then continuity of normal mass flux, which is equivalent to $[\psi_z / r] = 0$, implies that the Stokes streamfunction in the passive region is

$$\psi = z \frac{1}{\Omega} \Psi(\delta) \frac{R^2 - r^2}{R^2 - r_\delta^2} \qquad r_\delta \leq r \leq R. \tag{4.50}$$

Finally, continuity of pressure, which can be shown to be equivalent to $[\psi_r / r] = 0$, implies that

$$R^2 = R_m^{-2} \theta_\infty^{-1} \Omega^{-1} w_e^{-1} \left(\delta^2 - 2\delta \Psi(\delta) / \Psi'(\delta)\right). \tag{4.51}$$

4.6.2 An approximate solution in an arbitrary geometry

Consider an axisymmetric active region of radius r_δ inside a general passive region. The pressure field that drives the flow in the active region corresponding to the scaled solution determined above is

$$p = \frac{1}{\Omega R_m} \int_\delta^\eta \frac{\Psi(\eta')}{\eta'} \, d\eta' - \frac{z^2}{2h_0} \left(\frac{\Psi'(\delta)}{\delta} + 1 \right). \tag{4.52}$$

In the passive region, we assume a linear temperature profile $\theta = z/h_0$ and then solve Darcy's law (3.18) for the flow. Taking the divergence of Darcy's law, we find

$$\nabla^2 p = -\theta_z \equiv -1/h_0, \tag{4.53}$$

where the right-hand side is constant. We seek a separable solution $p = m(x, y) + n(z)$. Let $n''(z) = n_0$, $\nabla^2 m(x, y) = -m_0$, where m_0 and n_0 are constants satisfying $m_0 = n_0 + 1/h_0$. Note that $n = (z^2/2) n_0$, such that $w = 0$ at $z = 0$.

To patch the solutions, we impose $[p] = 0$ and $[\boldsymbol{u} \cdot \boldsymbol{n}] = 0$ on $x^2 + y^2 = r_\delta^2$.

Firstly, $[p] = 0$ implies that $m = 0$ on $x^2 + y^2 = r_\delta^2$ and

$$n_0 = -\frac{1}{h_0}\left(\frac{\Psi'(\delta)}{\delta} + 1\right), \qquad m_0 = -\frac{1}{h_0}\left(\frac{\Psi'(\delta)}{\delta}\right). \tag{4.54a, b}$$

Secondly, $[\boldsymbol{u}\cdot\boldsymbol{n}] = 0 \Rightarrow [\partial p/\partial r] = 0$. Therefore

$$\left.\frac{\partial m}{\partial r}\right|_{x^2+y^2=r_\delta^2} = (R_m \Omega h_0)^{-1/2}\frac{\Psi(\delta)}{\delta}. \tag{4.55}$$

Integrating $\nabla^2 m(x,y) = -m_0$ over the passive region using the divergence theorem, and applying the boundary condition $\boldsymbol{u}\cdot\boldsymbol{n} = 0 \Rightarrow \partial m/\partial n = 0$ on the outer boundary, we find

$$\left\langle \left.\frac{\partial m}{\partial r}\right|_{x^2+y^2=r_\delta^2} \right\rangle (2\pi r_\delta) = m_0 A_p, \tag{4.56}$$

where $\langle\cdot\rangle$ denotes the azimuthal average and A_p is the area of of the passive region. We substitute equation (4.56) into (4.55) to obtain the final patching condition. Note that if the passive region is axisymmetric then $A_p = \pi(R^2 - r_\delta^2)$ and we recover the patching condition (4.51) obtained previously.

In non-axisymmetric geometries, we can determine the extent of azimuthal variation by finding $m(x,y)$ numerically using a finite-element method (we use the MATLAB PDE Toolbox). Two examples presented in figure 4.11 – square and hexagonal arrays of chimneys with the same total area drained – illustrate the main results. Generically, there is greater azimuthal variation for a square array than a hexagonal array, in which case the variation is usually minimal.

In conclusion, we can approximate a drainage cell of total area A by an axisymmetric region with outer cylinder radius R satisfying

$$R = \left(\frac{A}{\pi}\right)^{1/2}. \tag{4.57}$$

All the patching conditions are satisfied exactly, except $[\boldsymbol{u}\cdot\boldsymbol{n}] = 0$ which is satisfied only in an azimuthally averaged sense, such that mass is conserved globally.

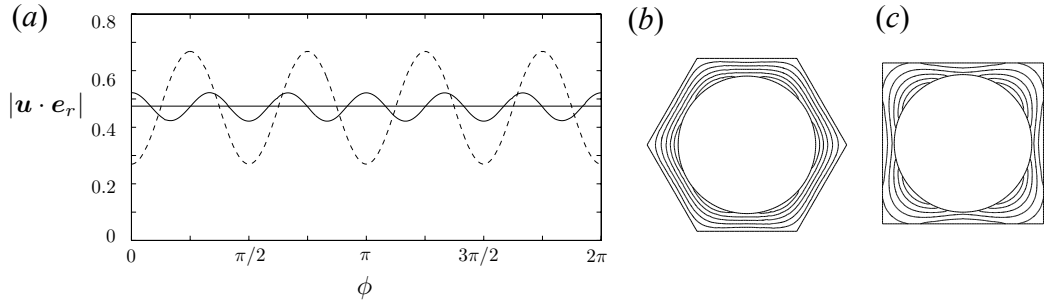

Figure 4.11: Example of the effect of the geometry of the chimney arrangement. (a) Computed radial inflow $|\boldsymbol{u}\cdot\boldsymbol{e}_r|$ for a square $(--)$ and hexagonal $(——)$ array of chimneys as a function of azimuthal angle ϕ in comparison to an axisymmetric passive region (the solid horizontal line). Corresponding contours of $|\nabla m(x,y)|$ in the passive region as shown in (b) for hexagonal and (c) for square arrays. In this example, $R_m = 20$, $\Omega = 4/3$, $\mathcal{D} = 10^{-4}$ and $\theta_\infty = 1.4$, with outer cylinder radius $R = 0.746$, which maximizes the solute flux through the chimney. For these parameters, the azimuthal variation is about 40% for the square array, and 10% for the hexagonal.

4.6.3 Results of the model in the axisymmetric geometry

Having shown that a general drainage cell can be modelled using an axisymmetric cell of the same area, we repeat the analysis of section 4.3.4 in axisymmetry to find the fluxes

$$F_{\text{Solute}} = -R_m\gamma, \tag{4.58}$$

$$F_{\text{Heat}} = -2\theta_\infty R_m\gamma, \tag{4.59}$$

where the multiplying factor,

$$\gamma = \frac{\Psi(\alpha)}{\Theta(\alpha)}\left[\delta^2 - 2\delta\Psi(\delta)/\Psi'(\delta)\right]^{-1} \tag{4.60}$$

can be found by solving the scaled equations for the active region. The size of the active region δ depends on the external parameters, through the radius of the outer cylinder R, under equation (4.51).

We assume that the drainage area takes the value that maximizes the solute flux (section 4.5). As in the planar case, we can satisfy this criterion by finding

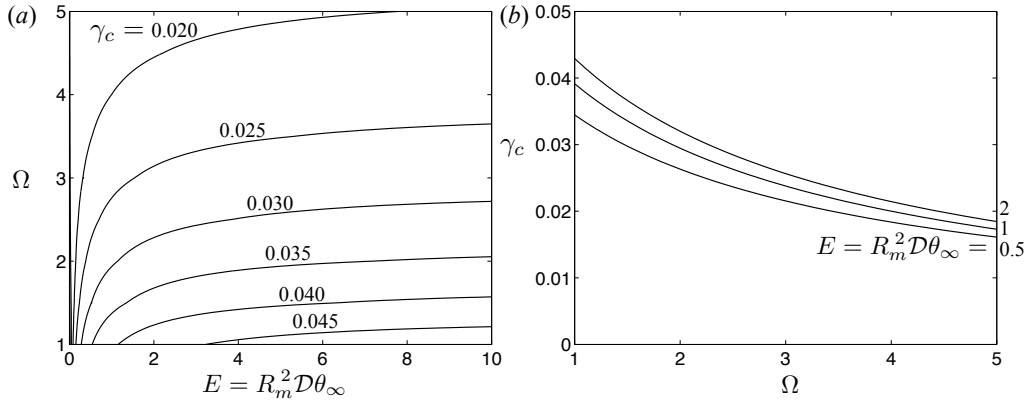

Figure 4.12: Behaviour of the proportionality constant $\gamma_c(E, \Omega)$ in equations (4.61, 4.62). (a) Equally spaced contours of γ_c; note that they are approximately parallel to the E-axis at large E indicating that the γ_c depends principally on Ω in this region. (b) The dependence on Ω at three distinct values of E.

solutions for the active region that satisfy $\partial\gamma/\partial\delta = 0$. In section 4.6.1, we proved that the equations governing the active region depend on only two dimensionless groups: Ω and $E = R_m^2 \mathcal{D}\theta_\infty$. Therefore, under the maximum-flux criterion,

$$F_{\text{Solute}} = -R_m \gamma_c(\Omega, E), \tag{4.61}$$

$$F_{\text{Heat}} = -2\theta_\infty R_m \gamma_c(\Omega, E). \tag{4.62}$$

Figure 4.12 shows the behaviour of the proportionality function $\gamma_c(E, \Omega)$ in these equations, and can be used to derive and interpret the relationships between solute flux and Rayleigh number developed in section 4.6.4.

However, it is important first to note that in axisymmetry there are additional geometric factors that complicate the dependence of flux on drainage area. In particular, mass conservation $\nabla \cdot \boldsymbol{u} = 0$ means that in the axisymmetric geometry, unlike the planar geometry, the flow is constricted as $r \to a^+$.

Flow constriction gives rise to two distinct modes of convection at certain parameter values. Mode I (figure 4.13a) has a relatively small drainage area and weaker flow. Mode II (figure 4.13b) has a relatively large drainage area which supports a bigger temperature contrast and hence greater flow rates but similar solute fluxes per unit area drained. As R_m increases, the strength of convection

increases, which leads to geometric constriction becoming more significant. This inhibits mode II relative to mode I (figure 4.13*c*, *e*). This complicating detail has a minimal effect on the solute flux (figure 4.13*d*). Under the maximum-flux criterion, there is a transition to a greater number of relatively weak chimneys as R_m increases (a transition to mode I at high R_m). This fact, as well as the observation that a much greater fraction of the volume flux occurs through the chimney in mode I, consistent with the formulation of the CAP model, leads us to expect that mode I will occur generically. Therefore, a hexagonal array of chimneys would have the form shown in figure 4.14, which is similar in appearance to the photograph of ammonium chloride solidifying in a rectangular tank by Huppert (1990), his figure 19*c*).

4.6.4 Relationships between solute flux and Rayleigh number

In axisymmetry, we find nonlinear relationships between solute flux and Rayleigh number, as shown in figure 4.15. The precise form of these relationships depends significantly on Ω, and somewhat more weakly on $\mathcal{D}$ and θ_∞. The departure from linearity arises from the different behaviour near the chimney, especially in terms of the geometric constriction of the flow discussed previously.

We firstly consider the dependence on the Darcy number $\mathcal{D}$ and far-field temperature of the melt θ_∞. These parameters only appear multiplied together in the group $E = R_m^2 \mathcal{D}\theta_\infty$, so we need only consider the product $\mathcal{D}\theta_\infty$.

In the planar geometry $\mathcal{D}$ and θ_∞ did not affect the maximum solute flux at all. However, they do affect the chimney radius, which in axisymmetry controls the significance of geometric constriction, and hence they affect the solute flux (see equation 4.47*c*).

Nevertheless, the slopes of the curves in figure 4.15*b* are approximately the same across a wide range of $\mathcal{D}\theta_\infty$ (we observe that this statement holds better at higher Ω, so figure 4.15*b* represents the 'worst-case scenario' $\Omega = 1$). Therefore, in some circumstances it is appropriate to seek an approximate relationship between flux and Rayleigh number that is independent of both $\mathcal{D}$ and θ_∞, a further major parametric simplification, as we now do.

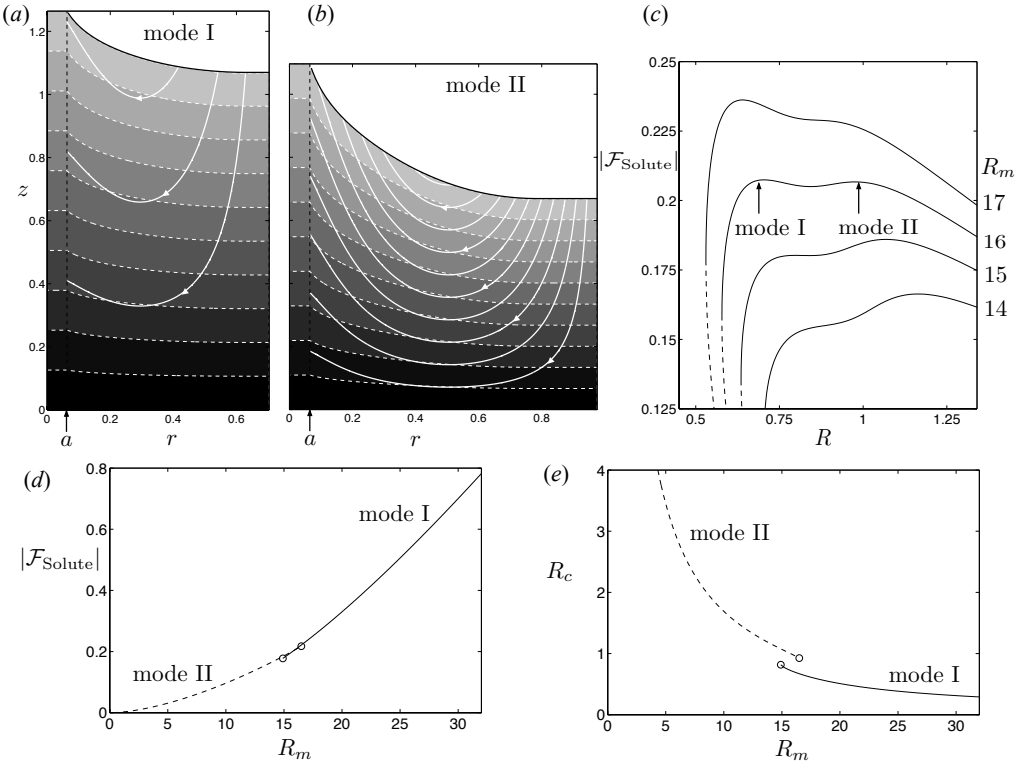

Figure 4.13: (a, b) The two modes of convection (I, II) for parameters $R_m = 16$, $\theta_\infty = 1.4$, $\mathcal{D} = 1 \times 10^{-4}$ and $\Omega = 1$. Isotherms (dashed white curves), streamlines of Darcy velocity (solid white curves) and the chimney radii at $r = a$ are shown. (c) Solute flux against drainage cell radius R and the change in which local maximum (mode) has the greater flux as we increase R_m from 14 to 17; the dashed curves are lower branches of solutions, analogous to those in figure 4.6. The transition between modes is shown in (d, e) with open circles indicating the value of R_m where is there is no longer a local maximum in solute flux corresponding to the mode. (d) The maximum value of solute flux and (e) the drainage cell radius $R = R_c$ at which the flux is maximized. At higher values of Ω, the transition is rapid, but no longer discontinuous in R_c.

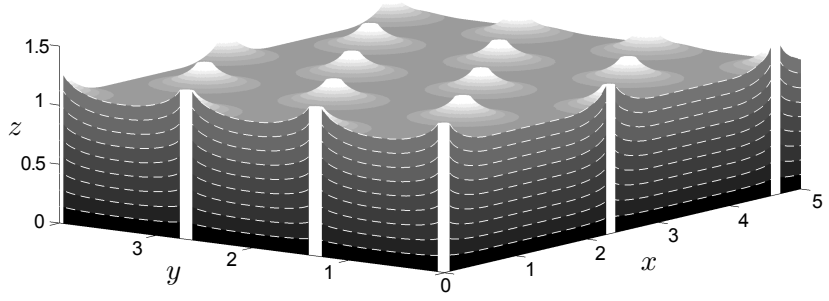

Figure 4.14: A hexagonal array of chimneys corresponding to mode I in figure 4.13. The thin white dashed curves are isotherms while thicker vertical white regions are chimneys.

We secondly consider the dependence on Ω. Both the degree of nonlinearity and the gradient of the slope of the graph of flux against Rayleigh number depend significantly on the value of Ω, as shown in figure 4.15*a*. For low R_m, the flux does not depend strongly on Ω because to some extent the weaker convection caused by increasing Ω (as found in the planar case) is compensated by the lesser importance of geometrical constriction. However, at high R_m, when the smaller, weaker chimney mode of convection dominates, the solute flux is considerably lower at higher values of Ω. Indeed, at high R_m we can approximate the relationship between flux and Rayleigh number by a linear flux law

$$F_{\text{Solute}} = R_m \tilde{\gamma}_c(\Omega) - c, \quad \text{where } c \text{ is constant.} \tag{4.63}$$

The gradient $\tilde{\gamma}_c(\Omega)$ decreases with Ω, as shown by considering any of the curves in figure 4.12*b*.

4.7 Concluding discussion and applications

Convection in a mushy layer can be modelled simply using a series of approximations that capture the underlying physics while reducing a two-dimensional problem (either planar or axisymmetric) to solving ordinary differential equations. In planar geometry, we deduced analytically that the solute and heat fluxes through

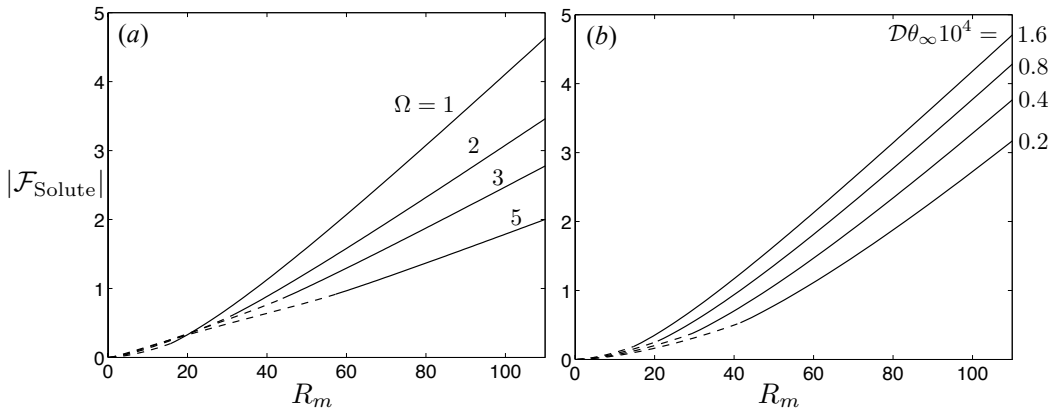

Figure 4.15: Relationships between solute flux and Rayleigh number in axisymmetry. (a) The relationships at different values of Ω for fixed $\mathcal{D}\theta_\infty = 1.4 \times 10^{-4}$. These become approximately linear at high R_m. In (b) we use different values of $\mathcal{D}\theta_\infty$ but fixed $\Omega = 1$. The solid parts of the curves correspond to mode I behaviour, and the dashed parts to mode II behaviour.

the chimney are proportional to the mush Rayleigh number, with the proportionality depending on only one parameter. In axisymmetric geometry, we found that this proportionality function depended on two dimensionless groups Ω and $E = R_m^2 \mathcal{D}\theta_\infty$. This gave rise to the possibility of nonlinear relationships between the solute flux and the mush Rayleigh number R_m.

At a foundational level, nonlinearity arises from the presence of an additional length scale. The planar problem has only one length scale, the thermal length scale κ/V, and so on dimensional grounds the solute flux must be proportional to the Rayleigh number at high Rayleigh number. By contrast, in the axisymmetric problem geometrical constriction that occurs over a length scale that depends on the chimney radius introduces an additional length scale. Non-dimensionally, this means that the solute flux can depend on the Darcy number in axisymmetry, in which case there is a nonlinear relationship between solute flux and Rayleigh number.

Nevertheless, for large R_m and only moderate variation in $\mathcal{D}\theta_\infty$, this nonlinearity is weak, particularly at the moderately large values of Ω relevant to sea-ice formation. Furthermore we showed that the fully three-dimensional problem can be approximated well by an axisymmetric region of the same drainage

area. Therefore we propose the *dimensional* approximations

$$F_{\text{Solute}} \sim -V(C_0 - C_E)R_m\gamma_c(\Omega), \tag{4.64}$$

$$F_{\text{Heat}} \sim -2\rho c_p V(T_\infty - T_0)R_m\gamma_c(\Omega), \tag{4.65}$$

in which the following non-dimensional parameters of the system appear

$$R_m = \frac{\beta(C_0 - C_E)g\Pi_0}{\nu V}, \quad \Omega = 1 + \frac{\mathcal{L}}{(C_S - C_E)\Gamma c_p}.$$

The flux law (4.64) simplifies the parametric dependence of the solute flux caused by convection in a mushy layer. Solute flux depends quadratically on driving concentration difference $(C_0 - C_E)$ and linearly on permeability Π_0. It is independent of both the solidification rate V and the thermal diffusivity κ, which together set the overall thermal length scale κ/V.

Our modelling approach provides additional evidence of the robustness of the linear solute flux law in planar geometry, which was first proposed by Wells *et al.* (2010) on the basis of numerical work over a range of values of R_m and $\mathcal{C}$, holding θ_∞ and $\mathcal{S}$ constant (note that $\Omega = 1 + \mathcal{S}/\mathcal{C}$). In particular, we were able to find this law (at least for high R_m) across a broader range of parameter values.

Crucially, we were able to extend this approach into axisymmetry. The possibility of nonlinearity does suggest that caution should be used in applying the planar flux law to three-dimensional problems, and suggests that variation in $\mathcal{D}\theta_\infty$ should be moderate in order to do so.

It is also interesting to note that, for both geometries, we reproduce the ratio of solute flux to heat flux found by the scaling analysis of Worster (1991) and successfully used to explain the evolution of the melt region in experiments (Worster, 1992*a*). That analysis left a factor in the flux laws undetermined, which did not affect the ratio. However, we improve on that study by determining this factor in terms of the non-dimensional parameters.

Furthermore, our approach demonstrates the need for a finite active region where baroclinic torque occurs in order to drive the entire convective flow through the chimneys. Our analytical approach also reveals the connection between straight-sided chimneys and a linear temperature field, both ideas that we justify

fully in the next chapter.

Although not capable of producing quantitative agreement with the direct numerical simulations of Chung & Worster (2002) and Wells *et al.* (2010, 2013), for reasons discussed earlier, our model does capture the same dynamics as numerical simulations. This suggests that it could be used as the basis of a dynamically informed parameterization of brine fluxes within and from sea ice. The types of simplification used in our model are consistent with current models for sea ice. These use a low vertical resolution (so a linear temperature profile is a reasonable approximation when only the bottom several centimetres of sea ice actively convect, as is typical) and also use an effective heat capacity, analogous to Ω.

Significantly, our model allows us to determine the vertical transport within sea ice and hence also its bulk salinity, which evolves according to equation (3.7). Along with temperature, bulk salinity is the main variable of interest to modellers. Our results for the vertical transport, which have the same structure in both planar and axisymmetric geometry, could be applied to model the actively convecting region at the bottom of sea ice in a one-dimensional fashion, thereby accounting for the effects of convection semi-analytically. In particular, within the passive region, where there is no horizontal variation, we find the *dimensional* result

$$w = -VR_m w_c\,\zeta, \tag{4.66}$$

where ζ, which equals z/h_0 in our formulation, in general denotes the ratio of the distance into the convecting region to the depth of that region, and the appropriate interstitial concentration difference ΔC in the Rayleigh number is that across the convecting layer only, an idea that we use to derive an *effective* Rayleigh number in chapter 6. We then use this to parameterize the convective transport of heat and salt in a one-dimensional model of sea ice in chapter 7. Thus our simple model of convection in a mushy layer is applicable to developing a model for sea ice in which its salt content and salt fluxes to the ocean are determined dynamically.

Chapter 5

Mathematical Insights into the CAP Model

The content of this chapter has been published in the Journal of Fluid Mechanics (Rees Jones & Worster, 2013a): a very condensed version of section 5.2 as an appendix to the paper, and sections 5.3–5.5 as supplementary material.

This chapter explores some of the more mathematical aspects of the Chimney-Active-Passive (CAP) model introduced in the previous chapter. It is not essential to the main direction of the thesis, which we resume in the following chapter in which we apply the CAP model to gravity drainage in sea ice, but nevertheless yields helpful physical insights into convection in a mushy layer. We compare porous medium (mushy layer) convection at a chimney with an unstable far-field density profile to convection with a uniform far-field density (the simplest example of which is convection at a heated plate). We show that important differences arise from the unstable far-field density profile.

5.1 Introduction

The CAP model of convection in mushy layers (chapter 4) involves a chimney, an active region and a passive region. Previous analytical scaling studies such as Worster (1991) amounted to considering a chimney and active region without

the connection to the passive region. These were unable to fully determine solute fluxes from mushy layers. This raises the question as to why the CAP model is able to do so.

In this chapter, we first consider why we need a finite, bounded domain (with a passive region) by finding boundary-layer solutions to the mushy layer equations in an infinite mush (section 5.2). This approach amounts to considering a model that only has an unbounded active region. Conversely, we then consider the finite boundary-value problem associated with a bounded active region (section 5.3 onwards). This allows us to explain why the active region is needed to sustain convection. Together, this chapter uses mathematical insights into the CAP model to explain further the physical mechanisms driving convection in a mushy layer.

5.2 Boundary-layer solutions near a chimney

5.2.1 Scaling of the chimney width

In unpublished work by J. Ashmore & M. G. Worster, scaling relationships were discovered between the shape of the vertical temperature variation in a mushy layer and the width of a chimney as follows. Their work was performed in the limit $\mathcal{S} \ll \mathcal{C}$ which is equivalent to $\Omega = 1$, since $\Omega = 1 + \mathcal{S}/\mathcal{C}$. However, in the following presentation we generalize to $\Omega > 1$.

Consider an isolated chimney in a semi-infinite (both vertically and horizontally) mushy layer. Look for a boundary-layer similarity solution of the heat conservation (4.2) and vorticity (4.5) equations, appropriate to high Rayleigh number, with far-field conditions

$$\theta \to cz^b, \qquad \psi_x \to 0 \qquad (x \to \infty). \tag{5.1a, b}$$

In the boundary layer, the dominant balances in equations (4.2) and (4.5) become

$$\Omega(-\psi_z\theta_x + \psi_x\theta_z) \sim \theta_{xx}, \qquad \psi_{xx} \sim -R_m\theta_x. \tag{5.2a, b}$$

This is analogous to our active region. There are similarity scalings

$$\psi = \left(\frac{cR_m}{b\Omega}\right)^{1/2} z^{(1+b)/2}\,\Psi(\eta), \quad \theta = cz^b\Theta(\eta), \tag{5.3}$$

where Ψ and Θ satisfy ordinary differential equations, and

$$\eta = \frac{x}{d(z)}, \qquad d(z) = \frac{z^{(1-b)/2}}{(bcR_m\Omega)^{1/2}}. \tag{5.4}$$

We substitute the similarity solution into equation (4.17) to find that the average concentration in the chimney is $\overline{C} \sim cz^b\Theta_0(1+b)/(1+3b)$. Recalling equation (4.7c) for mass conservation, we substitute the similarity solution and neglect the final term as asymptotically small in the limit $\mathcal{D} \to 0$ to find

$$a \sim \frac{\mathcal{D}^{1/3}}{(cR_m\Omega)^{1/6}} z^{(1-b)/6}\alpha(b), \tag{5.5}$$

where

$$\alpha(b) = \left(\frac{3\Psi_0(1+3b)}{b^{1/2}\left[(1+3b)\Psi_0' + 2b\Theta_0\right]}\right)^{1/3}. \tag{5.6}$$

Therefore, $a \propto z^{(1-b)/6}$ and so straight-sided chimneys correspond precisely to linear ($b = 1$) far-field temperature profiles. Note that equation (5.5) reduces to equation (4.18) for the chimney width in the CAP model if $b = 1$ and $c = 1/h_0$.

Now Ψ and Θ satisfy ordinary differential equations

$$-\left(\frac{1+b}{2b}\right)\Psi\Theta' + \Psi'\Theta = \Theta'', \qquad \Psi'' = -\Theta'. \tag{5.7a, b}$$

Furthermore, if $\mathcal{D} \ll 1$, the chimneys are narrow and to leading order we can apply the remaining boundary conditions (4.7a, b) at $x = 0$, as discussed in chapter 4. In terms of the similarity variables these give

$$-\left(\frac{1+b}{2b}\right)\Psi\Theta' + \Psi'\Theta = 0 \qquad \Omega\Theta' = \Psi\Theta \qquad (\eta = 0). \tag{5.8a, b}$$

The far-field conditions $(5.1a, b)$ give

$$\Theta \to 1, \qquad \Psi' \to 0 \qquad (\eta \to \infty). \tag{5.9a, b}$$

5.2.2 Solutions of the boundary-layer equations

The similarity (boundary layer) equations behave as follows. Equation $(5.7b)$ can be integrated directly, and far-field conditions $(5.9a, b)$ applied, to give

$$\Psi' = 1 - \Theta. \tag{5.10}$$

This leads to a third-order equation for Ψ, from equation $(5.7a)$,

$$\Psi''' + \frac{1+b}{2b}\Psi\Psi'' + \Psi'(1-\Psi') = 0 \tag{5.11}$$

subject to conditions, from equations $(5.8a, b)$ and $(5.9b)$,

$$\left(\frac{1+b}{2b}\right)\Psi\Psi'' + \Psi'(1-\Psi') = 0 \qquad (\eta = 0), \tag{5.12a}$$

$$\Omega\Psi'' + \Psi(1-\Psi') = 0 \qquad (\eta = 0), \tag{5.12b}$$

$$\Psi' \to 0 \qquad (\eta \to \infty). \tag{5.12c}$$

These equations can be solved using a shooting method. The following solutions extend the previous work of J. Ashmore and M. G. Worster in the important respect of drawing out the continuous, rather than discrete, nature of the family of solutions appropriate to the case of an infinite domain (rather than the large but finite domain that they previously studied). These solutions can be characterized in terms of $\Psi'(0)$ as follows.

If $\Psi'(0) > 1$, then $\Psi'(\eta) > 1$ for all η so cannot satisfy the far-field condition $(5.12c)$. Indeed Ψ then tends to infinity in a number of possible ways depending on b. The dominant balance for large Ψ in equation (5.11) is $(1+b)\Psi\Psi'' = 2b(\Psi')^2$. Integrating this once we find $\Psi'\Psi^{-2b/(1+b)} = A_0$, where A_0 is constant. Then we

obtain the following solutions

$$\begin{aligned}
&\Psi(\eta) \sim A_1 \eta^{(1+b)/(1-b)} && (b < 1,\ \eta \to \infty),\\
&\Psi(\eta) \sim A_2 e^{A_0 \eta} && (b = 1,\ \eta \to \infty),\\
&\Psi(\eta) \sim (A_4 - A_3 \eta)^{(1+b)/(1-b)} && (b > 1,\ \eta \to \infty),
\end{aligned}$$

where A_1–A_4 are constants. These solutions correspond, respectively, to algebraic growth, exponential growth and finite blow-up.

There is a transition in behaviour at $\Psi'(0) = 1$. In this case $\Psi'(\eta) = 1$ for all η, which also does not satisfy the far-field boundary condition.

If $1 > \Psi'(0) > 0$ then $\Psi' \to 0$ and $\Psi \to \Psi_\infty$ as $\eta \to \infty$. Note that Ψ_∞ depends on $\Psi'(0)$. There is a critical value $\Psi'_C(0)$, which depends on b and Ω, such that this decay is monotonic and (asymptotically) exponential if $\Psi'(0) \geq \Psi'_C(0)$ and oscillatory if $\Psi'(0) < \Psi'_C(0)$. This critical value corresponds to $\Psi_\infty = 4b/(1+b)$ since at large η the dominant balance in (5.11) is

$$\Psi''' + \frac{1+b}{2b}\Psi_\infty \Psi'' + \Psi' = 0, \tag{5.13}$$

which has solutions $e^{m\eta}$ where $m = 0$ or

$$2m = -\left(\frac{1+b}{2b}\Psi_\infty\right) \pm \sqrt{\left(\frac{1+b}{2b}\Psi_\infty\right)^2 - 4}. \tag{5.14}$$

In the case of exponential decay, this negative root decays rapidly away and we observe numerically that the positive root describes the asymptotic behaviour as shown in figure 5.1. The critical value is a well-defined function of (b, Ω) and is best found by shooting for the far-field value of Ψ. Numerically we find that increasing b leads to increased damping and so a higher critical value. Conversely Ω represents the heat capacity so increasing it reduces the strength of the flow and so leads to a lower critical value. Both of these trends are shown in figure 5.2.

It is significant that the continuous spectrum of solutions has an unbounded

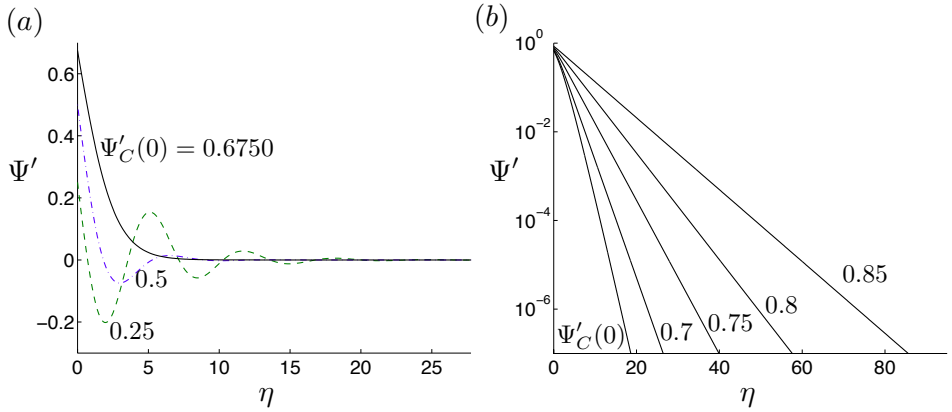

Figure 5.1: (a) oscillating solutions to the similarity equations and the critical solution. (b) shows the exponential decay of the similarity solutions with $\Psi'_C(0) \leq \Psi'(0) < 1$. Note the logarithmic scale. In this figure $b = 1$ and $\Omega = 1$.

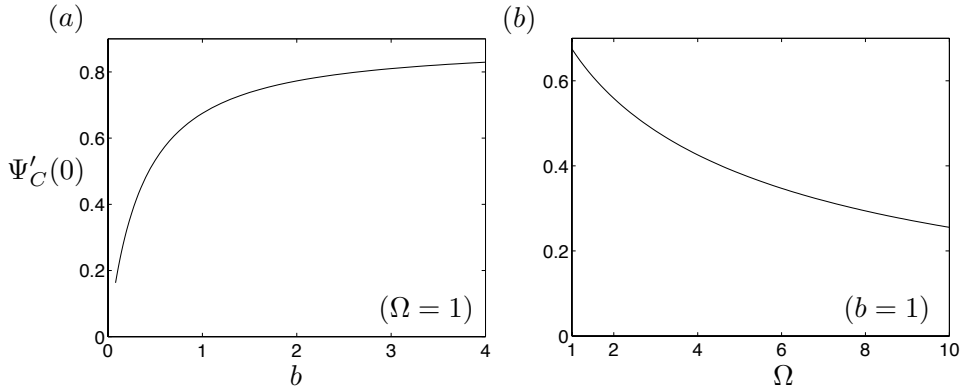

Figure 5.2: (a) critical value of $\Psi'(0)$ as a function of b at fixed $\Omega = 1$. (b) critical value of $\Psi'(0)$ as a function of Ω at fixed $b = 1$.

range of Ψ_∞. For example, when $b = 1$

$$\Psi_\infty < 2 \qquad \Psi'(0) < \Psi'_C(0), \tag{5.15a}$$

$$\Psi_\infty = 2 \qquad \Psi'(0) = \Psi'_C(0), \tag{5.15b}$$

$$\Psi_\infty > 2 \qquad \Psi'(0) > \Psi'_C(0). \tag{5.15c}$$

Physically, this means that required mass flux Ψ_∞ into the boundary layer is unbounded. Later, in section 5.4.3, we contrast this with a bounded active region, in which case the required mass flux is bounded above by the critical value $\Psi_\infty = 2$.

5.2.3 Stability of the boundary-layer solutions

The boundary-layer equations admit a continuous family of solutions, so there is not a unique solution to the boundary-value problem. However, it is possible that the oscillatory solutions are unstable and so would not occur while the monotonic solutions are stable (*cf.* the analogous pure fluid case, Lighthill, 1953). In order to investigate this idea, we consider 'structural' perturbations (with a vertical structure that can be considered within the boundary-layer framework) in the example case $b = 1$. We introduce structural perturbations θ, ψ such that

$$\theta = cz\left[\Theta(\eta) + \theta(\eta)e^{\sigma t}\right], \tag{5.16}$$

$$\psi = (cR_m)^{\frac{1}{2}} z\left[\Psi(\eta) + \psi(\eta)e^{\sigma t}\right]. \tag{5.17}$$

Following the same analysis as for the base state, we can integrate one of the resulting equations to find $\theta = -\psi'$ and then the other equation becomes

$$(1 - 2\Psi' - \tilde{\sigma})\psi' + \psi\Psi'' + \psi''\Psi + \psi''' = 0, \tag{5.18}$$

where we have rescaled $\tilde{\sigma} = \sigma/cR_m$. Boundary conditions are

$$(1 - 2\Psi' - \tilde{\sigma})\psi' + \psi\Psi'' + \psi''\Psi = 0 \qquad (\eta = 0) \tag{5.19a}$$

$$\Omega\psi'' + \psi(1 - \Psi') - \psi'\Psi = 0 \qquad (\eta = 0) \tag{5.19b}$$

$$\psi' \to 0 \qquad (\eta \to \infty) \tag{5.19c}$$

By solving these equations numerically, we found that both oscillatory and exponential base states are subject to structural instabilities. Other homogenous equations with a parameter have a discrete spectrum of eigenfunctions and associated eigenvalues. However, for this problem, there is a continuous spectrum of eigenfunctions. Indeed, there is an eigenfunction associated with any eigenvalue (growth rate) $\tilde{\sigma} < 1$ for each base state. The instabilities, especially for the oscillatory base states, have a very long range in the x-direction and appear to be driven by the unstable density field in the far-field, and are therefore a consequence of considering an isolated chimney in an infinite mushy layer. Figure 5.3 shows that both kinds of base state are susceptible to instability. These boundary-layer solutions are all unstable to the particular structural perturbations we considered, and they may be even more unstable to perturbations with a more general vertical structure.

5.2.4 Conclusions

This boundary-layer analysis attractively draws out the connection between a linear far-field temperature and a straight-sided chimney, which is an important observation given that this is a widely observed feature of chimneys in laboratory experiments (see figure 4.3). Thus we can conclude that the straight-sided chimneys in the CAP model are a consequence of imposing a vertically linear temperature in the passive region. In the boundary-layer analysis, we can also find the shape of the chimney with other power laws for the far-field temperature. Figure 5.4 shows the case $b = 1/2$ for example, and illustrates the fact that the chimney is typically almost straight-sided except near its base for a variety of realistic temperature profiles, which is qualitatively similar to the shape found in the numerical solutions of Chung & Worster (2002).

However, considering an isolated chimney in an infinite mushy layer introduces a number of artefacts. The infinite horizontal extent means that the boundary-layer equations possess an infinite family of solutions, all of which are unstable. The CAP model uses a finite passive region to determine the solution completely. It also seems likely that the finite domain also stabilizes the solutions. Some evidence for this claim comes from the structural similarity between the CAP

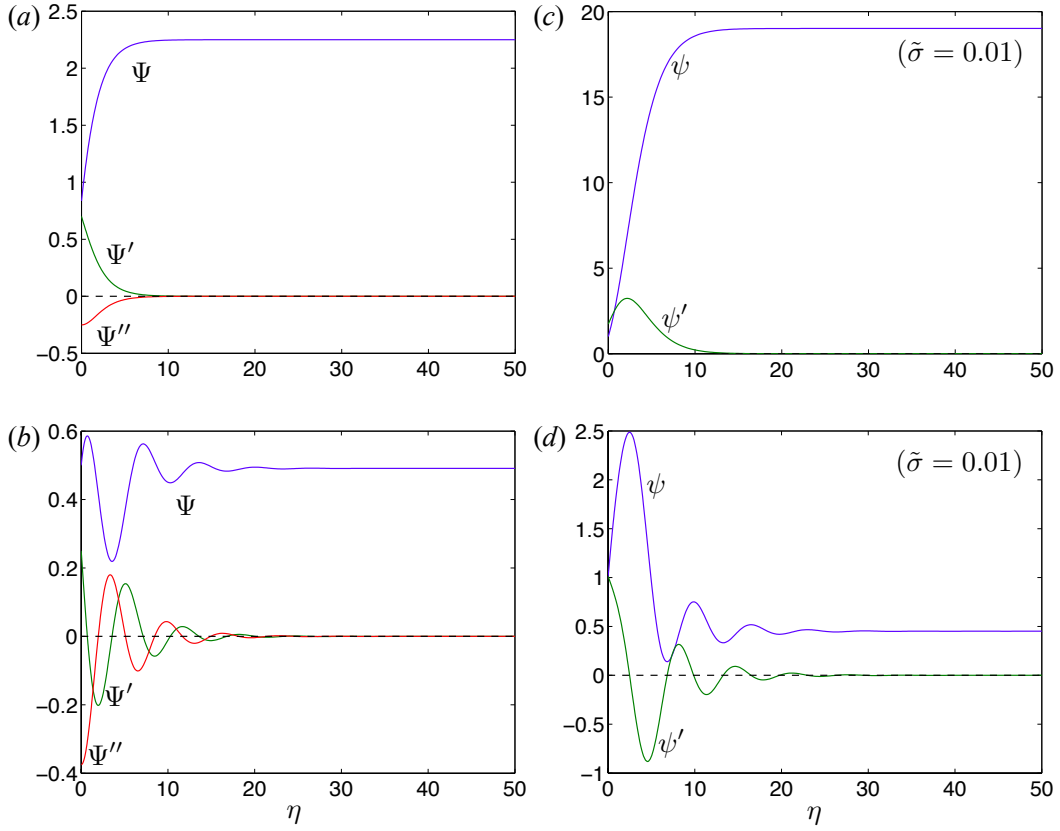

Figure 5.3: The perturbations with growth rate $\tilde{\sigma} = 0.01$ (c, d) of the boundary-layer solutions (a, b) at $\Omega = 1$. Note that the instability occurs for both monotonic (a, c) and oscillatory (b, d) base states, and also occurs for all Ω.

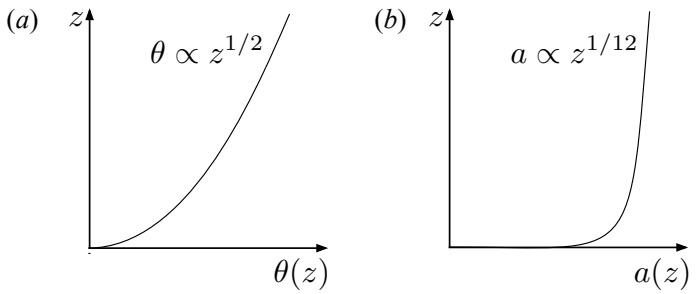

Figure 5.4: A nonlinear far-field temperature $b = 1/2$ profile (a) gives rise to the chimney width shown in (b). The sides remain very steep apart from near the base. Their shape is qualitatively similar to the numerical results of Chung & Worster (2002).

model and the stable numerical results of Chung & Worster (2002), as discussed in figure 4.5.

Furthermore, the continuous set of both oscillatory and monotonic boundary-layer solutions is somewhat surprising given that the similar problem of a heated wall with power-law temperature profile in a semi-infinite porous medium has a unique monotonic solution, see Cheng & Minkowycz (1977) (their figure 2 with $\lambda = 1$ corresponds to a chimney with linearly increasing temperature) and the wider review of Nield & Bejan (2006). This appears to be connected with the unstable density in the far-field. We return to this issue in section 5.4.3 below, where we show the critical monotonic solution that divides monotonic from oscillatory solutions in figure 5.10.

Therefore, by considering an active region around an isolated chimney, we have demonstrated the need to consider an appropriately bounded active region (or boundary layer) in a complete description of convection in a mushy layer.

5.3 The active region boundary-value problem

For the remainder of the chapter, we show that the CAP model needs an active region by considering the boundary-value problem associated with it. We firstly restate the boundary-value problem in the planar geometry (section 5.3.1) and discuss the existence and uniqueness of solutions (section 5.3.2). The function $G(\delta, \Omega)$ (section 4.3.3) relates the width of the active region δ to the spacing between chimneys L. We determine the asymptotic behaviour of G in various limits (section 5.4) and reach the important conclusion that the active region must have a finite width in order to sustain convection. In section 5.5, we consider the limit $\Omega \gg 1$ and prove the existence and uniqueness of a chimney spacing that maximizes the solute flux. We also prove the asymptotic dependence on Ω observed in the previous chapter.

5.3.1 Statement of problem

The solution for the active region (section 4.3.2) is governed by a fourth-order system of ordinary differential equations, subject to four boundary conditions, on

the domain $[0, \delta]$. The governing equations are

$$\Theta'' = -\Psi\Theta' + \Psi'\Theta, \qquad \Psi'' = -\Theta', \tag{5.20a, b}$$

and the boundary conditions are

$$\Psi'_0\Theta_0 = \Psi_0\Theta'_0, \qquad \Theta'_0 = \Psi_0\Theta_0/\Omega, \qquad \Theta_\delta = 1, \qquad \Theta'_\delta = 0 \tag{5.21a, b, c, d}$$

where subscripts 0 and δ denote quantities evaluated at $\eta = 0$ and $\eta = \delta$ respectively. The last two conditions are particular to the finite domain and correspond physically to continuity of temperature and heat flux at the interface between passive and active regions.

The width of the active region δ is determined as part of the solution both in the case of fixed chimney half-spacing L, and in the case in which L takes the value that maximizes the solute flux (the maximum-flux criterion introduced in section 4.5).

Firstly, in the case of imposing the chimney spacing, the size of the active region δ is determined through equation (4.23)

$$G(\delta, \Omega) = LR_m\theta_\infty^{1/2}, \tag{5.22}$$

where

$$G(\delta, \Omega) = \Omega^{-1/2}(-\Psi'_\delta)^{-1/2}\left(\delta - \Psi_\delta/\Psi'_\delta\right), \tag{5.23}$$

which we can evaluate having solved the boundary-value problem (5.20, 5.21).

Secondly, in the case of imposing the maximum-flux criterion, we look for turning points which correspond to flux-maximising chimney spacings,

$$\frac{\partial\gamma}{\partial\delta} = 0, \tag{5.24}$$

where γ is proportional to the solute flux through the chimney by equation (4.26)

$$F_{\text{Solute}} = -R_m\gamma(\delta, \Omega). \tag{5.25}$$

and satisfies

$$\gamma(\delta, \Omega) = \frac{1}{2}\frac{\Psi_0}{\Theta_0}\left(\delta - \Psi_\delta/\Psi'_\delta\right)^{-1}. \tag{5.26}$$

5.3.2 Existence and uniqueness of solutions

We first investigate the existence and uniqueness of solutions to the boundary-value problem as follows. Given Ψ_0 and Θ_0, we can combine $(5.21a, b)$ to find Ψ'_0 and Θ'_0. Thus we have an initial-value problem that we can solve on any domain $[0, \delta]$, assuming the solution does not have a singularity at a finite value of η. In this section, we restrict attention to $\Psi_0 > 0$ (which corresponds to flow into a chimney) and Θ_0 in the range $[0, 1]$ (which ensures that the depth of the mushy layer increases near the chimney). However, the initial-value problem is well posed for a wider class of initial conditions.

A solution of the full boundary-value problem must satisfy the remaining boundary conditions $(5.21c, d)$. Therefore, we solve the initial-value problem introduced above to a high accuracy using the MATLAB 'ode113' routine, with relative and absolute error tolerances of 1×10^{-12} and 1×10^{-15} respectively. Then we use the MATLAB 'isosurfaces' routine to plot surfaces $\Theta_\delta = 1$, $\Theta'_\delta = 0$ (the required boundary conditions) as functions of Ψ_0, Θ_0 and δ. An example of this is shown in figure 5.5, and the solutions are the intersection curves highlighted. An alternative representation of these solutions can be obtained by taking slices through figure 5.5 at fixed values of δ. This corresponds to making contour plots, as shown in figure 5.6, and the solutions are the intersections of the contours $\Theta_\delta = 1$ and $\Theta'_\delta = 0$.

The solution branches can be categorized by the number of turning points of Ψ. The first branch (counting from the right of figure 5.5, that is going from low to high δ) has one turning point and each subsequent branch has an additional turning point. This feature corresponds to the fact that $\Psi' = 0 \Leftrightarrow \Theta'' = 0$ (from equation $5.20a$). Physically, the number of turning points corresponds to the number of convecting cells within the active region. We have continued to higher values of δ and this pattern continues.

The first branch has a negative value of Ψ'_δ and thereafter the sign of Ψ'_δ alternates. Thus the 'even' branches correspond to flow from the active to the

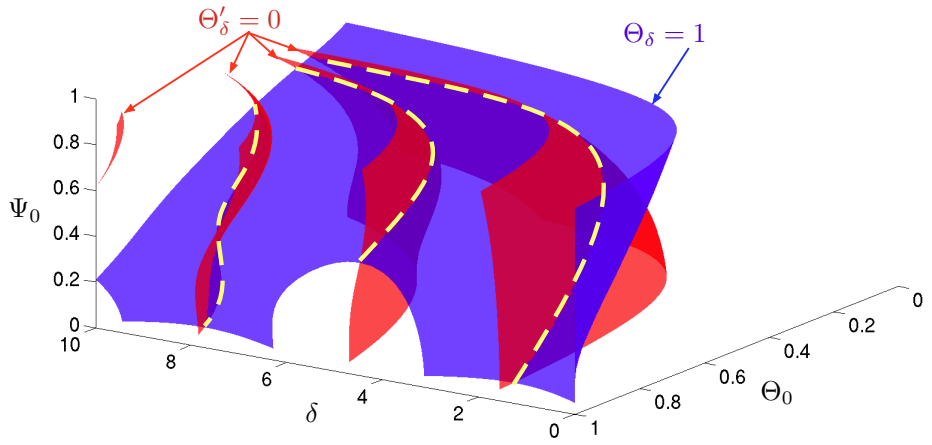

Figure 5.5: Surfaces $\Theta_\delta = 1$ and $\Theta'_\delta = 0$ calculated in the case $\Omega = 1$. The intersection curves, highlighted with dashed yellow lines, correspond to branches of solutions.

passive region, and therefore correspond to flow that is from the mushy layer into the liquid melt in the passive region. This is inconsistent with the boundary conditions at the mush–liquid interface (equation 4.12) and so is not a valid solution of the entire CAP model. Thus $G(\delta, \Omega)$ is defined in (5.23) only for $\Psi'_\delta < 0$. The other 'odd' branches (the third, fifth, and so on) are in principle permissible. However, they are not consistent with the overall CAP model in that the downwelling in the passive region was assumed to set the vertical velocity scale away from the chimney. Furthermore, these higher branches correspond to substantially lower-flux solutions of the full problem (as proved in the case $\Omega \gg 1$ in section 5.5 below). Therefore, motivated by the maximum-flux criterion in section 4.5 of the previous chapter, we restrict attention to the first branch.

The first branch of solutions starts at $\Psi_0 = 0$, $\Theta_0 = 1$, $\delta = \pi/2$, and there are no solutions below $\delta = \pi/2$. This interesting cut-off at $\delta = \pi/2$ occurs because the solutions are damped, nonlinear waves of frequency ω that is approximately equal to the average value of $\Theta^{1/2}$. But $\Theta < 1$, so $\omega < 1$. The first branch corresponds to $\omega\delta = \pi/2$ (one quarter wavelength), so $\delta > \pi/2$. This argument will be formalized in an asymptotic approximation below (section 5.4.2).

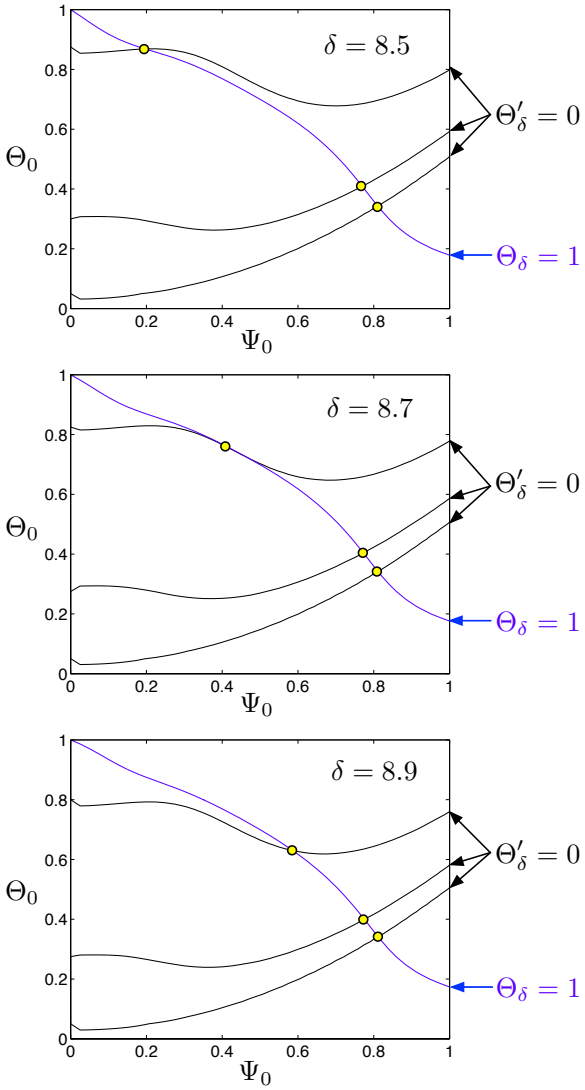

Figure 5.6: Contour plots at three values of δ at fixed $\Omega = 1$. At these values of δ, there are three intersection points, highlighted with yellow circles, corresponding to the three branches in figure 5.5. Note that the third branch changes rapidly as a function of δ near $\delta = 8.7$, which corresponds to the contours lying approximately tangentially.

5.4 Asymptotic behaviour of $G(\delta, \Omega)$

5.4.1 Introduction

In this section, we investigate the function $G(\delta, \Omega)$, which is proportional to the chimney spacing, in order to gain insight into the relationship between solute flux and chimney spacing. We consider two asymptotic limits for the width of the active region δ. We consider firstly the case δ is just above the lower cut-off at $\pi/2$, and secondly the behaviour at high values of δ. These limits can be considered in the context of fixed chimney spacing, which corresponds to imposing the value of $G(\delta, \Omega)$. Note that the asymptotic limits considered in this section do not correspond to the maximum solute flux.

5.4.2 Solution for $\delta = \pi/2 + \epsilon$ where $\epsilon \ll 1$

There is an exact trivial solution of the boundary-value problem (5.20, 5.21) for all values of δ (namely $\Theta \equiv 1$, $\Psi \equiv 0$), although G is not well defined for this trivial solution, which corresponds to a stagnant mushy layer.

For $\delta > \pi/2$ there is a non-trivial solution. We compute its behaviour asymptotically at $\delta = \pi/2 + \epsilon$, where $\epsilon \ll 1$, by finding an expansion of the solution in powers of ϵ. Let

$$\Theta = 1 + \epsilon g_1 + \epsilon^2 g_2 + O(\epsilon^3), \tag{5.27}$$

$$\Psi = 0 + \epsilon f_1 + \epsilon^2 f_2 + O(\epsilon^3). \tag{5.28}$$

We substitute these equations into the governing equations and boundary conditions and collect terms in powers of ϵ.

At $O(\epsilon)$, from (5.20) the differential equations are

$$g_1'' = f_1', \qquad f_1'' = -g_1', \tag{5.29a, b}$$

and from (5.21) the boundary conditions are

$$f_1' = 0, \quad \Omega g_1' = f_1 \quad (\eta = 0), \qquad g_1 = 0, \quad g_1' = 0 \quad (\eta = \pi/2), \quad (5.30a, b, c, d)$$

where, for example, we have used

$$1 = \Theta(\delta) = \Theta(\pi/2 + \epsilon) = \Theta(\pi/2) + \epsilon\Theta'(\pi/2) + \frac{\epsilon^2}{2}\Theta''(\pi/2) + O(\epsilon^3)$$
$$= \left[1 + \epsilon g_1 + \epsilon^2 g_2 + \epsilon(\epsilon g_1') + O(\epsilon^3)\right]_{\eta=\pi/2}$$

to obtain equation (5.30c, d).

At $O(\epsilon^2)$, from (5.20) the differential equations are

$$g_2'' = -f_1 g_1' + f_1' g_1 + f_2', \qquad f_2'' = -g_2', \tag{5.31a, b}$$

and from (5.21) the boundary conditions are

$$f_2' + f_1' g_1 - f_1 g_1' = 0, \quad \Omega g_2' = f_1 g_1 + f_2 \quad (\eta = 0),$$
$$g_2 + g_1' = 0, \quad g_2' + g_1'' = 0 \quad (\eta = \pi/2). \tag{5.32a, b, c, d}$$

The first-order equations are those of an unforced harmonic oscillator of frequency 1, which, to leading order, is the average value of $\Theta^{1/2}$, as discussed in section 5.3.2. We combine (5.29a, b) and solve subject to boundary conditions (5.30) – one of which is redundant because of the nature of the coupling – to find

$$f_1 = A(\Omega - 1 + \cos\eta), \tag{5.33}$$
$$g_1 = -A(1 - \sin\eta), \tag{5.34}$$

where A is an unknown constant that must be determined by solving the second-order problem.

The second-order equations have the character of an oscillator of frequency 1 that is resonantly forced by the first-order solution. This is evident upon eliminating g_2 between (5.31a, b) and substituting equations (5.33, 5.34) to obtain

$$f_2''' + f_2' = A^2[1 + (\Omega - 1)\cos\eta - \sin\eta]. \tag{5.35}$$

We solve $(5.31a, b)$ subject to $(5.32a, b, c)$ to obtain

$$f_2 = -B\cos\eta + \frac{A^2}{2}\left[(\Omega-1)(3\sin\eta - \eta\cos\eta) + \cos\eta + \eta\sin\eta + 2\eta\right] + C, \tag{5.36}$$

$$g_2 = -f_2' + D, \tag{5.37}$$

where

$$C = (\Omega-1)(-B + A^2/2) \qquad D = B + A^2\left[\pi(\Omega-1)/4 + 1\right],$$

and B is another constant that could, in principle, be determined by proceeding to the next order. Finally, we apply $(5.30d)$ to find that

$$A^2\left[\frac{1}{2}(\Omega-1) + \frac{\pi}{4}\right] - A = 0,$$

so either $A = 0$, in which case the leading-order solution is trivial, or

$$A = \left[\frac{1}{2}(\Omega-1) + \frac{\pi}{4}\right]^{-1}. \tag{5.38}$$

Therefore, having fully determined the asymptotic solution to first order, we obtain

$$\begin{aligned} G(\delta,\Omega) &= 2\Omega^{-1/2}A^{-3/2}\epsilon^{-1/2} + O(\epsilon^{1/2}), \\ &= 2\Omega^{-1/2}\left[\frac{1}{2}(\Omega-1) + \frac{\pi}{4}\right]^{3/2}\epsilon^{-1/2} + O(\epsilon^{1/2}). \end{aligned} \tag{5.39}$$

In the special case $\Omega = 1$, this simplifies to

$$G(\delta, 1) = \frac{\pi^{3/2}}{4}\epsilon^{-1/2} + O(\epsilon^{1/2}). \tag{5.40}$$

Furthermore, we find the asymptotic behaviour of $\gamma(\delta, \Omega)$:

$$\gamma(\delta,\Omega) = \frac{1}{4}\Omega A^2\epsilon + O(\epsilon^2) = \frac{1}{4}\Omega\left[\frac{1}{2}(\Omega-1) + \frac{\pi}{4}\right]^{-2}\epsilon + O(\epsilon^2), \tag{5.41}$$

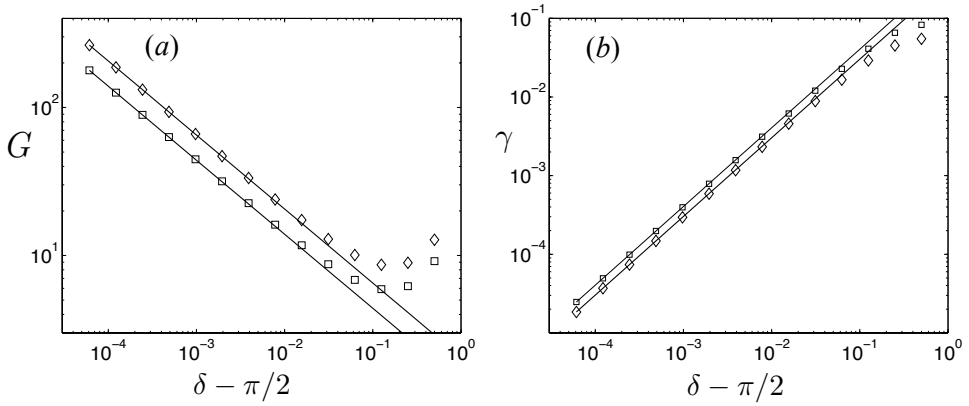

Figure 5.7: (a) is a log–log plot showing $G(\delta, \Omega)$ at $\Omega = 1$ (squares) and $\Omega = 2$ (diamonds). The asymptotic predictions (solid lines) from equation (5.39) match extremely well. Likewise (b) is a log–log plot showing $\gamma(\delta, \Omega)$ at the same values of Ω. Again, the asymptotic predictions (solid lines) from equation (5.41) match extremely well.

which simplifies in the case $\Omega = 1$ to

$$\gamma(\delta, 1) = 4\pi^{-2}\epsilon + O(\epsilon^2). \tag{5.42}$$

These predictions match numerical results extremely well, as shown in figure 5.7.

These values of δ correspond to the lower branch of the relationship between flux and Rayleigh number (see the dashed portion of the curves in figures 4.5 and 4.6 in the previous chapter), so we find that at fixed chimney spacing L, F_{Solute} varies with the inverse square of L. In particular, since $F_{\text{Solute}} = -R_m\gamma(\delta, \Omega)$ and $L = R_m^{-1}\theta_\infty^{-1/2}G(\delta, \Omega)$, we find

$$F_{\text{Solute}} = -\left[AR_m\theta_\infty\right]^{-1} L^{-2} = -\left[R_m\theta_\infty\right]^{-1}\left[\frac{1}{2}(\Omega - 1) + \frac{\pi}{4}\right] L^{-2}. \tag{5.43}$$

Perhaps most importantly, this section formalizes the argument that the minimum size of the active region required to sustain convection is $\delta = \pi/2$ (independently of Ω). This demonstrates the important physical insight that there must be a finitely wide active region, where baroclinic torque occurs, in order to drive convection through chimneys. It is not the case that the buoyancy causes motion in the chimney and then the rest of the mushy layer responds essentially

passively.

5.4.3 Solution for $\delta \gg 1$

Integrating equation (5.20b), we find

$$\Theta = -\Psi' + c, \tag{5.44}$$

where $c = \Theta_\delta + \Psi'_\delta = 1 + \Psi'_\delta$. We find numerically that $\Psi'_\delta \to 0$ exponentially, so for now we consider this as an ansatz. If this ansatz holds, then $c \to 1$ exponentially. Note that c is also equal to $\Theta_0 + \Psi'_0$, so with boundary conditions (5.21a, b)

$$\Theta_0 \sim 1 - \Psi_0^2/\Omega. \tag{5.45}$$

If we substitute equation (5.44) back into (5.20a), then we find

$$\Psi''' + \Psi\Psi'' + \Psi'(c - \Psi') = 0. \tag{5.46}$$

Consistently with the exponential decay of Ψ'_δ, this equation can be approximated at large η by

$$\Psi''' + \Psi_\delta\Psi'' + \Psi' = 0, \tag{5.47}$$

which we can solve by positing the solution $\Psi' = \mathrm{e}^{m\eta}$. This implies

$$m^2 + m\Psi_\delta + 1 = 0 \Rightarrow m = -\frac{\Psi_\delta}{2} \pm \mathrm{i}\sqrt{1 - \left(\frac{\Psi_\delta}{2}\right)^2}. \tag{5.48}$$

Let $\omega = \sqrt{1 - (\Psi_\delta/2)^2}$. Then

$$\Psi' = \mathrm{e}^{-\eta\Psi_\delta/2}(A\cos\omega\eta + B\sin\omega\eta). \tag{5.49}$$

From figure 5.5, we observe that the first branch has precisely one turning point $\Psi' = 0$. This is consistent with $\omega \to 0$, or equivalently $\Psi \to 2$ from below. Numerically, we observe that this is an algebraic process. Then equation (5.49) shows that our assumptions are self-consistent and $\Psi'_\delta \sim -\mathrm{e}^{-\delta+\delta_0}$, for some constant δ_0.

I have integrated the equations numerically to a high accuracy and find that the scalings postulated on the basis of analytical arguments hold very well. I find that Ψ_δ approaches 2 from below in an inversely quadratic fashion.

Indeed, the limit of large δ in the CAP model recovers the boundary-layer analysis in section 5.2.1. However, rather than the continuous set of monotonic and oscillatory solutions that we found in that case, each branch of solutions in the CAP model corresponds to an oscillatory solution and there are no monotonic solutions. Furthermore, while there is still a (discrete) family of solutions at any fixed value of δ, as we let $\delta \to \infty$ along any branch, the solutions all approach the critical (marginal) monotonic solution identified in section 5.2.2, as shown in figure 5.8. Thus, $\Psi_\delta \to 2^-$ corresponds to the critical $\Psi_\infty = 2$ (given that $b = 1$ in the CAP model). Therefore, the mass flux Ψ_δ is bounded above in the CAP model (whereas the monotonic boundary-layer solutions had an unbounded Ψ_∞). We find $\Psi_C(0) = 0.8216$, $\Psi'_C(0) = 0.6750$ and $\Theta_C(0) = 0.3250$ when $\Omega = 1$. Figure 5.9 shows our numerical results.

Returning to the multiplicity of solutions in the boundary-layer analysis, the CAP model has the attractive feature of selecting the critical monotonic solution of the boundary-layer equations that separates the region of oscillatory solutions from that of monotonic solutions. We show this critical solution in figure 5.10. It has a similar structure to the boundary-layer solution for a heated plate in a semi-infinite porous medium (Cheng & Minkowycz, 1977), with some minor differences associated with the different boundary conditions at a chimney.

5.4.4 Solute fluxes for $\delta \gg 1$

We now fix Ω and use '$\sim$' to include a proportionality constant that depends on Ω. Asymptotically as $\delta \to \infty$

$$G(\delta) \sim \mathrm{e}^{3\delta/2}, \tag{5.50}$$

$$\gamma(\delta) \sim \mathrm{e}^{-\delta}. \tag{5.51}$$

High values of δ correspond to the upper branch of the relationship between flux and Rayleigh number (see the solid curves in figures 4.6 and 4.7 in the previous

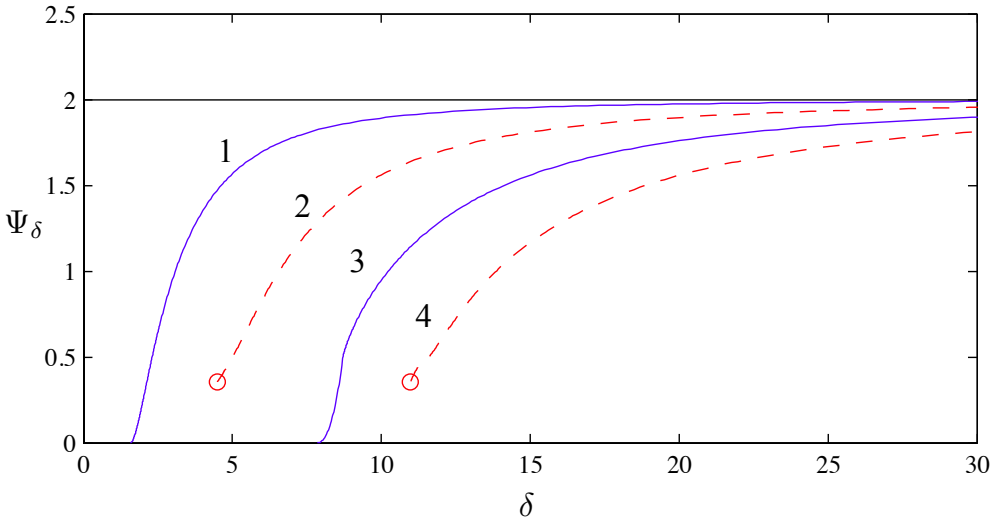

Figure 5.8: The strength of the horizontal flow Ψ_δ on the first four branches of solutions. The solid blue curves correspond to the odd branches (that have an odd number of turning points of the vertical velocity, see section 5.3.2) and the dashed curves correspond to the even branches. The open circles denote a cut-off where $\Theta_0 = 1$, although it is possible to extend the branches slightly if the condition $\Theta_0 \leq 1$ is relaxed. Note that all the branches tend to the critical $\Psi_\infty = 2$, although there are more branches (not shown) at any finite δ. Throughout $\Omega = 1$.

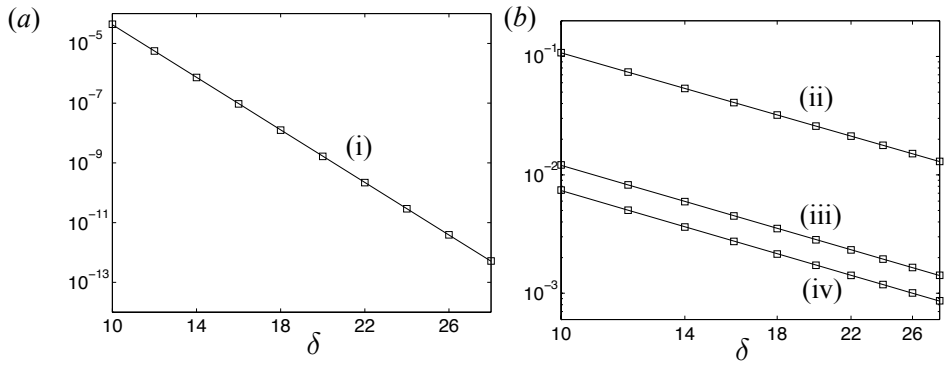

Figure 5.9: (a) is a log–linear plot showing (i) the exponential decay of $-\Psi'_\delta$. The best-fit line is $\Psi'_\delta = -\exp(-1.013\delta + 0.05746)$. (b) is a log–log plot showing the algebraic behaviour of (ii) $2 - \Psi_\delta$, (iii) $(\Psi_0)_c - \Psi_0$ and (iv) $\Theta_0 - (\Theta_0)_c$. The best-fit lines are (ii) $\Psi_\delta = 2 - 12.11 \times \delta^{-2.053}$, (iii) $\Theta_0 = (\Theta_0)_c + 1.453 \times \delta^{-2.082}$ and (iv) $\Psi_0 = (\Psi_0)_c - 0.9013 \times \delta^{-2.088}$. Throughout $\Omega = 1$.

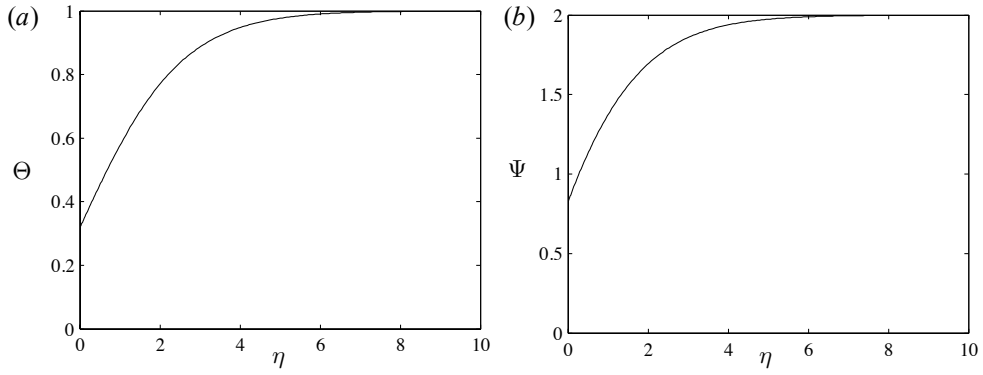

Figure 5.10: The critical solution of the active-region problem for large δ. (a) temperature Θ, related to the vertical velocity by $\Psi' = 1 - \Theta$. (b) horizontal velocity Ψ, which tends to 2. Throughout $\Omega = 1$.

chapter). Now $L = R_m^{-1}\theta_\infty^{-1/2}G(\delta, \Omega)$ so at fixed L, high values of R_m correspond to high values of δ. So $R_m \gg 1$ corresponds to $\delta \gg 1$ and so at high Rayleigh number

$$L \sim R_m^{-1}\theta_\infty^{-1/2}\mathrm{e}^{3\delta/2}, \tag{5.52}$$

which implies that

$$F_{\text{Solute}} \sim -R_m^{1/3}\theta_\infty^{-1/3}L^{-2/3}, \tag{5.53}$$

since $F_{\text{Solute}} = -R_m\gamma(\delta, \Omega) \sim -R_m\mathrm{e}^{-\delta}$. Therefore, at fixed chimney spacing, flux scales with the cube root of Rayleigh number, and at fixed Rayleigh number, flux scales with chimney spacing to $-2/3$ power. Therefore, at large chimney spacing, the solute flux decreases with $L^{-2/3}$. To our knowledge, this result has not been observed before, which may be because having one convecting cell in a large region between two chimneys is unstable to the formation of new convecting cells and new chimneys (see previous section).

These asymptotic limits of large and small δ elucidate a number of important features of the CAP model. However, numerical calculations of G for intermediate values of δ (figures 4.7 and 5.11) additionally show that there is a global minimum value of G, corresponding to the minimum spacing between chimneys, and that γ is a bounded, positive function on $\pi/2 < \delta < \infty$. Let δ_m be defined by $\partial G/\partial\delta(\delta_m, \Omega) = 0$, and let $G_{\text{min.}}$ be the minimum value of G, as marked in figure

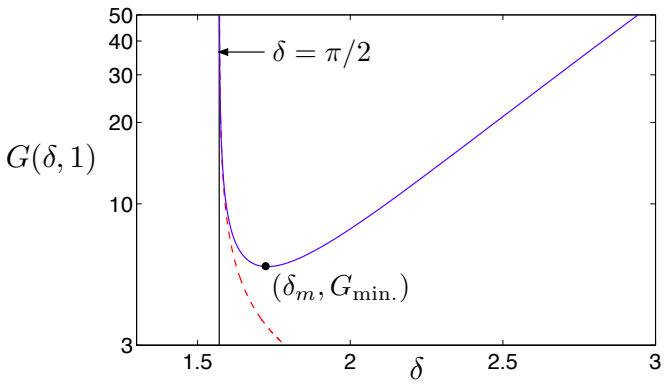

Figure 5.11: Adaptation of figure 4.7*a* from the previous chapter, showing $G(\delta, \Omega = 1)$, which is proportional to the chimney spacing. The global minimum corresponds to the minimum chimney spacing required to sustain convection. The asymptotic results derived in this chapter for $\delta \to \pi/2$ (dashed red curve) follow the numerical results (solid blue curve) very well. However, the $\delta \gg 1$ results (not shown) only apply for much higher values of δ (see figure 5.9). The quantities δ_m and $G_{\text{min.}}$ discussed in the main text are labelled.

5.11. Then the minimum chimney spacing is

$$L_{\text{min.}} = R_m^{-1} \theta_\infty^{-1/2} G_{\text{min.}}(\Omega). \tag{5.54}$$

Combined with our asymptotic observations, this shows that there is maximum solute flux on $\delta_m < \delta < \infty$. We prove the uniqueness of the maximum in section 5.5 for the case $\Omega \gg 1$, but numerically we find that this holds in general (*cf.* figure 4.7*b*).

5.5 Asymptotic solution in the limit $\Omega \to \infty$

5.5.1 Leading-order solution

In the limit $\Omega \to \infty$, corresponding physically to large latent heat release, we can solve the leading-order problem analytically. Thus we prove that there is a unique chimney spacing that maximizes the solute flux.

At large values of Ω, the solution of the governing equations (5.20) is a weak

departure from the exact solution of no flow, discussed in section 5.4.2. Considering the boundary conditions (5.21a, b) at ($\eta = 0$) leads us to posit a regular expansion

$$\Psi = \Psi_0 + \frac{1}{\Omega} f(\eta) + O(\Omega^{-2}), \tag{5.55}$$

$$\Theta = 1 - \frac{1}{\Omega} g(\eta) + O(\Omega^{-2}). \tag{5.56}$$

We substitute into the differential equations (5.20) and find that

$$g'' + \Psi_0 g' + f' = 0, \qquad f'' = g'. \tag{5.57a, b}$$

The boundary conditions (5.21) imply that

$$f = 0, \quad f' = \Psi_0^2, \quad g' = -\Psi_0 \quad (\eta = 0), \qquad g = 0, \quad g' = 0 \quad (\eta = \delta), \tag{5.58$a - e$}$$

Integrating equation (5.57b), we obtain

$$f' = g - C, \tag{5.59}$$

where C is a constant, and substituting this into equation (5.57a), we obtain

$$g'' + \Psi_0 g' + g = C. \tag{5.60}$$

This has general solution

$$g = \left[A \sin\left(\eta \sqrt{1 - \Psi_0^2/4} \right) + B \cos\left(\eta \sqrt{1 - \Psi_0^2/4} \right) \right] e^{-\Psi_0 \eta/2} + C. \tag{5.61}$$

The boundary condition (5.58b) with equation (5.59) shows that

$$B = \Psi_0^2, \tag{5.62}$$

and then boundary condition (5.58c) shows that

$$A = \left(\frac{\Psi_0^2}{2} - 1 \right) \frac{\Psi_0}{\sqrt{1 - \Psi_0^2/4}}. \tag{5.63}$$

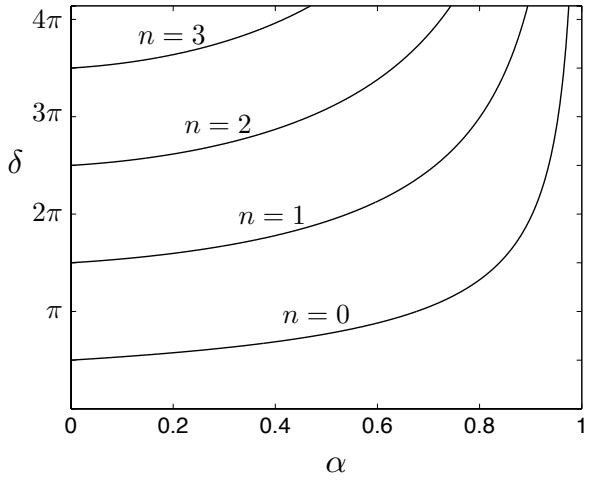

Figure 5.12: Plot of solution curves for equation (5.64) for the first four branches. Note that there are no solutions for $\delta < \pi/2$ as we found previously.

Boundary condition (5.58e) then determines the unknown Ψ_0, which is expressed implicitly by

$$\delta(\alpha) = \frac{\arcsin\alpha + \pi(1+2n)/2}{(1-\alpha^2)^{1/2}}, \tag{5.64}$$

where $\alpha = \Psi_0/2$, n is an integer and arcsin takes its principal value. These multiple solutions, shown in figure 5.12, correspond to the multiple solutions discussed previously. We restrict attention to $\alpha \geq 0$ (such that flow is from the mush into the chimney). Furthermore, there are no solutions if $\alpha \geq 1$, so we need consider only $0 \leq \alpha < 1$.

Finally, C can then be determined from boundary condition (5.58d) to be

$$C = (-1)^n\, 2\alpha \exp(-\alpha\delta). \tag{5.65}$$

However, recognising that $\Psi'_\delta = f'(\delta)/\Omega = -C/\Omega$, we can restrict attention to the case n even, thereby ensuring that $\Psi'_\delta < 0$, as discussed previously in section 5.3.2. Then equation (5.26) implies that

$$\gamma(\delta, \Omega) = C/2\Omega, \tag{5.66}$$

so, under the maximum-flux principle, we maximize $C(\delta)$, plotted in figure 5.13b,

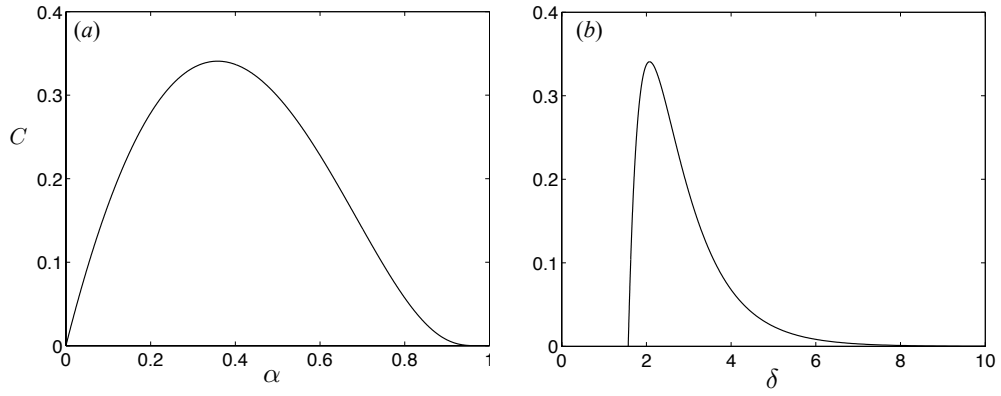

Figure 5.13: The existence of a unique maximum flux, illustrated for the case $n = 0$, which is the overall maximum-flux case. C can be interpreted as a function of α, as in (a), or δ, as in (b).

in order to determine the solute flux, which is proportional to γ.

5.5.2 Maximum-flux criterion

As discussed above, we can restrict attention to the domain $0 \leq \alpha < 1$, and since $\delta = \delta(\alpha)$ on each branch (as specified by equation 5.64), we can also consider C as a function of α (figure 5.13a). Now

$$\frac{dC}{d\delta} = \left(\frac{d\delta}{d\alpha}\right)^{-1} \frac{dC}{d\alpha} = \frac{1}{\delta'} \left(1 - \alpha(\alpha\delta)'\right) 2\exp(-\alpha\delta). \tag{5.67}$$

But

$$\delta'(\alpha) = \frac{1}{1-\alpha^2} + \alpha \frac{\arcsin\alpha + \pi(1+2n)/2}{(1-\alpha^2)^{3/2}} > 0, \tag{5.68}$$

which, by substituting (5.68) into (5.67), shows that $dC/d\delta = 0$ if and only if

$$1 - 2\alpha^2 = \frac{\alpha}{(1-\alpha^2)^{1/2}} \left[\arcsin\alpha + \frac{\pi(1+2n)}{2}\right]. \tag{5.69}$$

Now the left-hand side decreases monotonically from 1 to -1 and the right-hand side increases monotonically from 0 to $+\infty$, so by the Intermediate-Value Theorem, there is a unique solution, $\alpha = \alpha_c$, to equation (5.69). Further, the

positive function $C(\alpha)$ satisfies $C(0) = C(1) = 0$, so this turning point must be a maximum. Having solved equation (5.69) numerically to find α_c, we determine

$$\delta_c = \delta(\alpha_c) = 1/\alpha_c - 2\alpha_c, \tag{5.70}$$

$$C_c = C(\alpha_c) = 2\alpha_c \exp(-1 + 2\alpha_c^2). \tag{5.71}$$

Therefore, we have proved the existence of a unique maximum flux on each branch of solutions. Furthermore, the overall maximum occurs when $n = 0$, which we prove as follows. Define

$$h(\alpha) = (1/\alpha - 2)(1 - \alpha^2)^{1/2} - \arcsin(\alpha), \tag{5.72}$$

which implies that

$$h'(\alpha) = -(4 + 1/\alpha^2)(1 - \alpha^2)^{1/2} < 0. \tag{5.73}$$

But $h(\alpha)$, which decreases from $+\infty$ to $-\pi/2$ over $[0, 1)$, satisfies

$$h(\alpha_c) = \pi(1 + 2n)/2, \tag{5.74}$$

and so as n increases, α_c decreases. Then $C_c = 2\alpha_c \exp(-1 + 2\alpha_c^2)$ must also decrease with n. Therefore, solutions with a greater number of convecting cells have a lower associated solute flux, and the maximum-flux criterion leads us to consider solutions which have only one convecting cell.

In the case $n = 0$, we find $\alpha_c = 0.3582$, $\delta_c = 2.0749$, and $C_c = 0.3407$. This leads to the asymptotic prediction

$$\gamma_c(\Omega) \sim 0.1704\,\Omega^{-1} \tag{5.75}$$

for the proportionality constant in the relation $F_{\text{Solute}} = -R_m\gamma_c(\Omega)$, as is confirmed by the numerical calculations presented in the previous chapter (see figure 4.8*a*).

This asymptotic limit proves the uniqueness of the flux-maximising chimney spacing in the limit $\Omega \gg 1$. However, this result actually holds for all Ω. Indeed,

this asymptotic calculation captures a number of features relevant to all values of Ω. In particular, figure 5.12 is structurally the same as a projection of the dashed curves in figure 5.6, which is the case $\Omega = 1$. Furthermore, a graph of $\gamma(\delta, \Omega)$ along the first branch of solutions in figure 5.6 corresponds to figure 5.13. Thus this asymptotic proof provides valuable corroboration of our numerical observation that there is always a unique value of δ, and hence of L such that the solute flux is maximized, and that we need only consider solutions with one convecting cell.

5.6 Conclusions

The CAP model is a simple, semi-analytical description of convection in a mushy layer. By mathematically analysing its structure we are able to demonstrate important features of convection in a mushy layer. Firstly, we have shown that the boundary-layer solutions to the mushy-layer equations near an isolated chimney are unstable. The nonlinear development of this instability would likely cause the formation of new chimneys. Therefore, it is important to consider a full convecting cell, with both upwelling in (and near) the chimney, and downwelling in the bulk of the mushy layer away from the chimney. In the CAP model, we consider this latter region to be passive. Furthermore, the boundary-layer solutions are an infinite family of both monotonic and oscillatory solutions. Our analysis of the CAP model shows that the oscillatory solutions all tend to the critical monotonic solution identified in the boundary-layer analysis that separates the region where there are oscillatory solutions from that where there are monotonic solutions. Thus we can recover a unique solution of a kind similar to that found for the case of a heated plate in a semi-infinite porous medium.

Secondly, we have shown that there is a minimum width of the active region required to sustain convection within a mushy layer. This width is physically determined by the need to have a turning point in the vertical velocity within the active region, from upwards near the chimney, to downwards away from it. This important general feature arises because of the marginal equilibrium condition, as we showed in the corner flow problem in section 3.5. Thus the structure of the active region in the CAP model is an essential aspect of any reduced description of convection in a mushy layer.

Chapter 6

Gravity Drainage in Sea Ice

*The content of this chapter has been published in the Geophysical Research Letters (Rees Jones & Worster, 2013*b*).*

6.1 Introduction

The polar seasonal cycle sees an enormous volume of sea ice frozen each year. As leads (which are areas of open water between ice floes) open up and refreeze, and as pack ice thickens over the winter, brine is initially held within a matrix of porous sea ice. A number of different mechanisms lead to the subsequent desalination of sea ice observed over time in field measurements (Nakawo & Sinha, 1981; Eicken, 1992).

Untersteiner (1968) reviewed and estimated the strength of the mechanisms of brine-pocket migration, brine expulsion and flushing, which we discuss in section 6.2, as well as gravity drainage. In this chapter we focus on gravity drainage (Eide & Martin, 1975; Cox & Weeks, 1975), which is the dominant process causing desalination while ice grows during the winter.

Gravity drainage occurs when the interstitial brine becomes increasingly concentrated in salt, which is segregated from the solid phase as the ice continues to freeze. The increasingly dense brine can then drain from the ice under the action of gravity, reducing the salinity of the ice and causing plumes of dense brine to sink into the polar oceans, deepening the mixed layer and increasing the potential

for bottom-water formation and vertical mixing.

However, while the significance of gravity drainage to brine fluxes from sea ice during its winter growth has long been acknowledged (Untersteiner, 1968; Niedrauer & Martin, 1979; Notz & Worster, 2009), it has proved difficult to incorporate this process directly in the sea-ice component of Global Climate Models in a sufficiently simple fashion (Hunke *et al.*, 2011). Indeed, even the most resolved, established sea-ice models (such as version 4 of CICE: the Los Alamos sea ice model, Hunke & Lipscomb, 2008) prescribe the bulk salinity of the ice, use it to calculate its thermal properties and then calculate the thermodynamic growth of the ice (Maykut & Untersteiner, 1971; Bitz & Lipscomb, 1999). Although this approach is a reasonable starting point, determining the bulk salinity dynamically would constitute a major advance and would increase confidence in the predictions of Global Climate Models in significantly changed climatic conditions in which the proportion of first-year ice might be much higher and the previously prescribed salinity profiles, which are more appropriate to multi-year ice, might consequently be less appropriate. We develop such a one-dimensional dynamic-salinity sea-ice model in chapter 7.

Some recent theoretical studies approach this challenge by treating sea ice as a two-phase reactive porous medium and numerically solving partial differential equations in two dimensions for heat, salt and mass conservation, using Darcy's law for the interstitial fluid flow. Oertling & Watts (2004) and Wells *et al.* (2011) constitute important, contrasting studies in this vein.

In this chapter, we apply the CAP model of convective desalination from chapter 4 to describe and determine mathematically the essential physics of gravity drainage, elucidating the connection between downward flow in brine channels and a convective upward flow in the rest of the porous ice. We develop a simple theoretical parameterization of gravity drainage in sea ice by calculating the strength of the interstitial upwelling away from the main channels required to replace the interstitial liquid that flows into the brine channels and thence into the ocean. We then use our results to interpret the previous laboratory experiments of Eide & Martin (1975) concerning dye-front propagation in sea ice and an analogous experiment of Chen (1995), which provide a consistency check for our model.

6.2 Mechanisms of desalination

Gravity drainage is only one of a number of processes that cause the salinity of sea ice to decrease over time. We now review these in the context of growing first-year ice during the polar winter.

Firstly, brine-pocket migration (Whitman, 1926) is driven by the temperature gradient within sea ice, hence its alternative name in materials science, 'temperature gradient zone melting' (*e.g.* Tiller, 1963). The vertical temperature gradient in winter from cold at the ice–atmosphere interface to warm at the ice–ocean interface establishes an interstitial salinity gradient from salty to less salty within brine held in the pore space. This salinity gradient means that salt diffuses towards the ice–ocean interface. In the summer, when the temperature gradient is reversed, the direction of such diffusive salt transport is reversed.

Macroscopically, this mechanism is usually described in terms of an individual brine pocket. Here, the diffusion of salt downwards within the brine pocket causes the bottom of it to be dissolved, and the whole brine pocket moves (or migrates) downwards, a process that can be observed and measured (*e.g.* Harrison, 1965). However, while the speed of migration of a brine pocket can be investigated theoretically for various geometrically regular liquid inclusions (Tiller, 1963), the approach of mushy-layer theory is to average over the details of the geometry of the inclusions. In particular, equation (3.7) captures the average desalination rate caused by this mechanism and shows very concisely that the desalination rate is proportional to the (molecular) diffusivity of salt in water and the concentration (and hence temperature) gradient.

Since the diffusivity of salt in water is very low, brine-pocket migration is very slow, typically a small number of centimetres per month (Untersteiner, 1968; Weeks, 2010). It accounts for little salt transport, so we neglect it in this chapter.

Secondly, brine expulsion (Bennington, 1963) is caused by the smaller density of solid ice compared to liquid water, a difference of approximately 10%. As sea ice grows, brine at a given position within the ice becomes colder, and so the solid fraction rises, expelling brine downwards on average. The mechanism is sometimes described more mechanically, in terms of a pressure buildup causing a failure of the ice.

As with brine-pocket migration, we can describe this mechanism within mushy-layer theory using equation (3.3). A simple scaling analysis on this equation suggests that brine expulsion induces a vertical Darcy transport that is proportional to the density difference between the phases and the ice growth rate. This concords with the fuller analysis of Cox & Weeks (1975) and Notz (2005). One of the assumptions that we make below (section 6.4.1) is that the Darcy velocity associated with gravity drainage is much smaller than the ice growth rate, so neglecting brine expulsion is consistent with that assumption. In conclusion, brine expulsion redistributes salt within the ice. However, this mechanism causes no net salt flux from ice to the ocean (Notz, 2005; Notz & Worster, 2009), and we neglect it in this chapter.

Thirdly, there are a number of externally caused, pressure-driven flows inside sea ice. For example, there are high levels of snowfall off Antarctica, which can depress sea ice. This can cause brine to be displaced upwards and is thought to be the most important mechanism by which the snowpack is flooded with salty water (Maksym & Jeffries, 2000).

In terms of downwards transport of salt, flushing by meltwater that ponds on the surface of the ice is very significant in the summer when water from melt ponds can lead to rapid desalination of ice. Eicken *et al.* (2004) modelled this flow using Darcy's law, and it can be treated within the mushy-layer equations (section 3.3) through boundary conditions on the pressure field. Untersteiner (1968) estimated the magnitude of flushing and showed that it can account for much of the shape of the salinity profile of multi-year ice. However, for the purposes of this thesis, in which we focus on growing first-year ice, we neglect flooding and flushing, and instead focus on gravity drainage.

6.3 Physical description of gravity drainage

Fluid flow in sea ice associated with gravity drainage is not restricted to liquid brine channels; rather, that flow is part of a convective circulation that occurs throughout the porous ice, since the brine-rich liquid that leaves the ice through brine channels must necessarily be replaced by liquid flowing into the ice from the ocean. Therefore, there is a net upwelling in the bulk of the ice, a phe-

nomenon that has been observed by Eide & Martin (1975), who describe this as entrainment, but whose significance is arguably under appreciated.

In growing ice, convection is sustained by the following physical mechanism. The ice near a brine channel (both the solid matrix and interstitial brine) is cooled by conduction from the cold liquid flowing down the channel; relatively cold interstitial brine is also relatively concentrated, since the freezing temperature of salt water decreases with salinity, and to a very good approximation the interstitial brine is at local thermodynamic equilibrium (Feltham & Worster, 2000; Feltham *et al.*, 2006). This establishes the horizontal density gradient of the interstitial brine that sustains convection, and we determine this flow mathematically in section 6.4.

However, while postmortems of sea ice often reveal a brine drainage network that persists through much of its depth (e.g. Lake & Lewis, 1970), there is evidence (for example Eide & Martin (1975), discussed in section 6.5 below) that after an initial transient period when convection leading to brine transport can occur within the whole depth of ice, convection is confined to a relatively thin layer at the bottom of the ice, as indicated in figure 6.1. Confinement of convection arises where there is insufficient gravitational potential energy within the compositional density gradient to overcome thermal diffusion and viscous dissipation. This competition can be described by a local mush Rayleigh number: the upper part of the mushy layer has a Rayleigh number below the critical value required for convection and so is stagnant, whereas the lower part of the mushy layer has a Rayleigh number above the critical value and so convects. This interpretation was made following the field experiments of Notz & Worster (2008), developing the previous observation that the delayed onset of gravity drainage is controlled by a critical Rayleigh number (Worster, 1997; Wettlaufer *et al.*, 1997*b*). The brine in the stagnant layer is not necessarily 'trapped' in the sense of the ice being impermeable. Indeed, the permeability of sea ice remains a major open question (Freitag, 1999; Petrich *et al.*, 2006; Golden *et al.*, 2007) to which we return in section 7.4.

The flow within a brine channel itself is only part of the overall mechanism of gravity drainage in sea ice. While the channel flow has received much attention (for example Lake & Lewis (1970) use the theoretical study of convection in a

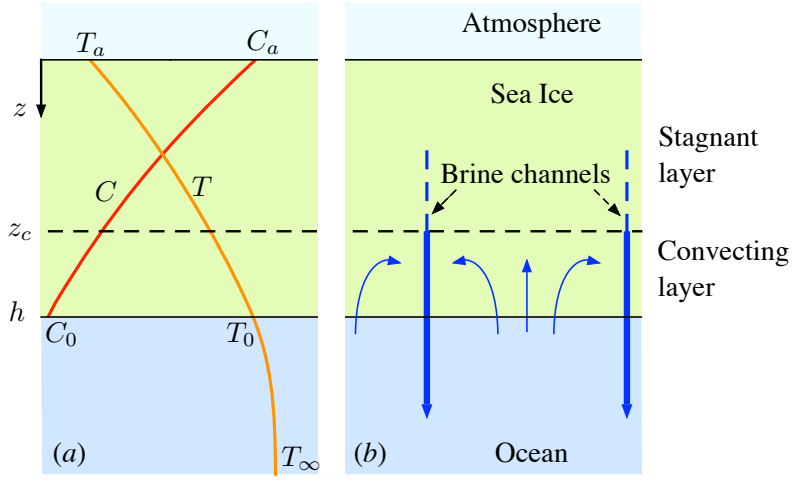

Figure 6.1: (a) schematic diagram of a one-dimensional model of sea ice showing typical temperature T and *interstitial* salinity C profiles. (b) sketch of convective flow within the ice (thin arrows) and down through brine channels into the ocean (thick arrows). Often this flow only occurs in a lower convecting layer between $z = z_c$ and $z = h$, as indicated. However, this is not a restriction imposed by our model.

semi-closed pipe by Lighthill (1953) to interpret flow in a brine channel, which is not appropriate since the surrounding ice is a porous medium), continuity requires that any description of gravity drainage must include the sustaining convective flow in the bulk of the ice.

6.4 Mathematical model

Here we present a simple framework in the context of idealized governing equations to determine the structure of this sustaining convective flow.

6.4.1 Governing equations

In the sense that sea ice is a two-phase, reactive porous medium, it constitutes a mushy layer (Feltham *et al.*, 2006). The mushy-layer equations introduced in section 3.3 adopt the approach of continuum mechanics in averaging equations of heat, salt and mass conservation over the two phases, using Darcy's law for the interstitial fluid flow, described by the Darcy velocity $\boldsymbol{u}$ and pressure p.

The temperature T and *interstitial* brine salinity C are coupled by local thermodynamic equilibrium and we assume that the associated liquidus relationship is linear. This allows us to introduce a single dimensionless variable for both: $\theta = (T - T_0)/\Delta T = -(C - C_0)/\Delta C$, where, in this chapter, $\Delta T = T_0 - T_a$ and $\Delta C = C_a - C_0$ are the temperature and interstitial salinity differences across the whole depth of ice, as shown in figure 6.1. Note that the liquidus temperature decreases with salinity and we are working on the left side of the phase portrait in figures 3.1 and 4.1*b*. However, as sea ice is solidified from above, it is dynamically equivalent to the situation considered in section 4.2. Taking the idealizations that we discuss below in the context of sea ice, we use the steady ideal mushy-layer equations introduced in section 3.3.2. These are given *non-dimensionally* by

$$\Omega\, \boldsymbol{u} \cdot \nabla\theta = \nabla^2\theta, \tag{6.1}$$

$$\nabla \cdot \boldsymbol{u} = 0, \tag{6.2}$$

$$\boldsymbol{u} = Ra\,(-\nabla p + \theta \boldsymbol{k})\,, \tag{6.3}$$

where $\boldsymbol{k}$ is a unit vector in the vertical direction.

The group $\Omega = 1 + L/c\,(T_m - T_a)$, where $T_m = 0°\mathrm{C}$ is the freezing point of pure water, c is the heat capacity of the ice and L is the latent heat of solidification, is the factor by which the effective heat capacity of sea ice is enhanced by phase change (Huppert & Worster, 2012). In particular, Ωc is a simplified form of the dimensional effective heat capacity derived by Feltham *et al.* (2006).

The important dimensionless Rayleigh number, which represents the ratio of available potential energy for convection to diffusive and dissipative effects, is defined by

$$Ra = g\beta\Delta C K H/\nu\kappa, \tag{6.4}$$

where g is acceleration due to gravity, κ is the thermal diffusivity, ν and ρ are the kinematic viscosity and density of water, $\beta = \rho^{-1}\partial\rho/\partial C$ is a solutal expansion coefficient (because salinity dominates temperature in causing variation in the density of the interstitial liquid) and K is a typical permeability. Note that in this chapter and the next, we use K rather than Π_0 for permeability, and Ra rather than R_m for the Rayleigh number, for consistency with the geophysical literature.

The permeability depends on the local porosity of the convecting layer; however, for practical applications of our model, K can be taken as a mean value over the convecting layer (*cf.* Notz & Worster, 2008, and section 7.2.3 below). The use of a uniform permeability in the CAP model is one of the most important simplifications. We use a quasi-steady approximation in which the growth rate $\dot{h}$ is constant on the timescale of convective turnover ($\dot{h} \ll w$) in which case an appropriate vertical length scale is $H = \kappa/\dot{h}$, *cf.* equation (3.22).

The idealizations made in (6.1–6.3) isolate the mechanism of gravity drainage as follows. Firstly, we neglect the diffusion of salt, which accounts for brine pocket migration. Secondly, we neglect all differences in the properties of the phases, including the roughly 10% difference in density that accounts for brine expulsion. Note that there are more significant differences in the thermal properties (see table 7.1 in the following chapter). Thirdly, we assume that $\dot{h} \ll w$, the vertical Darcy velocity, such that the dominant balance in the heat equation is between conduction and convective transport. The resulting equations (6.1–6.3) provide the simplest meaningful mathematical description of convection within sea ice.

Given the assumptions underlying the ideal mushy-layer equations, the equation expressing conservation of salt (3.7)

$$\frac{\partial S}{\partial t} = -w\frac{\partial C}{\partial z} \tag{6.5}$$

is decoupled from equations (6.1–6.3) describing buoyancy-driven flow (*cf.* Worster, 1997). In this equation, $S = (1-\phi)C$ is the bulk salinity, since we may neglect the salt content of solid ice, which is very small, and we have also neglected diffusion of salt as discussed above. Then, having determined the upwelling velocity w as we describe below, equation (6.5) can be used to determine the evolution of bulk salinity field and hence the solid fraction ϕ.

6.4.2 CAP model for sea ice

The Chimney-Active-Passive (CAP) model provides a simple characterization of convective solutions to (6.1–6.3). Full mathematical details are presented in chapter 4. The CAP model can be applied in both two and three dimensions. Here,

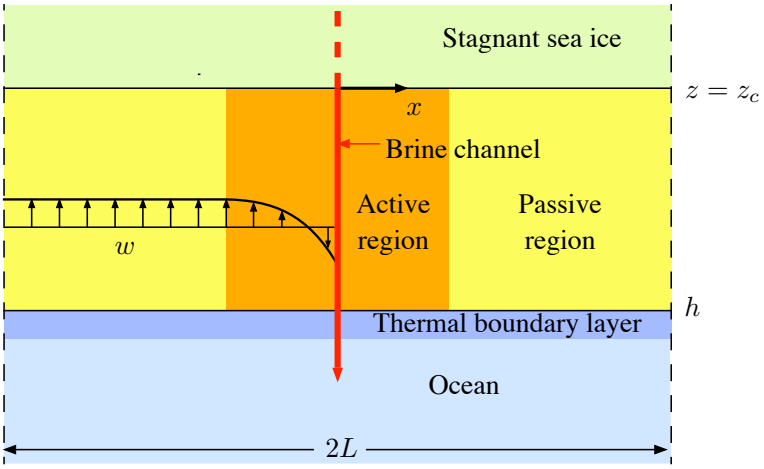

Figure 6.2: The Channel-Active-Passive (CAP) model. The vertical component of Darcy velocity w is uniform in the passive region but changes in the active region owing to the horizontal density gradient driving convection. Note that the shape of the isotherms is similar to the profile of vertical velocity: the temperature is horizontally uniform in the passive region and lower in the active region near the brine channel.

we review the approach as applied to a periodic planar array of brine channels of separation $2L$ in the case of a confined convecting layer $z_c \leq z \leq h$, as shown in figure 6.2. Note that we have moved from steady, directional solidification to the transient growth of sea ice by means of the quasi-steady assumption introduced in the previous section.

The temperature in the passive region is horizontally uniform and vertically linear, which is appropriate for a relatively thin convecting layer. Therefore,

$$\theta = \theta_0 \left(z - h\right) / \left(z_c - h\right), \quad z_c \leq z \leq h, \tag{6.6}$$

where $\theta_0 = -\Delta C_e / \Delta C$, in which $\Delta C_e = C_c - C_0$ is the interstitial brine salinity difference across the convecting layer. Although there are known to be horizontal inhomogeneities in bulk salinity caused by brine channels (Cottier *et al.*, 1999), the temperature field away from brine channels is assumed to be horizontally homogenous in experimental measurements of sea ice. Horizontally uniform upwelling velocities are consistent with horizontally uniform solutions for θ and

the most general streamfunction of this form that satisfies no flow through the periodic boundary at $x = L$ or at the top of the convecting region at $z = z_c$ is

$$\psi \propto (L - x)(z - z_c), \tag{6.7}$$

which corresponds to horizontally uniform upwelling.

The overall strength of the flow, or equivalently the proportionality factor in (6.7), is determined by matching this uniform upwelling in the passive region to the active region near the channel where the temperature is not horizontally uniform.

The salt flux from the ice into the ocean depends on channel spacing L. In section 4.4, we showed that there is both a minimum channel spacing and also a minimum width of the active region needed in order to sustain gravity drainage through channels. Therefore, horizontal density gradients in the surrounding ice sustain gravity drainage through channels.

However, the (mean) channel spacing L remains undetermined. As discussed in section 4.5, we assume that L takes the value that maximizes the salt flux. This avoids prescribing L, which is not an external parameter in sea-ice formation (in contrast to some experimental systems, such as Zhong *et al.*, 2012), and importantly allows us to determine the solution completely in terms of a single proportionality factor $W(\Omega)$ which can be computed cheaply. Note that, in terms of the quantities discussed in section 4.5,

$$W(\Omega) = 1/h_c(\Omega) \approx 2\gamma_c(\Omega), \tag{6.8}$$

where γ_c is the proportionality factor in the relationship between solute flux and Rayleigh number. The latter relationship in (6.8) is as we would expect from scaling analysis. We show a graph of the proportionality factors in figure 6.3. However, since the model includes a number of idealizations, for quantitative implementation we propose tuning this factor with experimental results.

In conclusion, the dimensional vertical component of Darcy velocity w in the passive region, which gives a measure of the mean upwelling outside the brine

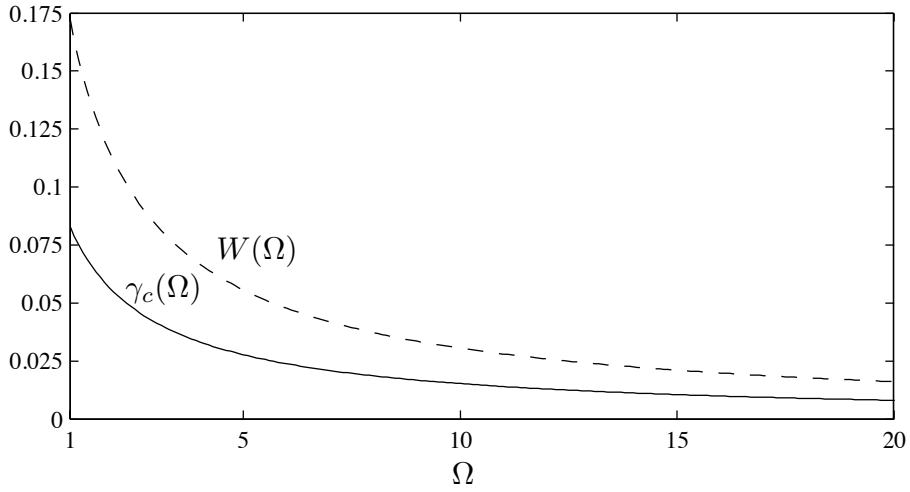

Figure 6.3: The behaviour of the proportionality factor $W(\Omega)$. For reference we include $\gamma_c(\Omega)$ from figure 4.8.

channel, is

$$w = -\frac{\kappa}{h - z_c} Ra_e \frac{z - z_c}{h - z_c} W(\Omega), \tag{6.9}$$

where

$$Ra_e = \left[g\beta \Delta C_e K \left(h - z_c \right) \right] / \nu\kappa, \tag{6.10}$$

is an effective Rayleigh number across the convecting layer, generalizing the result (equation 4.34) found for full-depth convection. The fact that w is proportional to a Rayleigh number strictly only applies in a planar geometry, but can be considered a reasonable approximation across a limited parameter range in three dimensions. The result that w is vertically linear applies both in planar and axisymmetric geometries. By integrating equation (6.5) for local salt conservation using equation (6.9) for the upwelling velocity w, we can determine the net salt flux from the mushy layer due to gravity drainage.

6.4.3 Comparison with some alternative models

Studies of sea ice at the polar-ocean scale use parameterizations of gravity drainage (Vancoppenolle *et al.*, 2009*b*, 2010; Petrich *et al.*, 2011; Jeffery *et al.*, 2011; Saenz & Arrigo, 2012; Turner *et al.*, 2013; Griewank & Notz, 2013). Our conclusions contrast with some of these recent suggestions about parameterizations of gravity

drainage. They are fundamentally different to enhanced molecular diffusion or mixing-length diffusion (Vancoppenolle *et al.*, 2010; Jeffery *et al.*, 2011); gravity drainage is an advective process. Consistent with this, our advective parameterization always transports salt (and any passive tracers) in the direction of the fluid flow, and necessarily desalinates ice. By contrast, diffusive parameterizations imply down-gradient transport.

Our model is closer to the prescription of a vertical velocity proportional to a Rayleigh number proposed by Petrich *et al.* (2011); our mathematical modelling provides a solid justification for this kind of approach. However, whereas they impose a vertically uniform vertical velocity, we determine a linear structure (6.9). Our concept of the passive region matched to the active region around brine channels shows theoretically that horizontally uniform vertical velocity corresponds to vertically linear vertical velocity. The concept of Petrich *et al.* (2011) requires much of the interstitial liquid to enter the brine channel at the top of the convecting region by conservation of mass. This seems unlikely both given the description of the nature of convection we argued for in section 6.3, and also given the observed tributary structure to the brine drainage systems (e.g. Lake & Lewis, 1970). Furthermore, the linear structure of the vertical component of the Darcy velocity given in (6.9) that we found is consistent with the experimental observations of Eide & Martin (1975) and Chen (1995), as we demonstrate below.

However, our model is closest to Turner *et al.* (2013) and Griewank & Notz (2013). Nevertheless, as with Petrich *et al.* (2011), there are important differences between these models and our own in terms of the vertical structure of w. We discuss the parameterizations of Turner *et al.* (2013) and Griewank & Notz (2013) in section 8.1.3 in the context of implementation of the parameterizations in a one-dimensional sea-ice model.

6.5 Analysis of previous experiments

Eide & Martin (1975) investigated the interstitial flow by injecting dye into the liquid beneath growing ice in a laboratory and observing its horizontally uniform "entrainment" into the ice. For two cases, they measure the average height of the dye front as a function of time, which we reproduce in figure 6.4, to which they

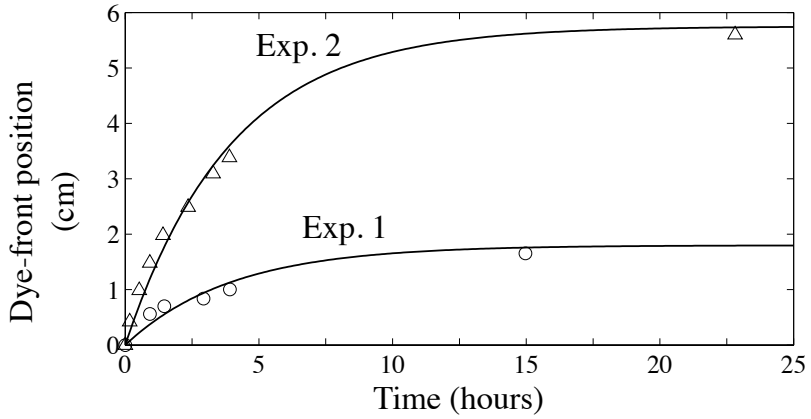

Figure 6.4: Reproduced from Eide & Martin (1975). Height of dye front above interface height for two experiments. The exponential fits of the form $a\,[1-\exp(-bt)]$ are part of the original figure. For both experiments $b = 7\times10^{-5}$ s^{-1}, while, for experiment 1, $a = 1.8$ cm, and, for experiment 2 when the ice was three times thicker, $a = 5.75$ cm. That b is approximately unchanged hints at the possibility that the permeability K has increased to compensate for the likely slackening of the brine salinity gradient $\Delta C_e/h - z_c$. Combined with the increase in $a = h - z_c$, equation (6.14) suggests that the effective Rayleigh number Ra_e increased. However, it is difficult to draw comparisons between only two experiments, especially as in the first experiment the ice was growing sufficiently rapidly that the quasi-steady approximation is unreliable.

fit exponential curves of the form $a\,[1-\exp(-bt)]$.

The exponential time-dependence is explained by our simple model, and fundamentally arises from the linear vertical structure we found for the vertical velocity. Neglecting diffusion of the dye, the position of the dye front $z_d(t)$ is governed by

$$\frac{dz_d}{dt} = w\,(z_d,t) = -b\,(z_d - z_c)\,, \tag{6.11}$$

using (6.9), where $b = Ra_e W(\Omega)\kappa/\,(h-z_c)^2$. This equation can be integrated immediately, assuming that the depth of the convecting layer $h - z_c$ evolves slowly compared to the dye-front position z_d. Integrating equation (6.11) with the initial condition $z_d(0) = h$, we find that the height of the dye front satisfies

$$h - z_d = (h - z_c)\,[1-\exp(-bt)]\,. \tag{6.12}$$

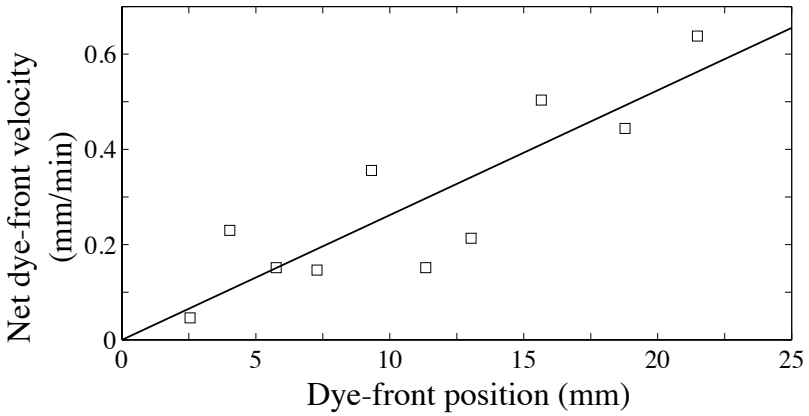

Figure 6.5: Reprocessed data from Chen (1995) showing that a straight line through the origin gives a good fit, as predicted by (6.11).

This exponential time-dependence contrasts, for example, with the piecewise linear time-dependence that results from the model of Petrich *et al.* (2011). Equation (6.12) provides a simple interpretation of a and b in Eide & Martin (1975):

$$a = h - z_c, \tag{6.13}$$

the depth of the convecting layer, and, on rearrangement,

$$b = Ra_e \frac{\kappa}{(h - z_c)^2} W(\Omega) \equiv \frac{g\beta}{\nu} \frac{\Delta C_e}{h - z_c} KW(\Omega). \tag{6.14}$$

Further confirmation of the linear vertical structure in (6.11) comes from the experiments of Chen (1995) on a different physical system. In these experiments ammonium-chloride solution was solidified from below and dye injected into the liquid melt. By using finite differences, and making a correction for a dye-sinking rate extracted from a control experiment before the onset of convection within the mushy layer, we could estimate a net dye-front velocity caused by convection, extending a calculation by Chen (1995). Motivated by (6.11), we plot this velocity against the dye-front position in figure 6.5. The reasonable fit provides further confirmation of the linear structure of w and the slope of this graph is a measure of b. Note that, for this experiment, convection appeared to penetrate the whole

depth of the mushy layer and so $z_c = 0$. This is likely to be caused by the high permeability of the mushy layer of ammonium-chloride crystals that formed in this experiment.

6.6 Conclusions

Gravity drainage is the most important mechanism by which first-year ice desalinates. Brine-pocket migration and brine expulsion are observable but very slow processes that can be neglected during first-year growth, although brine expulsion may be somewhat important in redistributing salt within sea ice. Only after the first winter of growth does meltwater flushing become significant, although other pressure-driven flows such as flooding may be important in the winter, especially in the Antarctic.

Therefore, we developed a series of idealizations that isolate the mechanism of gravity drainage. We derived a new parameterization of gravity drainage in sea ice theoretically in terms of two unknown parameters. Our mathematical modelling and experimental comparison indicate the existence of a convecting layer in which the mean upwelling velocity is vertically linear and proportional to an effective Rayleigh number. The dye-front experiments described above offer a systematic way to investigate both the behaviour of the tuning parameter $W(\Omega)$ and also the question of how the depth of the convecting layer $h - z_c$ is determined physically. A theoretical determination of the latter is required for a complete implementation of our model, and we develop such a proposal in section 7.2.3 below.

The CAP model constitutes a new dynamical approach to modelling gravity drainage from sea ice. Using the CAP model to determine the vertical upwelling velocity w allows a thermodynamic sea-ice model to determine, rather than prescribe, the bulk salinity profile, and we implement this idea in the following chapter. Such a modified sea-ice model conserves salt as well as heat in the ice–ocean system, and dynamically determines the heat capacity and thermal conductivity of the ice, the additional vertical heat transport due to convection within the ice, and net brine fluxes into the ocean.

Chapter 7

One-dimensional model of sea ice

The content of this chapter has been submitted to the Journal of Geophysical Research (Rees Jones & Worster, 2013c).

7.1 Introduction

7.1.1 Sea ice: climate and models

Sea ice forms a dynamic interface between the ocean and atmosphere and so constitutes an integral aspect of any coupled climate model (Gent, 2012). It plays an important role in the regional and global climate, as discussed in section 2.1.

Coupled climate models account for the thermodynamic growth and melting of sea ice, the movement of sea ice due to wind stress, its response to internal stresses, lateral melting and the formation of pressure ridges (*e.g.* Hunke & Lipscomb, 2008; Vancoppenolle *et al.*, 2009*a*,*b*), as discussed in section 2.2. In this chapter, we restrict attention to the thermodynamic growth of sea ice, which is a one-dimensional process. This accounts for much of the change at the thin-ice end of the ice-thickness distribution used in climate models, and so is particularly important for salt fluxes, as these are much greater for thinner ice. The one-dimensional, dynamic-salinity model that we develop is structurally similar to fixed-salinity models currently used in coupled climate models. Fixed-salinity models solve a heat equation in which the thermal properties of ice – its heat

capacity and conductivity – depend on the temperature and salinity of the ice. They are deficient in that, while the temperature is determined as part of the solution, the salinity field is prescribed. By contrast, in our new model, the salinity is determined dynamically.

There has been much recent interest in determining the salinity of sea ice dynamically. Some studies are at a small scale and resolve gravity drainage in two-dimensional numerical simulations (Oertling & Watts, 2004; Wells *et al.*, 2011). Other studies are at the polar-ocean scale and parameterize gravity drainage (Vancoppenolle *et al.*, 2009*b*, 2010; Jeffery *et al.*, 2011; Saenz & Arrigo, 2012; Turner *et al.*, 2013; Griewank & Notz, 2013). Their parameterizations variously involve, sometimes in combination, relaxation of the salinity profile, enhanced molecular diffusion, mixing-length diffusion, empirical formulae based on the measurements of Cox & Weeks (1988), and a local Rayleigh number. Our approach is to take the simple theoretical model of gravity drainage in terms of a Rayleigh number derived from small scale models developed in the previous chapters and cast it in a form appropriate to these large scale models. The other mechanisms of desalination discussed in section 6.2 could in principle also be included in a model – here we focus on the most important mechanism in first-year ice (and indeed in the laboratory experiments we consider). Our model can be considered one of a new generation of dynamic-salinity sea-ice models and is most similar to Turner *et al.* (2013) and Griewank & Notz (2013). We discuss how our model compares to those two models in section 8.1.3.

7.1.2 Desalination of sea ice: modelling gravity drainage

In chapter 4, we developed the CAP model, which allows us to parameterize the convective upwelling velocity in a way that captures the underlying physics. The interstitial brine is relatively saline compared with the ocean, so the convective upwelling amounts to a net desalination. The upwelling is balanced by downward flow in the brine channels and results in brine fluxes into the ocean. Two parameters in our model – a critical Rayleigh number and a proportionality constant – have been calculated in idealized situations, for example by Wells *et al.* (2010, 2013) and also in figure 6.3. However, in this chapter, we treat them as tuning

parameters that we adjust to describe the laboratory experiments of Wettlaufer *et al.* (1997*a*) and Notz (2005).

For all but the thinnest ice, only the lowermost regions of sea ice convects, as discussed in the previous chapter. There we identified the need to determine the depth of the convecting layer theoretically. It is now well established that a Rayleigh number governs the onset of convection in mushy layers such as sea ice (Worster, 1992*b*, 1997) and so we propose using a *local* Rayleigh number to determine the thickness of the convecting layer, as suggested by Notz & Worster (2008). In sea ice, strongly varying permeability is responsible for the confinement of convection; in other physical systems, the mechanism can differ. For instance, in experiments analogous to sea ice but using sugar instead of salt (Aussillous *et al.*, 2006) and in the 'stagnant-lid' mode of convection in magma chambers (Davaille & Jaupart, 1993), confinement is thought to be caused by the strong variation of viscosity with temperature. Our approach here, which is based on fundamental physical principles, should be generalizable to such systems.

In section 7.2, we develop our model starting with the phase-averaged mushy-layer equations for heat and salt conservation in one spatial dimension from chapter 3. In the case of non-convecting sea ice, Feltham *et al.* (2006) have shown that these equations are essentially equivalent to those used in generations of models derived from the fundamental description given by Maykut & Untersteiner (1971), including Bitz & Lipscomb (1999) which is used in CICE: the Los Alamos Sea Ice Model (Hunke & Lipscomb, 2008). Our model develops these further by determining a convecting upwelling velocity internal to the sea ice and we compare our model to CICE in chapter 8.

In section 7.3, we compare results from our model with measurements from laboratory experiments in order to test the predictive ability of our model in terms of sea-ice growth and salt fluxes.

Finally, in section 7.4, we consider the open question of the permeability of sea ice, which in part determines the strength of gravity drainage. We test the approach adopted in previous sections by applying our model to a wide range of problems in order to analyze indirectly the relationship between the porosity and permeability of sea ice, highlighting the distinction between local and bulk permeability.

7.2 Model formulation

7.2.1 Model configuration

We consider ice grown from an upper cold plate of temperature $T_B(t)$, as shown in figure 7.1. This configuration allows for comparison with experiments. Our model dynamically evolves the internal temperature T and bulk salinity S of the ice using a parameterized vertical Darcy velocity w. It is important to note that the bulk salinity is always less than the interstitial salinity C, which is not an independent variable but coupled to T through the liquidus relation $C = C_L(T)$, since sea ice can be assumed to be at local thermodynamic equilibrium internally (Feltham & Worster, 2000; Feltham *et al.*, 2006). We use $T = T_L(C)$ to denote the inverse of this relationship. The salinities S and C are related through the solid fraction ϕ, previously introduced in equation (3.1), by

$$S = (1 - \phi)C + \phi C_s \approx (1 - \phi)C, \tag{7.1}$$

given that the salinity of solid ice $C_s \approx 0$. We rearrange equation (7.1) to determine the solid fraction

$$\phi(T, S) = 1 - S/C_L(T). \tag{7.2}$$

Sea ice of thickness $h(t)$ grows into a tank of fixed depth H. We take the purely liquid region in the tank (which in this chapter we refer to as the 'ocean') to be well mixed, owing to thermal and compositional convective mixing, having temperature $T_l(t)$ and salinity $C_l(t)$. This treatment of the ocean is approximate but is appropriate for this study as it is not part of the sea-ice component of a coupled climate model.

7.2.2 Model equations

Sea ice is a multiphase, reactive porous medium and so is an example of a wider class of systems called mushy layers, which we introduced in chapter 3. The mushy-layer equations discussed in that chapter for heat and salt conservation (3.4, 3.5) can be used to derive our model equations in one spatial dimension,

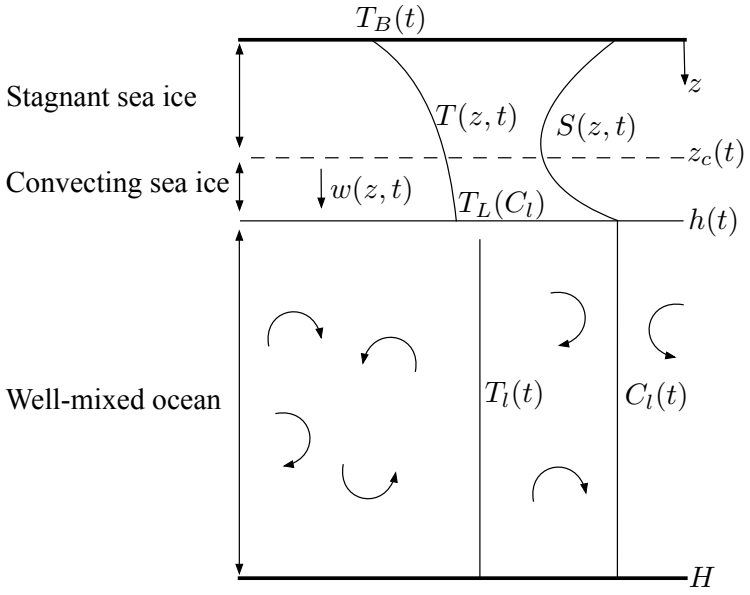

Figure 7.1: One-dimensional model of convection. The sea ice (mushy layer) is divided into a stagnant layer and a convecting layer, as discussed in the text. Note that there is a thin thermal boundary layer (exaggerated) at the interface between the mushy layer and the ocean (the purely liquid region) across which the modelled temperature field is discontinuous.

generalizing Feltham *et al.* (2006),

$$c_i \frac{\partial T}{\partial t} + c_w w \frac{\partial T}{\partial z} = \frac{\partial}{\partial z}\left(k_i \frac{\partial T}{\partial z}\right), \tag{7.3}$$

$$\frac{\partial S}{\partial t} = -w \frac{\partial C}{\partial z}, \tag{7.4}$$

in which the major novelty is that we include a convective Darcy velocity w due to gravity drainage

$$w = \begin{cases} -\alpha Ra_e \dfrac{k_l}{c_l} \dfrac{z - z_c}{(h - z_c)^2} & \text{if } z \geq z_c \\ 0 & \text{if } z < z_c \end{cases} \tag{7.5}$$

where α is a dimensionless prefactor (called $W(\Omega)$ in chapter 6), Ra_e is an effective Rayleigh number and z_c is the position of the top of the convecting layer determined in section 7.2.3 (*cf.* figure 7.1). Since we focus on gravity drainage, we have neglected diffusion of salt in (7.4), which is small.

Volumetric heat capacities of sea ice are determined by averaging over the two phases and accounting for the latent heat of fusion L per unit volume of solid formed at 0°C (Notz, 2005; Feltham *et al.*, 2006). In this, we generalize the 'classical' expression (Malmgren, 1927) to a nonlinear liquidus. We neglect the difference between the heat capacities of the solid and liquid phases (which is equivalent to a temperature-dependent latent heat) and the heat of solution, as these are both $O(1\%)$ combined on average, as shown in figure 7.2. Thus

$$c_i(T, S) = c_s - LSC'_L C_L^{-2}, \tag{7.6}$$

$$c_w(T, S) = c_l - \frac{LC'_L}{C_L}. \tag{7.7}$$

Likewise, the thermal conductivity of sea ice (Ono, 1968; Batchelor, 1974)

$$k_i(T, S) = k_s - (k_s - k_l)\, SC_L^{-1}, \tag{7.8}$$

In these expressions, subscripts s and l represent properties of solid and liquid phase respectively. In this, we relax the assumptions of ideal mushy-layer theory

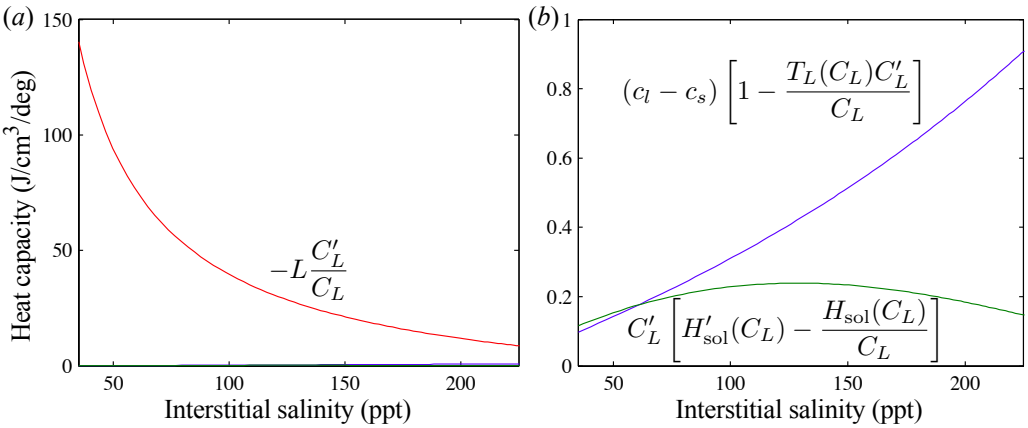

Figure 7.2: The heat capacity of sea ice is dominated by latent heat release (a). Corrections due to the difference in heat capacities between the phases and the heat of solution $H_{\rm sol}$ are shown in (b). Note the different vertical axes, which must both be multiplied by S/C_L in equation (7.6) to obtain the contribution to the heat capacity of sea ice. Note also that the interstitial salinity axis is equivalent to a temperature axis running from about $-2°$C to $-20°$C.

(section 3.3.1) that these properties are independent of phase. Throughout this chapter we take parameter values, listed in table 7.1, appropriate to the solidification of aqueous sodium chloride, since it is the most abundant salt in seawater and allows direct comparison with the laboratory experiments discussed in section 7.3.1. We use a cubic

$$C_L(T) = -17.6T - 0.389T^2 - 0.00362T^3 \tag{7.9}$$

for the liquidus salinity (Weast, 1971), and C_L' denotes the derivative of C_L with respect to T. For sea ice, the expression given by Assur (1958) should be used.

7.2.3 Parameterization of convective velocity w: applying the CAP model

The key novelty in our model is that we determine the convective velocity w dynamically from a simple physical parameterization. In chapter 6, we applied a steady-state study of mushy-layer convection (chapter 4) to transient sea-ice growth, which we now apply to a one-dimensional model as follows.

Parameter	Value (cgs units)	Reference
c_l	4.0 J/cm^3/deg	Weast (1971)
c_s	1.9 J/cm^3/deg	Weast (1971)
k_l	0.00523 J/s/cm/deg	Lange & Forke (1952)
k_s	0.0214 J/s/cm/deg	Slack (1980)
L	306 J/cm^3	Kerr *et al.* (1990)
g	980 cm/s^2	
ν	0.018 cm^2/s	Ozbek *et al.* (1977)
K_0	10^{-4} cm^2	Freitag (1999)
β	7.5×10^{-4} 1/ppt	Ruddick & Shirtcliffe (1979)
λ	0.12	Wettlaufer *et al.* (1997*a*)

Table 7.1: Material parameters used in calculations. Note that sometimes a measurement per unit mass has been converted to a one per unit volume. Many quantities vary with temperature but we have chosen a representative value.

The thickness of the convecting layer and the strength of convection are set by a depth-dependent *local* Rayleigh number introduced in section 6.3

$$Ra(z) = \frac{c_l g \beta}{k_l \nu} \left[C_L(T(z)) - C_L(T_l) \right] (h - z) K(z), \tag{7.10}$$

based on the ratio of the potential energy difference from a height z to the ice–ocean interface h relative to the thermal diffusion and the viscous dissipation caused by the flow required to replace the fluid that moves into the ocean. When this ratio is sufficiently large, there is enough potential energy for convection to occur. Note that the ratio of an advective to a diffusive timescale discussed in Griewank & Notz (2013) is better thought of as Péclet number, which is itself a function of the Rayleigh number.

We take the harmonic mean permeability

$$K(z) = K_0 \left[\frac{1}{h - z} \int_z^h \frac{1}{K_l(\phi(z'))} \, dz' \right]^{-1}, \tag{7.11}$$

where K_0 is a dimensional constant (see table 7.1) and $K_l(\phi) = (1 - \phi)^3$ is a dimensionless local relationship between porosity and permeability. The latter was suggested by Worster (1992*b*) as a simplified form of the Kozeny porosity–permeability relationship and used by various subsequent studies of convection in

a mushy layer (*e.g.* Amberg & Homsy, 1993; Schulze & Worster, 1998; Chung & Worster, 2002; Wells *et al.*, 2010, 2013). The harmonic mean in equation (7.11) reduces to $K = K_0(1-\phi)^3$ if ϕ is constant, which is approximately the same as the experimental fit to measurements of Freitag (1999), $K \propto (1-\phi)^{3.1}$. The harmonic mean is appropriate in that it is the bulk permeability of a series of layers of varying permeability (Phillips, 1991), on the assumption that the flow is dominantly vertical. This measure appropriately accounts for the fact that a fluid parcel being replaced at the top of the mushy layer needs to move through all the layers beneath it. Note that, in their expressions for the local Rayleigh number, Notz & Worster (2008) and Vancoppenolle *et al.* (2010) take $K(z)$ to correspond to the least-permeable layer between height z and the ice–ocean interface, which is comparable since the harmonic mean is dominated by the least permeable region. From a computational perspective, their expressions have the potential disadvantage of behaving very non-locally. However, we acknowledge that our expression is only tentative. The uncertainty arises from difficulties in making direct measurements, and we discuss recent suggestions and our own contribution in section 7.4.

The local Rayleigh number defined by equation (7.10) is used to determine both the region of convection (figures 7.1 & 7.3) and also an effective Rayleigh number governing the strength of convection in equation (7.5) as follows. If $Ra(z)$ is everywhere less than a critical value R_c (figure 7.3*a*), there is no convecting layer and $Ra_e = 0$. Otherwise, there is convection in the region between the ice–ocean interface $z = h$ and some critical depth $z = z_c$, which we determine as follows. If $Ra(0) \geq R_c$, then the whole mushy layer convects ($z_c = 0$, figure 7.3*c*, *d*). Otherwise, if $Ra(0) < R_c$, there is a first point z_c such that $Ra(z_c) = R_c$ (figure 7.3*b*). A fluid parcel at this depth has enough potential energy to convect through the whole depth below it $z_c \leq z \leq h$, being replaced by fluid rising up through the rest of the layer.

Finally, motivated by Wells *et al.* (2010, 2011, 2013), we define an effective Rayleigh number in terms of the degree of supercriticality,

$$Ra_e = \max_{z_c \leq z \leq h} Ra(z) - R_c, \tag{7.12}$$

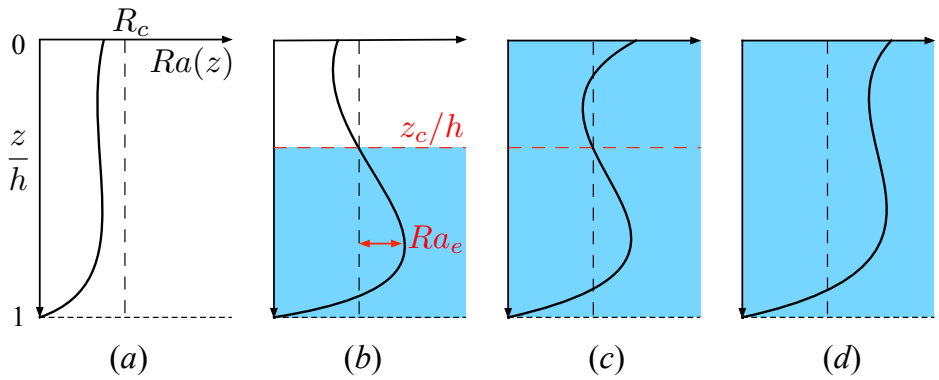

Figure 7.3: The convecting layer with various types of local Rayleigh number profile. (a) No convection, since $Ra(z)$ is everywhere subcritical. (b) A lower layer convects. The effective Rayleigh number Ra_e is specified in equation (7.12) and used in equation (7.5). (c, d) Full-depth convection. We also investigated an alternative parameterization in which convection is confined below the dashed red line in (c).

as marked in figure 7.3b. Other parameterizations are possible; in particular, we investigated both confining convection in the case of figure 7.3c and also letting

$$Ra_e = \max_{z_c \le z \le h} Ra(z), \tag{7.13}$$

which shares with (7.12) the property that flux is proportional to Rayleigh number at large Rayleigh number (as shown for a planar array of channels in chapter 4, *cf.* also Wells *et al.*, 2010, 2013), but found that these parameterizations were less satisfactory.

7.2.4 Boundary conditions at the ice–ocean interface

Here, we apply and in some cases extend the boundary conditions introduced in section 3.4. We assume that the temperature of the interface is equal to the liquidus temperature at the salinity of the well mixed ocean (Worster, 1986) and that the bulk salinity is continuous, which is equivalent to a zero solid fraction at the interface, consistent with the field observations of Notz & Worster (2008).

Therefore,

$$T = T_L(C_l), \quad S = C_l \qquad (z = h). \tag{7.14}$$

The growth of sea ice is determined by conservation of heat at the interface. A balance of heat fluxes across a control volume enclosing the interface and the thin thermal boundary layer in the ocean gives

$$c_l \left[T_l - T_L(C_l)\right] \left(\dot{h} - w\,|_{z=h}\right) + L\dot{h}\phi\,|_{z=h} + F_T = k_m \left.\frac{\partial T}{\partial z}\right|_{z=h^-}. \tag{7.15}$$

In laboratory experiments, the turbulent heat flux from the ocean F_T is caused by natural convection driven by the density difference between fluid at the interface and fluid in the interior, in which case

$$F_T = \left(2^{4/3}\lambda\right) k_l \left(\frac{\alpha_T g c_l}{k_l \nu}\right)^{1/3} \left[T_l - T_L(C_l)\right]^{4/3}, \tag{7.16}$$

where $\alpha_T = \alpha_T\left(T_L\left(C_l\right), C_l\right)$ is a temperature and salinity-dependent thermal expansion coefficient calculated from the density measurements of Ruddick & Shirtcliffe (1979). This is appropriate for a tank (or ocean mixed layer) of constant depth, although the mixed-layer depth changes significantly over the course of the winter. The ocean is cooled by the turbulent heat flux and evolves according to

$$c_l (H - h) \frac{dT_l}{dt} = -F_T. \tag{7.17}$$

For implementation in a climate model, a friction velocity could be used in calculating F_T (Maykut & McPhee, 1995). Indeed, sea-ice thickness after sufficiently long times is known to be very sensitive to the parameterization of oceanic heat flux (*e.g.* Maykut & Untersteiner, 1971; Holland *et al.*, 1997), and weaknesses in our parameterization of F_T may explain some of the discrepancy between our model and experimental observations shown in section 7.3.4. Note that, in our model, the term for latent heat released at the interface in equation 7.15 $L\dot{h}\phi\,|_{z=h} = 0$, since the solid fraction there is zero. However, we retain it to accommodate fixed-salinity models, in which the solid fraction at the interface is nonzero, in section 8.

The salt flux from the sea ice to the ocean, the definition of which we discuss in more detail in section 8.2, is given by

$$F_S = -\int_0^h \frac{\partial S}{\partial t}\, dz + \dot{h}\Delta S. \tag{7.18}$$

The salt flux consists of the net change in the internal salinity of the ice and brine rejection at the ice–ocean interface associated with a salinity discontinuity ΔS there. In our model, $\Delta S = 0$ (from equation 7.14) and the change to internal salinity is caused by gravity drainage alone.

As ice grows, the salinity of the remaining well mixed ocean increases according to

$$(H - h)\frac{dC_l}{dt} = F_S. \tag{7.19}$$

However, within our numerical scheme, we prefer to apply global conservation explicitly using quadrature. Further details about our numerical method are given in appendix 7.A.

7.2.5 Model calculations

In order to illustrate the behaviour of our model, figure 7.4 shows our results for a simulation in which ice is grown from a cold plate at constant temperature $T_B = -20°\text{C}$. For this calculation, we fixed the salinity $C_l = 35.5$ ppt and temperature $T_l = -1.9°\text{C}$ of the ocean to simulate a constant ocean heat flux of 2.25 W/m^2 appropriate to the polar oceans (Maykut & Untersteiner, 1971). As the sea ice grows, we continually update the temperature and salinity fields within the ice and use these to calculate the solid fraction (equation 7.2) and local Rayleigh number (equation 7.10) used in our parameterization of convection.

The temperature field (figure 7.4*a*) is approximately linear with depth, so the sea ice grows approximately diffusively with a balance between internal latent heat release and conduction to the cold plate. At later times the temperature gradient becomes shallower, so the heat flux from the ocean becomes significant and slows the ice growth, eventually leading to a steady state. In these respects, our model differs little from other thermodynamic sea-ice models.

However, by allowing the salinity field (figure 7.4*b*) to evolve, our model cap-

tures the gradual desalination of sea ice caused by convection, which leads to C-shaped salinity profiles, as are commonly observed in first-year ice. Throughout the calculation, the salinity at the interface with the ocean region remains fixed. The amount of desalination is controlled by the choice of critical Rayleigh number R_c: at smaller R_c, the ice desalinates more before convection shuts down. We explore this effect more thoroughly in section 7.3, in which we compare predicted salt fluxes against those observed in laboratory experiments. At the ice–cold-plate interface, the salinity is steady since the vertical upwelling velocity associated with convective desalination is zero there.

The desalination of the sea ice causes the local solid fraction to increase over the course of the experiment (figure 7.4*c*). Note that the rapid change in solid fraction near the ice–ocean region interface causes a rapid change in thermal properties of the ice, causing some nonlinearity in the temperature field (which is sometimes more pronounced than in figure 7.4*a*).

The local Rayleigh number (figure 7.4*d*) typically peaks around the chosen R_c because desalination causes the local Rayleigh number to relax back towards this value. There is usually one peak near the ice–ocean interface, and another near the cold plate. We suspect the latter is a result of our neglect of solar radiation, and brine expulsion, which would transport salt downwards within the ice, increasing the solid fraction in the upper ice and thereby reducing the permeability and local Rayleigh number. We discuss its evolution further in section 7.3.3 when discussing convection in laboratory experiments.

7.3 Results compared to laboratory experiments

7.3.1 Discussion of experimental systems

We test our parameterization of gravity drainage by comparing its predictions to the results of two sets of laboratory experiments reported in Wettlaufer *et al.* (1997*a*) and Notz (2005). The latter are also reported in less detail in Notz *et al.* (2005) and Notz & Worster (2008). The basic systems are very similar: a coolant is circulated to maintain at constant temperature a brass cold plate mounted at the top of an insulated tank of horizontal size 20×20 cm and vertical size 37.6

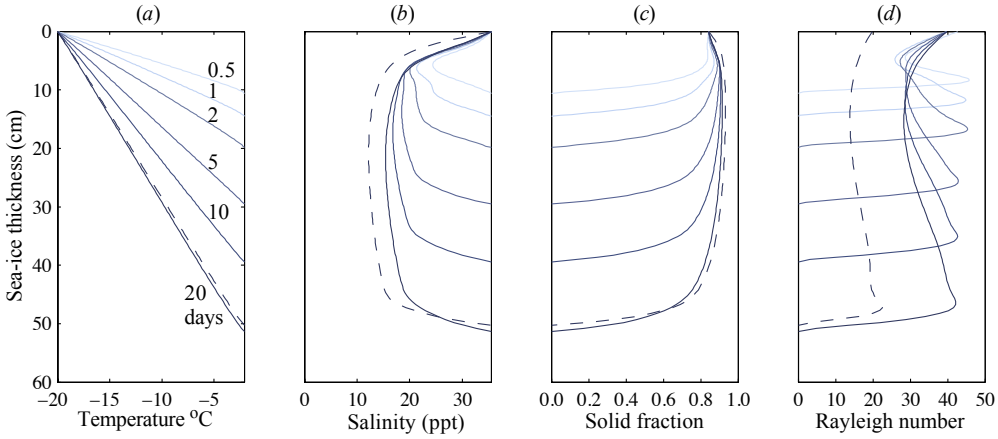

Figure 7.4: A series of profiles through the sea ice of (a) temperature, (b) salinity, (c) solid fraction and (d) local Rayleigh number. The calculations were performed for growth into a deep ocean with parameters $R_c = 40$ and $\alpha = 0.03$. The dashed curve gives profiles at the final time (20 days) at $R_c = 20$ and $\alpha = 0.03$.

cm for Wettlaufer *et al.* (1997*a*) and 39.5 cm for Notz (2005). Temperature is measured with thermistors and salinity by measuring with an optical refractometer small samples withdrawn from the tank using a hypodermic syringe. The resolution of the refractometer used to measure salinity is approximately 1 ppt so measurements near the onset of convection (when salinity begins to rise from the initial value) are difficult. We also mention more briefly the older experiments of Cox & Weeks (1975), which differ more significantly from the other two sets. The most significant difference for our purposes is the size of the tank, which is cylindrical, 14 cm in diameter and 69 cm deep.

To make a fair comparison with our model, it is important to be aware of experimental uncertainties. It is well known that heat fluxes from the laboratory affect ice growth and need to be minimized. In Wettlaufer *et al.* (1997*a*) the insulated tank was placed in a larger environment, held at roughly 4°C. In Notz (2005), the tank was placed inside a freezer whose temperature was controlled to lie between 0°C and −1.5°C. The other significant difference is that in Notz (2005) a wire harp was fixed inside the tank to measure the electrical impedance between pairs of wires to determine the local solid fraction, while in Wettlaufer *et al.* (1997*a*), measurements of volume expansion were used to determine the

average solid fraction in the sea ice. The wire harp may have artificially increased brine drainage. Other differences are either unspecified or thought to be minor, at least at moderate to late times. Only the initial growth is sensitive to the control protocol used to set the constant temperature of the cold plate.

To some extent we privilege the experiments of Wettlaufer *et al.* (1997*a*), not because they are necessarily better, but because they were conducted across a wider range of experimental conditions, which gives a more thorough test of our parameterization of gravity drainage.

Our approach complements the focus of Turner *et al.* (2013) and Griewank & Notz (2013) in that they each consider one laboratory experiment and one field experiment. Taken together with our study, they show the predictive capabilities of new parameterizations of gravity drainage. Whereas the previous two of these studies focus on salinity profiles take from the data of Notz (2005), we focus on measurements of the salinity of the ocean as a measure of the geophysically important salt flux from sea ice. Griewank & Notz (2013) acknowledge that the profiles they use have an uncertainty of around 5 ppt (and perhaps even more than this for high solid fractions), and our analysis suggests that they systematically underestimate the salinity of the ice. By comparison, we estimate that the uncertainty in the ocean salinities corresponds to an uncertainty of around 2 ppt in average ice salinity, but with a bias towards overestimation caused by very salty water ponding at the bottom of the tank. For example, Notz (2005) observed a difference between measurements of salinity at the bottom and middle of the tank (figure 7.5) that may indicate ponding, as well as some experimental scatter. By contrast, measurements of thickness are more repeatable. If the average ice salinity is calculated without accounting for the mass of salt contained in liquid that overflows due to the lower density of ice (data for the overflow is not always available to us, so we do not use it in our calculations), there is a further overestimation of ice salinity by around 2–3 ppt in our treatment of the experimental data.

There are inconsistencies between experiments carried out at nominally equivalent conditions. Our comparison (figure 7.5*a*) between the experiments suggests that the thickness of sea ice observed by Wettlaufer *et al.* (1997*a*) is less (by up to 15%) than that observed by Notz (2005) and Cox & Weeks (1975). There

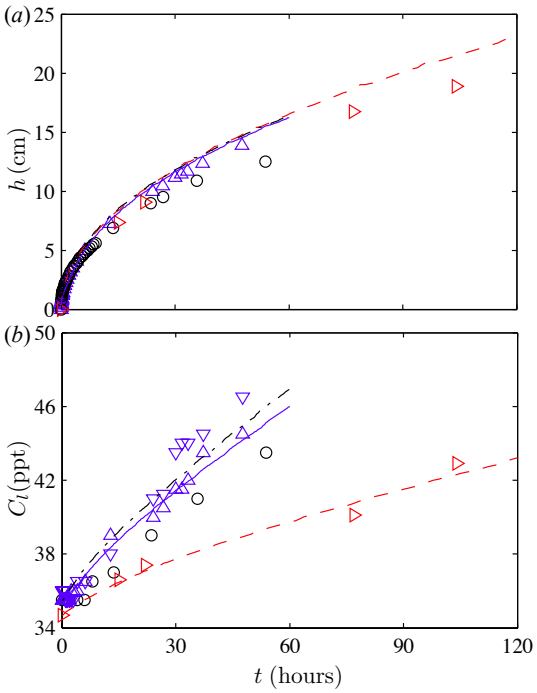

Figure 7.5: Experimental comparison in the case $T_B = -10°\mathrm{C}$: (a) sea-ice thickness and (b) ocean salinity measurements of Wettlaufer *et al.* (1997*a*) (black circles), Notz (2005) (blue triangles; in (b) upward triangles correspond to samples from the middle of the tank, downward from the bottom, where it appears some ponding of more saline water may occur) and Cox & Weeks (1975) (red, right-pointing triangles). For reference, we show predictions of our model at $R_c = 20$ and $\alpha = 0.03$. The different depths of the tank $H = 37.6$, $H = 39.5$ and $H = 69$ cm (dot–dashed, solid, dashed), corresponding to the experiments above, give negligible differences in sea-ice thickness but significant ones in ocean salinity.

is also almost certainly some differences in ocean salinity (figure 7.5b), since the different depths of the tank do not explain all the discrepancies between measurements. The experimental inconsistencies and biases in processing data must be remembered when comparing our models and choice of tuning parameters. These uncertainties should be addressed in future experiments.

7.3.2 Typical results for a fixed cold-plate temperature

We consider a constant cold-plate temperature of $T_B = -20°\text{C}$ and initial salinity 35.5 ppt, and compare our model results to the experimental observations of Wettlaufer *et al.* (1997a). The relatively cold temperature of the cold plate means that heat gains from the laboratory are somewhat less important.

We show results for a range of tuning parameters and discuss sensitivity to them below. Our model predicts the approximately diffusive growth of sea ice over time reasonably well (figure 7.6a). Our model also reproduces the evolution of the ocean salinity well (figure 7.6b) for parameters around $R_c = 40$, $\alpha = 0.03$. However, it predicts an onset time that is somewhat too early.

The temperature of the ocean (figure 7.6c) has been difficult to model across all the experiments. This discrepancy may arise owing to problems in our model, such as the assumption that the ocean is well mixed, or experimental problems such as heat gains from the laboratory. The latter is suggested by the fact that the amount of superheat $T_l - T_L(C_l)$ increases after the first 10 hours, while our model predicts that it remains roughly steady.

7.3.3 Parameterization of convection and sensitivity to tuning parameters

In our parameterization of convection, a smaller value of R_c (which corresponds to a smaller critical thickness of ice for the onset of convection) means that convection begins earlier (figure 7.6b). However, R_c also determines the late-time evolution of the salinity field. A smaller R_c means that that ice can desalinate more (corresponding to a higher solid fraction and a smaller permeability) before convection shuts down, leading to a more saline ocean.

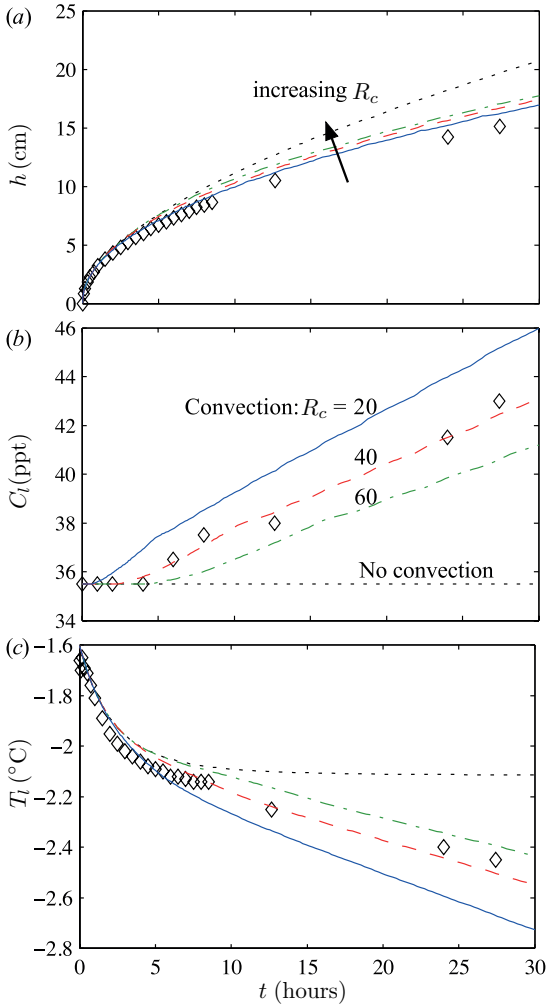

Figure 7.6: Results of our model at $T_B = -20°\mathrm{C}$: (a) sea-ice thickness, and (b) salinity and (c) temperature of the ocean. Open symbols are experimental measurements from Wettlaufer *et al.* (1997*a*). Calculations are run for the case of no convection ($R_c = \infty$) and for three different values of R_c (indicated in b), at fixed $\alpha = 0.03$. Experimental results for salinity of the ocean after 30 hours agree well with $R_c \approx 40$.

The sea-ice thickness predicted by our model without convection is consistently greater than that measured in experiments (figure 7.6*a*). All the parameterizations that include convection do a better job of describing the thickness, and can do so within the range of experimental uncertainty. However, the thickness appears relatively insensitive to the value of R_c because, although the thermal properties of ice depend significantly on salinity, the reduced thermal conductivity of more saline ice is almost balanced out by the lower latent heat release. The trend towards slightly thicker ice when R_c is larger is consistent with the fact that more saline ice is slightly thicker, as discussed in section 8.4.

More systematically, in figure 7.7 we consider how the predicted salinity of the ocean and sea-ice thickness after 30 hours depend on the tuning parameters. Hitherto we have considered two independent tuning parameters. However, figure 7.7*c*,*d* shows that the dependence on α is very weak in the range suggested by idealized studies, so we fix $\alpha = 0.03$, a typical value in these studies (*cf.* figure 6.3 and note that in this chapter we use α in place of $W(\Omega)$ and $\Omega \approx 10$). There is some early-time sensitivity to α, but very little sensitivity several hours after the onset of convection because of the following negative feedback. A greater initial desalination increases the solid fraction, thereby reducing the Rayleigh number and so reducing later desalination. Figure 7.7*a*,*b* shows the experimental uncertainty in ocean salinity corresponds (at least in this parameter range) to a large uncertainty in R_c. We suggest using $R_c = 40$ for the Wettlaufer *et al.* (1997*a*) experiments, although note that a range $20 < R_c < 45$ would be reasonable.

Our parameterization allows convection to be confined to a lower layer of ice. The detailed behaviour is sensitive to the precise details of the parameterization – using the approach described in section 7.2.3 leads to cycles of full-depth and confined convection, at least for the early part of ice growth in a confined tank (figure 7.8). The basic physical mechanism driving these cycles is as follows: a shift to confined convection reduces the salt flux from the ice, leading to a slower increase in solid fraction and slower decrease in permeability. However, the growth rate is almost unchanged, so the local Rayleigh number can increase sufficiently to allow full-depth convection. The more rapid desalination then decreases the permeability faster, leading to convection being confined again. This behaviour is

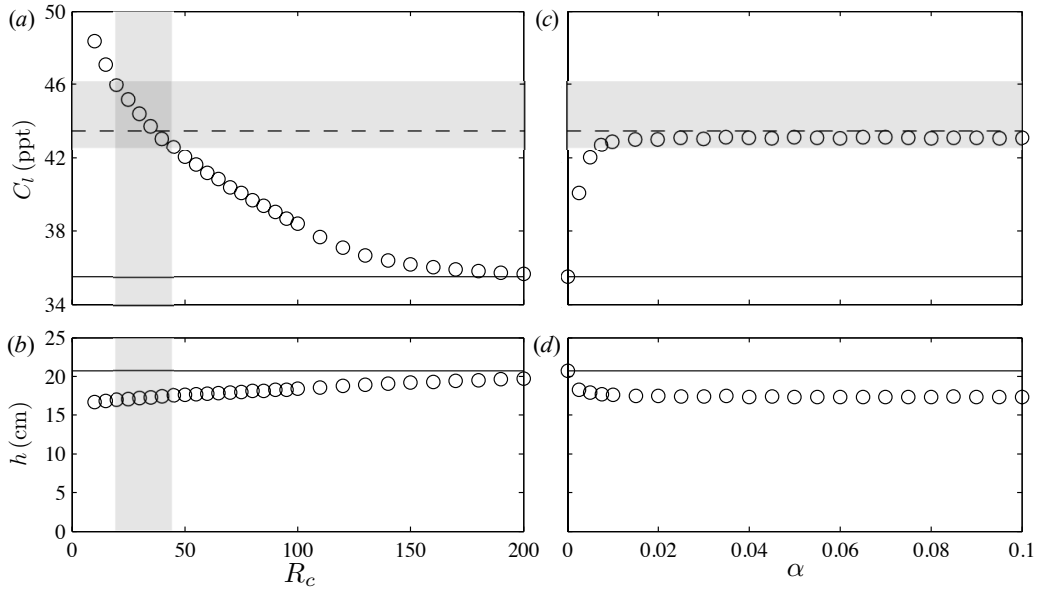

Figure 7.7: Model sensitivity to tuning parameters at $T_B = -20°\mathrm{C}$ (circles). Predictions of the ocean salinity (a, c) and sea-ice thickness (b, d) at $t = 30$ hours. We show variation with R_c at $\alpha = 0.03$ in (a, b), and variation with α at $R_c = 40$ (c, d). The dashed, horizontal line shows the experimentally observed ocean salinity. The horizontal shaded region gives a rough (high) estimate of the uncertainty, accounting for the ± 1 ppt resolution of the refractometer used and the $+1.5$ ppt bias towards underestimating the ocean salinity associated with the ponding and overflow discussed in section 7.3.1. The vertical shaded region shows the consequent uncertainty in choice of R_c. The solid, horizontal lines show the case of no convection.

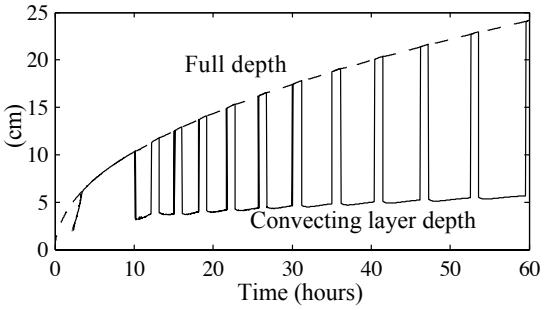

Figure 7.8: The depth of the convecting layer at the conditions described in figure 7.6 for parameters $R_c = 40$, $\alpha = 0.03$.

quite common in our model and indeed the signature of these oscillations is shown in the Ra-profiles shown in figure 7.4*d* for a deep tank with the Rayleigh number at the top of the tank $Ra(0)$ switching between being just supercritical and just subcritical. This switching allows the upper regions of ice to desalinate slowly (*cf.* figure 7.4*c*) within our single parameterization of gravity drainage, which may have a similar effect to the additional 'slow mode of gravity drainage' of Turner *et al.* (2013), discussed in section 8.1.3. We note in passing that oscillations in gravity drainage have previously been reported in experiments; for instance Eide & Martin (1975) report oscillations with a period of roughly an hour in 10 cm-thick ice.

7.3.4 Model predictions with fixed chill

The usefulness of our model depends not on its ability to predict a single experiment. Arguably, it is not surprising that any reasonable model could achieve this by adjusting tuning parameters. Therefore, we run our model with the same tuning parameters $R_c = 40$, $\alpha = 0.03$ suggested by the cold plate temperature $T_B = -20°\mathrm{C}$ over a range of T_B.

There is a tendency to overestimate sea-ice thickness in our model, which occurs to greater extent at warmer T_B (figure 7.9*a*). This overestimation may arise from the fact that our expression for the thermal conductivity of ice (7.8), which uses the arithmetic mean, applies to lamellae orientated parallel to the temperature gradient, and is an upper bound for arbitrary crystal structure (Batchelor,

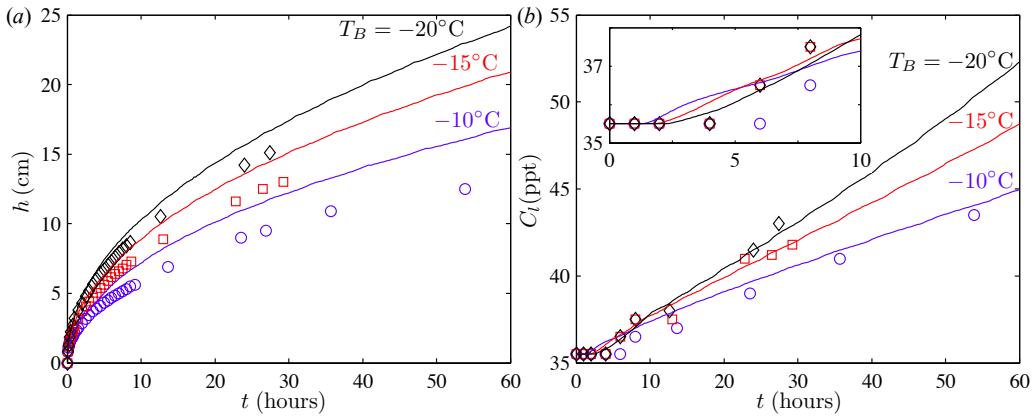

Figure 7.9: Model predictions of (a) sea-ice thickness and (b) ocean salinity at $R_c = 40$ and $\alpha = 0.03$ compared to the experiments of Wettlaufer *et al.* (1997a) for $T_B = -20°\mathrm{C}$ (diamonds), $T_B = -15°\mathrm{C}$ (squares) and $T_B = -10°\mathrm{C}$ (circles). The inset in (b) shows the onset of convection.

1974). However, calculations in which the harmonic, rather than arithmetic, mean are used suggest this effect is no more pronounced at warmer T_B. The overestimation seems more likely to result from the heat gains from the laboratory discussed in section 7.3.1.

In terms of ocean salinity, the onset of convection is poorly described by our model. According to our model, the onset is earliest in the case $T_B = -10°\mathrm{C}$, which is the reverse of the experimental observations (figure 7.9b, inset). Given that predictions of sea-ice thickness for early times are reasonably accurate, this discrepancy is most likely to be connected to difficulties in calculating the permeability of mushy layers. There appears to be a systematic tendency to overestimate the permeability of relatively porous ice ($T_B = -10°\mathrm{C}$) but underestimate the permeability of less porous ice ($T_B = -20°\mathrm{C}$). We return to this question in section 7.4. Nevertheless, our model describes the evolution of both the sea-ice thickness and salinity of the ocean across all three experiments in a reasonably successful fashion.

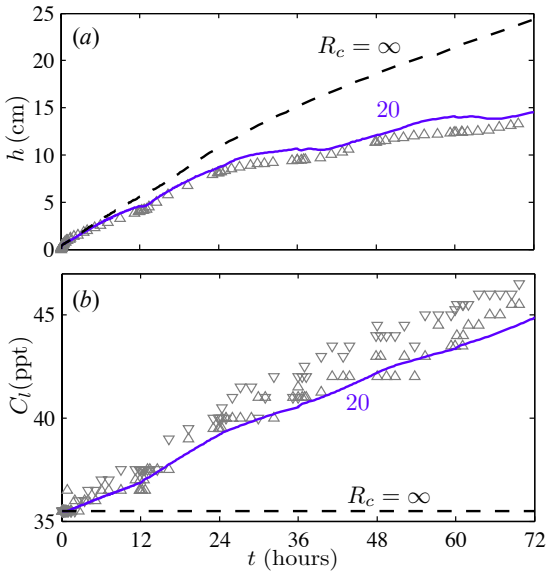

Figure 7.10: Experiment in which T_B is switched between -5°C to -10°C every twelve hours. Symbols are as in figure 7.5. The blue curve shows $R_c = 20$ and the black dashed curve shows $R_c = \infty$ (our model without convection).

7.3.5 Model predictions with variable chill

We compare our model to an experiment by Notz (2005) in which the cold plate temperature was switched every twelve hours, a timescale chosen to mimic a diurnal cycle. We use tuning parameters $R_c = 20$, $\alpha = 0.03$ suggested by the equivalent experiment at fixed cold-plate temperature (*cf.* figure 7.5, and note that the different R_c is associated with the experimental inconsistency discussed in section 7.3.1). Our model does a very good job of reproducing the observed sea-ice thickness and desalination of the ice (figure 7.10). Although these step changes in temperature are somewhat artificial, very similar results were obtained in our model with a sinusoidally varying cold-plate temperature.

7.3.6 Conclusions

Calculations of sea-ice thickness are sensitive to knowledge of the thermal properties of sea ice. In our calculations, we have made a number of approximations, such as ignoring the variation in these properties with temperature. Nevertheless, we are able to predict sea-ice growth within experimental uncertainty (albeit

with a bias towards over-predicting growth). Crucially, a single choice of tuning parameter can successfully describe the evolution of the salinity of the ocean in a range of experiments at different conditions. Therefore, our parameterization represents promising progress in the accurate, time-dependent, prediction of salt fluxes in sea-ice models.

However, there are differences between experiments (which we do not fully understand) and biases in processing experimental data that would lead to different (lower) choices of critical Rayleigh number compared to those based on the measured ocean salinity in the experiments of Wettlaufer *et al.* (1997*a*) on which we have focused. Further experiments are required to resolve the final choice.

7.4 Porosity–permeability relationship

Our dynamic-salinity model of sea ice applies to a much wider class of problems than simply those growing sea ice from saltwater with a salinity of about 35 ppt, because it is derived from fundamental physics and was not particularly tuned to sea ice (with the exception of the tuning parameters R_c and α, which we do not use in this section because here we only consider behaviour before the onset of convection). Thus we have used it to investigate the full set of experiments considered in Wettlaufer *et al.* (1997*a*), which were conducted at different initial saltwater salinities from 20 to 140 ppt. These lead to the formation of ice with different porosities, allowing an indirect study of the relationship between porosity and permeability.

The relationship between the porosity and permeability of a reactive porous medium, such as sea ice, is an intrinsically difficult problem, because direct measurements alter the structure of the medium. Some recent progress, reviewed by Golden *et al.* (2007), has been made by taking essentially microstructural models that have some form of *local* permeability and using them to establish a *bulk* permeability for a layer of sea ice (*e.g.* Petrich *et al.*, 2006; Zhu *et al.*, 2006).

Here, we extend a suggestion of Wettlaufer *et al.* (1997*a*, 2000): the hypothesis of a constant critical Rayleigh number can be used to collapse data from the full range of experiments to a single curve and this curve used to infer the (bulk) permeability. We extend this suggestion by inferring a consistent local

permeability.

Our procedure is as follows. We take the experimental measurements in Wettlaufer *et al.* (1997*a*) of ocean salinity as a function of sea-ice thickness and use them to calculate a critical thickness for the onset of convection (at which the ocean salinity starts to increase from its initial value). We then use our model, forced at the relevant experimental conditions, to calculate the growth of the mushy layer until the experimental critical thickness is reached. We calculate the local Rayleigh number from equation (7.10) at the critical thickness assuming a given relationship for the local permeability $K_l(\phi) = (1-\phi)^b$ in equation (7.11). We then plot the maximum value of the Rayleigh number $Ra_{\max}$ against the calculated mean solid fraction $\overline{\phi}$. We look for a horizontal line of best fit, because a constant $Ra_{\max}$ with $\overline{\phi}$ corresponds to the hypothesis of a constant critical Rayleigh number.

In figure 7.11*a*, we show that local permeability $K_l(\phi) = (1-\phi)^3$ does not appear consistent with a constant critical Rayleigh number. The cubic relationship seems to overestimate the permeability for low solid fraction and underestimate it for high solid fraction, consistent with the pattern observed in figure 7.9 and also the measurements of Eicken *et al.* (2004). A better choice, shown in figure 7.11*b*, is $K_l(\phi) = (1-\phi)^2$, which successfully removes most of the trend evident in figure 7.11*a* and is consistent with the hypothesis of a constant critical Rayleigh number. It also corrects the problems with predicting onset noted in figure 7.9*b* and improves predictions throughout the range of times considered.

It is important to note that, in the interpretation of experiments in figure 7.12, the hypothesis of a constant critical bulk Rayleigh number is nevertheless consistent with a bulk permeability that varies cubically with mean porosity, *i.e.* $\overline{K} \propto (1-\overline{\phi})^3$, a relationship commonly suggested following Freitag (1999). This suggests that caution should be used when calculating a local Rayleigh number using formulae appropriate to the bulk permeability. A local permeability $K_l(\phi) = (1-\phi)^2$ corresponds to a microstructural model of cylindrical tubes orientated parallel to the temperature gradient (*e.g.* Phillips, 1991), which is plausible for sea ice. Coupled with the promising results from our model, this leads us to propose investigating this relationship in future when calculating local Rayleigh numbers.

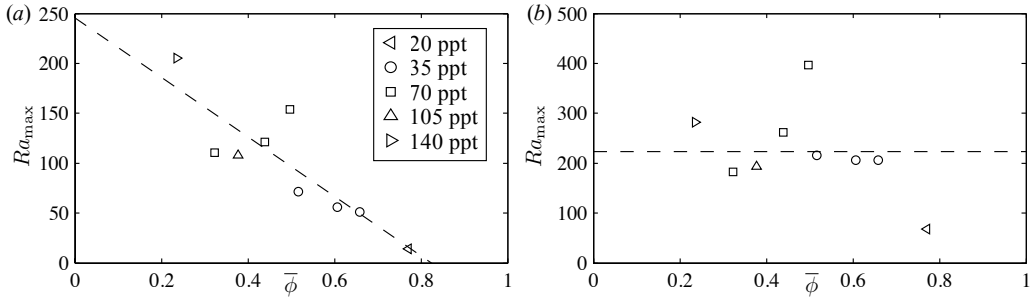

Figure 7.11: Maximum Rayleigh number $Ra_{\max}$ against mean solid fraction $\overline{\phi}$ for different initial salinities C_0 (see legend) calculated using our model on the experiments of Wettlaufer *et al.* (1997*a*) using the methodology discussed in the text. We display the cases: (*a*) $K_l(\phi) = (1-\phi)^3$ and (*b*) $K_l(\phi) = (1-\phi)^2$. The dashed lines represent a linear and constant fit respectively. Note that the different scale on the $Ra_{\max}$ has no physical significance since any change could be incorporated in the reference permeability K_0 in equation (7.11).

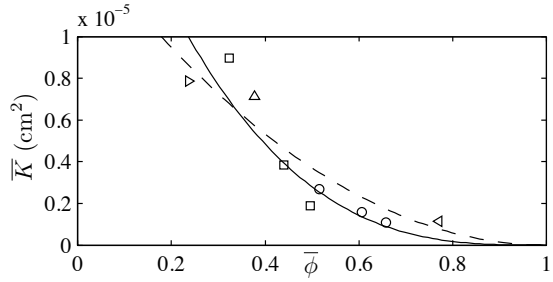

Figure 7.12: Bulk permeability inferred from the experiments of Wettlaufer *et al.* (1997*a*) using equation (7.10) with a single bulk permeability $\overline{K}$ under the hypothesis that the onset of convection is determined by a critical bulk Rayleigh number $R_c = 40$. The legend is as in figure 7.11. The solid curve is a best fit cubic $\overline{K} = 2.24 \times 10^{-5}(1-\overline{\phi})^3$, which is perhaps a slightly better fit than the best fit quadratic $\overline{K} = 1.48 \times 10^{-5}(1-\overline{\phi})^2$, (*cf.* figure 7*b* in Wettlaufer *et al.*, 2000, for a complementary approach).

7.5 Conclusions

Our new dynamic-salinity sea-ice model contains a parameterization of gravity drainage derived from fundamental physical principles. Thus it can account for important dynamical feedbacks that regulate the desalination of sea ice, such as the relationship between ice salinity, porosity, permeability and the desalination rate (which we use a local Rayleigh number to represent), as well as varying external forcing from the atmosphere and ocean.

Our simple parameterization benefits from being a single governing equation for the vertical transport of heat and salt caused by convection, with only one dynamically important tuning parameter, a critical Rayleigh number R_c. We have expressed our parameterization in terms of the underlying partial differential equations, rather than a particular numerical scheme, such that it can be implemented readily in climate models using any desired numerical method.

As well as being physically based (in common with some of the other new generation of dynamic-salinity sea-ice models), our model has been thoroughly tested against a wide range of published laboratory experiments. Our success in using a single choice of tuning parameter to predict the salt fluxes across a change of experimentally imposed external conditions leads us to conclude that our parameterization represents the correct physics. There are some inconsistencies and biases between experiments at the same nominal conditions, that lead to some uncertainty in the final choice of tuning parameter R_c. Further laboratory experiments (and perhaps field observations) are needed to resolve this choice.

We discuss the implications of our parameterization for climate modellers in chapter 8 by analysing the behaviour of a fixed-salinity model in comparison with the dynamic-salinity model developed in this chapter.

7.A Appendix: Numerical method

7.A.1 Non-dimensionalization, rescaling and discretization

We non-dimensionalize the governing equations and boundary conditions for numerical convenience. We define the dimensionless temperature of the ice and ocean

$$\theta = \frac{T - T_L(C_0)}{T_L(C_0) - T_B}, \qquad \theta_l = \frac{T_l - T_L(C_0)}{T_L(C_0) - T_B}, \tag{7.20}$$

respectively, where C_0 is the initial salinity of the ocean and T_B is the initial temperature of the cold plate. There is a choice in how to non-dimensionalize the bulk salinity of the ice and ocean. In order to avoid inverting the liquidus relationship $T = T_L(C)$ at various points it is more convenient to choose

$$\theta_b = \frac{T_L(S) - T_L(C_0)}{T_L(C_0) - T_B}, \qquad \theta_{cl} = \frac{T_L(C_l) - T_L(C_0)}{T_L(C_0) - T_B}, \tag{7.21}$$

for the bulk salinity and ocean salinity respectively.

Sea ice occupies the region $0 \leq z \leq h(t)$. It is moderately difficult to accommodate a time-dependent domain numerically, although this is sometimes done in so-called 'enthalpy-methods' (*e.g.* Oertling & Watts, 2004; Notz & Worster, 2006), including, for example, version 4 of CICE (Hunke & Lipscomb, 2008). In this chapter, we map the sea ice to $[0, 1]$ which avoids the need to re-map a numerical grid, and the additional nonlinearity in the equations is not especially costly because the equations are already nonlinear. It has the computational advantage that the temperature is approximately steady in these changed coordinates. Rather than directly calculating $h(t)$, we calculate $h^2(t)$ to cope better with the initial growth. In particular, we map the mushy layer to $[0, 1]$ by introducing the change of variables $(t, z) \to (\tau, \zeta)$, where

$$\tau(t, z) = t, \qquad \zeta(t, z) = z/y^{1/2}(t), \qquad y = h^2. \tag{7.22}$$

In these mapped coordinates

$$\frac{\partial}{\partial t} = \frac{\partial}{\partial \tau} - \zeta \frac{\dot{y}}{2y} \frac{\partial}{\partial \zeta}, \qquad \frac{\partial}{\partial z} = \frac{1}{y^{1/2}} \frac{\partial}{\partial \zeta}. \tag{7.23}$$

The governing equations (7.3, 7.4) give a nonlinear diffusion equation for the dimensionless temperature $\theta(\tau, \zeta)$ and an advection equation for dimensionless bulk salinity $\theta_b(\tau, \zeta)$ on $0 \leq \zeta \leq 1$. We discretize this domain into I equally spaced intervals of length $\Delta\zeta = 1/I$ and label the end-points

$$\zeta_j = j\Delta\zeta : j = 0, 1, ..., I.$$

Throughout, we use second-order estimates in space, appropriate to the order of the heat equation.

We index time steps $\Delta\tau$ with n. For example, if $y^n = y(\tau)$, then $y(\tau + \Delta\tau) = y^{n+1}$. Similarly, we write $\theta_j^n = \theta(\tau, \zeta_j)$ and likewise for the other variables. However, unlike $\Delta\zeta$, we do not fix $\Delta\tau$ but allow it to vary over the course of the integration.

7.A.2 Predictor–corrector routine for non-linear diffusion equation

The heat equation (7.3) implies that the temperature $\theta(\tau, \zeta)$ satisfies

$$c\frac{\partial\theta}{\partial\tau} + \left[-c\frac{\zeta\dot{y}}{2y} + d\frac{w}{y^{1/2}}\right]\frac{\partial\theta}{\partial\zeta} = \frac{1}{y}\frac{\partial}{\partial\zeta}\left(k\frac{\partial\theta}{\partial\zeta}\right), \tag{7.24}$$

where, to avoid multiple subscripts, we replace c_i by c, c_w by d and k_i by k. If we set $w = 0$, this equation reduces to an equivalent equation in Kerr *et al.* (1990). Therefore, we use the same type of numerical method: a predictor–corrector generalization of the second-order in space Crank-Nicholson routine (Ames, 1977) solves the heat equation, and a second-order Runge–Kutta routine solves the ordinary differential equations governing the interface location (7.15) and the temperature of the ocean (7.17). Our approach retains the stability advantages of semi-implicit schemes while retaining a linear tridiagonal system that can be readily solved.

For the predictor step, we estimate all quantities at time n, except for the highest derivative $\frac{\partial}{\partial\zeta}\left(k_m\frac{\partial\theta}{\partial\zeta}\right)$ in which we evaluate k at time n, but θ at time $n + \frac{1}{2}$. Using a forward time step to evaluate $\frac{\partial\theta}{\partial\tau}$, we obtain a linear system of

equations for $\theta^{n+1/2}$ at the interior points $j = 1, 2, ..., I-1$

$$y^n c_j^n \left(\frac{\theta_j^{n+1/2} - \theta_j^n}{\Delta\tau/2} \right) + \left[-c_j^n \frac{\zeta_j \dot{y}^n}{2} + d_j^n w_j^n (y^n)^{1/2} \right] \left(\frac{\theta_{j+1}^n - \theta_{j-1}^n}{2\Delta\zeta} \right)$$
$$= \frac{1}{2\Delta\zeta^2} \left[\left(k_{j+1}^n + k_j^n \right) \theta_{j+1}^{n+1/2} - \left(k_{j+1}^n + 2k_j^n + k_{j-1}^n \right) \theta_j^{n+1/2} \right.$$
$$\left. + \left(k_j^n + k_{j-1}^n \right) \theta_{j-1}^{n+1/2} \right] \tag{7.25}$$

We apply the fixed-temperature boundary conditions on θ by setting $\theta_0^{n+1/2}$ and $\theta_I^{n+1/2}$. We then use the Thomas Algorithm (Thomas, 1949) to solve the resulting tridiagonal system of linear equations to determine an estimate for the temperature field at the half time step.

For the corrector step, we estimate all quantities at time $n + 1/2$, averaging estimates for the highest derivatives at time n and time $n + 1$. This gives a linear system of equations for θ^{n+1} at the interior points $j = 1, 2, ..., I-1$

$$y^{n+1/2} c_j^{n+1/2} \left(\frac{\theta_j^{n+1} - \theta_j^n}{\Delta\tau} \right)$$
$$+ \left[-c_j^{n+1/2} \frac{\zeta_j \dot{y}^{n+1/2}}{2} + d_j^{n+1/2} w_j^{n+1/2} (y^{n+1/2})^{1/2} \right] \left(\frac{\theta_{j+1}^{n+1/2} - \theta_{j-1}^{n+1/2}}{2\Delta\zeta} \right)$$
$$= \frac{1}{4\Delta\zeta^2} \left[\left(k_{j+1}^{n+1/2} + k_j^{n+1/2} \right) \left(\theta_{j+1}^{n+1} + \theta_{j+1}^n \right) \right.$$
$$- \left(k_{j+1}^{n+1/2} + 2k_j^{n+1/2} + k_{j-1}^{n+1/2} \right) \left(\theta_j^{n+1} + \theta_j^n \right)$$
$$\left. + \left(k_j^{n+1/2} + k_{j-1}^{n+1/2} \right) \left(\theta_{j-1}^{n+1} + \theta_{j-1}^n \right) \right] \tag{7.26}$$

As before, we apply the fixed-temperature boundary conditions and solve the tridiagonal system to determine the temperature at the next time step θ^{n+1}.

7.A.3 Advection equation for bulk salinity

The salt equation (7.4) implies that $\theta_b(\tau, \zeta)$ satisfies

$$\frac{\partial \theta_b}{\partial \tau} = \frac{\zeta \dot{y}}{2y} - r \frac{w}{y^{1/2}} \frac{\partial \theta}{\partial \zeta}, \tag{7.27}$$

where $r = C_L'(\theta)/C_L'(\theta_b)$ and $'$ denotes a derivative with respect to the argument. Equation (7.27) is hyperbolic and susceptible to spurious oscillations. These can be avoided by solving the case $w = 0$ using interpolation (this accounts for the frame advection $\zeta\dot{y}/2y$ in equation 7.27) and then central differencing to treat the convective part ($w \neq 0$). In particular, we find

$$(\theta_b)_j^{n+1/2} = (\theta_b)_{j*}^n - r_j^n \frac{\Delta t}{2} \frac{w_j^n}{(y^n)^{1/2}} \left(\frac{\theta_{j+1}^n - \theta_{j-1}^n}{2\Delta\zeta} \right), \tag{7.28}$$

and

$$(\theta_b)_j^{n+1} = (\theta_b)_{j*}^n - r_j^{n+1/2} \Delta t \frac{w_j^{n+1/2}}{(y^{n+1/2})^{1/2}} \left(\frac{\theta_{j+1}^{n+1/2} - \theta_{j-1}^{n+1/2}}{2\Delta\zeta} \right), \tag{7.29}$$

where $(\theta_b)_{j*}^n$ is obtained by linearly interpolating the solution at time n to find the value at $\zeta_{j*} = \zeta_j(y^{n+1}/y^n)$ at the full time step and similarly at the half time step. Linear interpolation is equivalent to a central finite-difference approach at leading order, but avoids the spurious oscillations introduced by using central differencing to solve equations involving frame advection (the other advective term is coupled more tightly to the thermal equation, which includes diffusion, so this can be integrated as we have outlined above).

7.A.4 Boundary conditions

We use equations (7.15, 7.17) to determine the dimensionless thickness of sea ice and temperature of the ocean

$$\dot{y} = 2y^{1/2}\, w|_{\zeta=1} + \frac{2\,\partial\theta/\partial\zeta|_{\zeta=1^-} - 2y^{1/2} Nu\,(\theta_l - \theta_{cl})^{4/3}}{\theta_l - \theta_{cl} + \mathcal{S}\,\phi|_{\zeta=1^-}}, \tag{7.30}$$

$$\left(1 - y^{1/2}\right)\dot{\theta}_l = -Nu\,(\theta_l - \theta_{cl})^{4/3}, \tag{7.31}$$

where

$$Nu = \left(2^{4/3}\lambda\right)\left(\frac{\alpha_T g c_l H^3 \Delta T}{k_l \nu}\right)^{1/3}, \qquad \mathcal{S} = \frac{L}{c_l \Delta T}. \tag{7.32}$$

In order to maintain second-order accuracy in $\Delta\zeta$, we use the estimate

$$\left.\frac{\partial\theta}{\partial\zeta}\right|_{\zeta=1^-} = \frac{3\theta_I - 4\theta_{I-1} + \theta_{I-2}}{2\Delta\zeta}. \tag{7.33}$$

Our scheme to solve these ordinary differential equations is analogous to the second-order Runge–Kutta method and was chosen for compatibility with the predictor–corrector routine for the heat equation. We firstly estimate all quantities at time n to forward time step to $n+1/2$. We secondly estimate all quantities at time $n+1/2$. This estimation requires the output from the predictor step discussed above. We then perform a full time step forward from time step n to $n+1$ to obtain a second-order estimate for y and θ_l at time $n+1$.

We could have used a similar method to calculate the solute flux and hence the evolution of ocean salinity θ_{cl}. However, we preferred explicitly to conserve salt globally and we used quadrature to calculate the salt flux to the ocean. To maintain second-order accuracy, we used a modified Simpson's rule when evaluating the integral.

7.A.5 Parameterization of convection

At a given time, θ, θ_b are used to calculate the solid fraction ϕ. Then, using equation (7.11), the dimensionless harmonic mean permeability

$$K(\zeta) = \left[\frac{1}{1-\zeta}\int_\zeta^1 \frac{1}{K_l(\phi(\zeta'))}\,d\zeta'\right]^{-1}. \tag{7.34}$$

is calculated using a modified version of Simpson's rule. Finally, the local Rayleigh number given in equation (7.10)

$$Ra(\zeta) = Ra_0\frac{C_L(\theta(\zeta)) - C_L(\theta_l)}{\Delta C_0}y^{1/2}(1-\zeta)K(\zeta), \tag{7.35}$$

where

$$Ra_0 = c_l g\beta\Delta C_0 H K_0/k_l\nu, \qquad \Delta C_0 = C_L(\theta(0)) - C_L(\theta_l) \tag{7.36}$$

evaluated at $t=0$. The maximum value of $Ra(\zeta)$ is found on the discretized grid $Ra_i = Ra(\zeta_i)$. If $\max Ra_i < R_c$, the whole mushy layer is subcritical and so there

is no convection.

In order to retain second-order spatial accuracy in calculating w, we proceed as follows. If $Ra_{i=0} = 0$, the whole layer is supercritical and $\zeta_c = 0$. Otherwise, we find the first point i such that $Ra_i \geq R_c$, fit a quadratic to this point and its nearest neighbours (these three points uniquely specify the quadratic, no regression is required) and use the quadratic formula to determine a second-order estimate for the root $Ra(\zeta_c) = R_c$. Similarly, we fit a quadratic to the discretized Rayleigh number about the maximum to estimate $R_{max} = \max Ra(\zeta)$ to second order, except in the case of an end-point maximum, in which this is unnecessary.

7.A.6 Initial conditions

The initial conditions depend on the situation modelled and the following conditions are appropriate to the laboratory experiments in section 7.3. Initially the sea-ice thickness is zero and, before convection begins, the bulk salinity of the ice has the same value as the initial salinity of the ocean so

$$h(t) = 0, \quad S(t,z) = C_0, \quad C_l(t) = C_0, \quad T_l(t) = T_0 \qquad (t = 0), \tag{7.37}$$

where the initial salinity C_0 and temperature T_0 of the ocean must be specified.

While the initial temperature profile $T(0,z)$ appears arbitrary, it can be uniquely specified such that $h \sim At^{1/2}$ as $t \to 0$, which is exact diffusive growth, for some constant A to be determined. Exact diffusive growth corresponds to the initial temperature profile being steady in scaled coordinates ζ. Initially there is no convection, as observed by Wettlaufer *et al.* (1997*a*), since the initial Rayleigh number will be zero as the sea-ice thickness is zero. Then, asymptotically approximating the boundary condition (7.15) to determine the initial growth rate in terms of the initial temperature profile, the heat equation (7.3) becomes an ordinary differential equation, which we solve numerically using a shooting method and Runge–Kutta routine to determine the initial temperature profile uniquely.

7.A.7 Testing and error control

The numerical method was tested against known solutions for the linear and nonlinear heat equation without convection, and tested for resolution sensitivity. In all our calculations for the graphs in this chapter we used 100 vertical grid points. However, our model can certainly be run with fewer grid points. For example, in calculations for figure 7.4, after 20 days of growth into a deep ocean the use of 40 grid points gives a difference of 0.7% in the change in average sea-ice salinity, 10 gives a difference of 5% in the change in average sea-ice salinity, and 5 gives a difference of 16% in the change in average sea-ice salinity. The differences between sea-ice thickness were small (at most about 2% after 20 days, although higher for earlier times). This suggests that it is practical to use our parameterization in climate models with 5 or 10 grid points, although it may be necessary to retune parameters for the smaller number of grid points. We did not use a fixed time step but instead controlled errors in time stepping by both imposing a Courant condition and also by calculating the difference between two time steps and a single time step of double the length. This gives an estimate of the error, which we used to adjust the time step such that the error remained below some specified tolerance. For example, in the calculation with 5 grid points discussed above, the average time step was about 30 minutes. The variable time step speeds up the integration as much as possible while controlling the error.

Chapter 8

Implications for climate models

The content of this chapter has been submitted to the Journal of Geophysical Research (Rees Jones & Worster, 2013c).

8.1 Introduction

8.1.1 Mechanisms for interaction with the climate

In this chapter, we focus on two kinds of physical mechanism, discussed in more detail in section 2.1.2, through which our new parameterization of gravity drainage might affect a climate model in which it was included. Firstly, there are implications for the thermal properties of sea ice. Although only a few meters thick, sea ice reflects a higher proportion of solar radiation than open water, insulates the polar oceans, and stores latent heat (reviewed in Weeks, 2010). Secondly, there are implications for the transport of salt in the polar regions. The seasonal desalination of sea ice is a crucial salt flux for the polar oceans, comparable to the (negative) salt fluxes from rivers and ice-sheet melting, and drives vertical mixing of the upper layer of the ocean. Indeed, the representation of salt fluxes is known to significantly affect the salinity structure of the ocean in climate models (Vancoppenolle *et al.*, 2005, 2009*b*).

In full, coupled climate models there are likely to be additional effects. For example, the mechanical properties of sea ice depend on its salinity, so our parameterization could affect the advective transport of sea ice due to wind stresses, as

well as mechanisms like ridging, where the ice is thickened by collisions between ice floes. Furthermore, in principle, the parameterized convective upwelling velocity calculated in our model could also be used to calculate the transport of nutrients and trace gases in climate models (Vancoppenolle *et al.*, 2010). Such processes are increasingly important in view of the transition from purely physical models to 'Earth system' models that also incorporate biological and chemical elements, such as in the Community Earth System Model (Hurrell *et al.*, 2013). However, these effects are rather more indirect that those concerning thermal properties and salt fluxes that we focus on in this chapter.

8.1.2 Comparison of model formulation with CICE

Having developed a functioning dynamic-salinity sea-ice model in chapter 7, we now assess the implications for climate models by comparing it to CICE: The Los Alamos Sea Ice Model (version 4.1, Hunke & Lipscomb, 2008) as an example of a fixed-salinity model.

The thermodynamic modelling in Bitz & Lipscomb (1999), incorporated into CICE, is approximately equivalent to that derived from mushy-layer theory. In particular, Feltham *et al.* (2006) show that if the liquidus relationship is taken to be linear $C_L(T) = -T/m$, then equations (7.6, 7.8) for the thermal properties of a mushy layer simplify to

$$c_i(T,S) = c_s + mL\frac{S}{T^2}, \tag{8.1}$$

$$k_i(T,S) = k_s + m\,(k_s - k_l)\,\frac{S}{T}, \tag{8.2}$$

which are exactly the same expressions used in CICE, except for the small difference that $m\,(k_s - k_l) \approx 0.0009$ W/cm/ppt is replaced by a constant 0.0013 W/cm/ppt. In the case of CICE, k_i artificially drops to zero at the ice–ocean interface where the temperature $T_O \approx -2°\mathrm{C}$ at bulk salinity $S = k_s(-T_O)/0.0013 \approx 33$ ppt. By contrast, in our calculations k_i is always greater than the thermal conductivity of brine and so never drops to zero.

In our comparisons, we use equations (8.1, 8.2) with the constant 0.0013 W/cm/ppt as mentioned above and parameter values taken from the CICE doc-

umentation for consistency. The most significant difference is that the default option in CICE for the thermal conductivity of pure ice is 0.0203 W/cm/deg, which is lower than most estimates, including that used in table 7.1 (*cf.* Pringle *et al.*, 2007) – which has the effect of reducing ice growth slightly. In all other respects (numerical method, treatment of the ocean, including the relationship between its salinity and melting temperature), our models are the same. This allows us to contrast our dynamic-salinity model with CICE, as a fixed-salinity model, independently of additional differences such as in numerical method.

The standard option in CICE is to use a self-similar fixed-salinity profile

$$S_i(\zeta) = 0.5 \times 3.2 \left[1 - \cos\left(\pi \zeta^{0.407/(\zeta+0.573)}\right)\right], \tag{8.3}$$

where $\zeta = z/h$, for calculating the thermal properties of sea ice using equations (8.1, 8.2). For ice–ocean salt exchange, it uses a constant reference salinity $S_i = 4$ ppt.

8.1.3 Comparison with some alternative parameterizations of gravity drainage

Version 4.1 of CICE does not feature any representation of gravity drainage and this has prompted considerable recent interest and progress. Here, we give a detailed comparison with the two most similar proposals by Turner *et al.* (2013) and Griewank & Notz (2013), one of which (Turner *et al.*, 2013) is incorporated as an option in the next version of CICE (version 5).

Independently, these authors have developed parameterizations of gravity drainage that involve a Rayleigh number. There are several important differences compared to our proposal. Our single instantaneous effective Rayleigh number captures the non-local nature of convection arguably better than the more local 'rapid mode of gravity drainage' in Turner *et al.* (2013) and 'convective' parameterization in Griewank & Notz (2013), since it applies to the whole flow and means that the velocity at a given depth is related to the velocity everywhere within the convecting layer, consistent with the detailed calculations from which our model is derived. By contrast the other proposals amount to adding up a

series of locally driven flows, which may have some negative features. For example, Griewank & Notz (2013) may be prone to underestimating the desalination of lower regions of ice, since in their parameterization, the brine flux (implicitly vertical velocity) would not increase with z there. Likewise, the decision to moderate the velocity in terms of a local Rayleigh number in Turner *et al.* (2013) would also typically underestimate the desalination of the lower regions of the ice, since the local Rayleigh number approaches zero at the ice–ocean interface. In Turner *et al.* (2013), the fact that w is allowed to be non-zero at $z = 0$ can lead to excessive desalination near the top of the ice. A non-zero w at $z = 0$ is also inconsistent with the propagation of dye fronts discussed in section 6.5. Thus these alternative parameterizations may implicitly cause unreasonable features in the vertical structure of the velocity field w, and hence in the salinity profile.

For example, the C-shaped salinity profiles, as are commonly observed in first-year ice, and elevated near-surface salinities in our model (for example in figure 7.4*b*) arise because $w = 0$ at $z = 0$ in equation (7.5), in contrast to Turner *et al.* (2013). This has the potential to affect surface melting in periods of warming.

Furthermore, our model is entirely derived from fundamental physical models, and avoids relying on other mathematical descriptions that are not obviously physically motivated, such as the 'simple model' used as a stand-alone parameterization in Griewank & Notz (2013) and the 'slow mode of gravity drainage' used as an additional part of the parameterization in Turner *et al.* (2013). These extend (in different ways) a simple relaxation scheme for gravity drainage (Vancoppenolle *et al.*, 2009*a*).

In light of the critique by Turner *et al.* (2013) of Wells *et al.* (2010, 2011, 2013), we note that both the model of Wells *et al.* (2010, 2011, 2013) and our own CAP model consider the flow and viscous dissipation in the brine channel, and are more complete calculations in that they determine, rather than prescribe, the channel width, which depends on, for example, the strength of convection, as shown in equation (4.38).

In determining the growth rate of sea ice through equation (7.15), we differ significantly from Turner *et al.* (2013) in that they treat the solid fraction at the interface as a tuning parameter that they adjust to match ice-thickness data.

8.2 Definition of salt flux in sea-ice modelling

Fluxes of a quantity are only properly defined with respect to a reference value of that quantity. For example, measurements of salt fluxes from the Arctic Basin depend on the choice a relevant reference salinity (*e.g.* Aagaard & Carmack, 1989). Often various choices of definition could be made; however, a good definition will strengthen physical insight. Here we clarify the appropriate definition of salt flux relevant to sea-ice modelling. In doing so we discuss the definition used in CICE. We are not correcting any mistake; if alternative definitions are properly interpreted, they may be used. Nor is our definition novel. However, there is a need for clarity.

8.2.1 Treatment of salt fluxes in CICE

We firstly report how salt fluxes are described in the documentation of version 4.1 of CICE: the Los Alamos Sea Ice Model (Hunke & Lipscomb, 2008). In section 2.2, 'Ocean,' referring to the single-layer ocean used internally, the documentation reports:

> There is a flux of salt into the ocean under melting conditions, and a (negative) flux when sea water is freezing. However, melting sea ice ultimately freshens the top ocean layer, since the ocean is much more saline than the ice. The ice model passes the net flux of salt F_S to the flux coupler, based on the net change in salt for ice in all [ice-thickness] categories. In the present configuration, S_{i0} [a parameter called ice_ref_salinity, which is given a value 4 ppt] is used for computing the salt flux, although the ice salinity used in the thermodynamic calculation has differing values in the ice layers.

The index of variables also reports that F_S has units kg/m^2/s, *i.e.* the dimensions of a mass of salt transported per unit area per time.

We secondly consider the source code. Schematically, the 'ice_therm_vertical' module of CICE, version 4.1 (Lipscomb *et al.*, 2008), determines F_S as follows. It first calculates the total change in the thickness of the ice δh over one time step

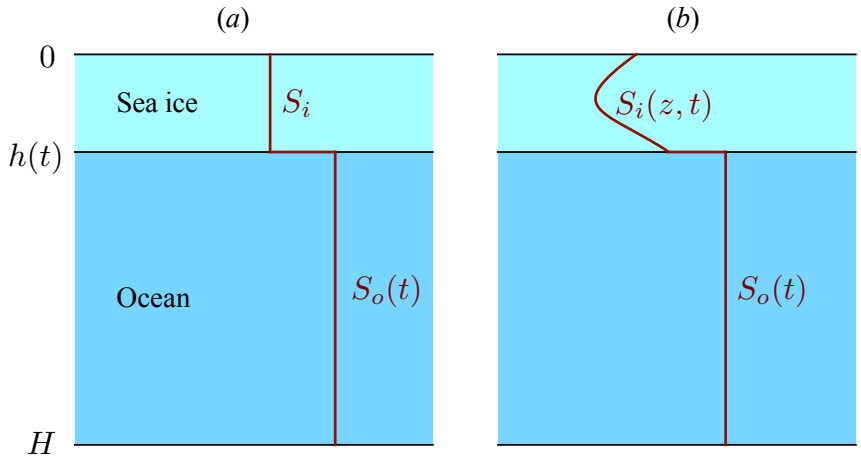

Figure 8.1: Box model of salt fluxes from sea ice with (a) uniform, steady ice salinity and (b) arbitrary ice salinity. We have included the possibility of a discontinuity at the ice–ocean interface.

δt and then computes the salt flux:

$$F_S = -0.001\rho_i \frac{\delta h}{\delta t} S_{i_0}, \tag{8.4}$$

where $S_{i0} = 4$ ppt is a constant reference salinity used in calculating ice–ocean salt exchange. The factor 0.001 converts units appropriately, since 1g of salt dissolved in 1000g of water has a salinity of 1 ppt and ρ_i is the density of pure ice. In the full model, this calculation is performed on each ice-thickness category and then the net salt flux is determined as a weighted mean over the whole grid box.

8.2.2 Salt fluxes from a global conservation equation

We consider a minimal box model, as shown in figure 8.1*a*. A liquid ocean of uniform salinity $S_o(t)$ lies between $h(t) < z < H$ and sea ice of steady, uniform salinity S_i lies between $0 < z < h(t)$. The vertical coordinate z points downward from ice to ocean, consistent with our sign convention that a positive salt flux is from ice to ocean. It is convenient for the purposes of this section to change units. Thus we use S, with various subscripts, to denote various *salt densities*, i.e. having units kg/m^3, not ppt.

The total mass of salt in the ocean and ice are, respectively,

$$M_o(t) = [H - h(t)]S_o(t), \qquad M_i(t) = h(t)S_i. \tag{8.5}$$

Since the total mass of salt is conserved in the ice–ocean system,

$$\frac{dM_o}{dt} = -\frac{dM_i}{dt} = -\dot{h}S_i. \tag{8.6}$$

This expression for $\dot{M}_o$ corresponds exactly to the definition (8.4) for F_S given in the CICE documentation, since we have changed units so $S_i = 0.001\rho_i S_{i0}$. Therefore, we can interpret the CICE definition as describing the partitioning of salt between two domains. It has nothing to do with what we might call dynamic salt flux. So in particular, in the extreme example of growing pure sea ice ($S_i = 0$), then the CICE definition would give zero salt flux!

However, we also have

$$\frac{dM_o}{dt} = -\dot{h}S_o + (H - h)\dot{S}_o \quad \Rightarrow \quad (H - h)\dot{S}_o = \dot{h}\left(S_o - S_i\right). \tag{8.7}$$

Therefore, we define the dynamic salt mass flux

$$F_{S\,\mathrm{dyn.}} \equiv \dot{h}\left(S_o - S_i\right) = (H - h)\dot{S}_o. \tag{8.8}$$

The expression $\dot{h}\left(S_o - S_i\right)$, the definition, can be interpreted physically as segregation across the ice–ocean interface (*cf.* Tiller *et al.*, 1953). This leads to a simple interpretation of dynamic salt flux for this simple case of constant-salinity ice: the salt flux to the ocean is the amount of salt segregated at the ice–ocean interface. In this case, the flux is simply proportional to the growth rate of the ice (equation 8.8). Note that this conclusion is drawn from a simple box model of sea ice in which its salinity is constant and there is a discontinuity in the salinity field across the ice–ocean interface. This does not mean segregation is a physical mechanism of sea-ice desalination.

In the growth season, $\dot{h} > 0$ so salt flux as defined by CICE (equation 8.4) is negative, as stated in the CICE documentation (*cf.* our section 8.2.1). This highlights that the counter-intuitive sign of salt flux in CICE arises from choosing

an inappropriate definition. By contrast, our definition of dynamic salt flux is clearly positive in the winter growth season (equation 8.8, since the ocean salinity S_o is greater than the ice salinity S_i).

In CICE, F_S is the rate at which the mass of salt in the *remaining* ocean changes; whereas, in our definition, F_S is the rate at which salt is excluded from the growing ice. We have shown that these definitions are not the same. The expression $(H - h)\dot{S}_o$ in equation (8.8) is more oceanographically important, because it is directly proportional to the buoyancy flux, which forces convection in the ocean. Since h is very much smaller than H, this term tells us how fast the ocean salinity changes.

8.2.3 Generalization to an arbitrary salinity profile

The salinity profile of sea ice evolves, so in general we take $S_i = S_i(z, t)$. However, we can still use global salt conservation in a box model (shown in figure 8.1*b*) to define the dynamic salt flux. Thus

$$0 = \frac{d}{dt}\left[\int_0^h S_i(z,t)\,dz + \int_0^h S_o(t)\,dz\right] \tag{8.9}$$

$$= \int_0^h \frac{\partial S}{\partial t}\,dz + \dot{h}S_i(h,t) + (H-h)\frac{dS_o}{dt} - \dot{h}S_o. \tag{8.10}$$

By analogy with the constant salinity box model, this leads us to define the dynamic salt mass flux in general:

$$F_{S\,\mathrm{dyn.}} \equiv \dot{h}\Delta S - \int_0^h \frac{\partial S}{\partial t}\,dz = (H-h)\frac{dS_o}{dt}, \tag{8.11}$$

where $\Delta S = S_o(t) - S_i(z = h, t)$ is the salinity jump across the ice–ocean interface. The first expression is best taken as the definition, hence our equation (7.18). The second expression is then used to update the salinity of the ocean, hence our equation (7.19).

For the special case of self-similar salinity profile $S_i(z, t) = \tilde{S}(\zeta)$, where $\zeta = z/h$, (including equation (8.3) used in the CICE thermodynamic calculation, but

not for calculating salt fluxes), we find that the salt flux

$$F_{S\,\mathrm{dyn.}} = \dot{h}\left(S_o - \overline{S}\right), \tag{8.12}$$

where $\overline{S} = \int_0^1 \tilde{S}(\zeta)\,d\zeta$, the average salinity of the sea ice. Note that a numerical integration gives $\overline{S} = 2.3$ ppt for the CICE profile. This value is lower than the 4 ppt used in calculating the salt flux (see section 8.2.1, a discrepancy that is acknowledged in the CICE documentation). Comparing equation (8.12) with (8.8) shows that, a self-similar salinity profile gives the same solute flux as a uniform profile of the average salinity.

Again, our definition has a simple physical interpretation: salt flux from sea ice is the sum of segregation at the ice–ocean interface and the total change in the internal salinity of the ice. Two examples – gravity drainage and basal melt – illustrate the physical sense of this definition.

In growing ice, processes such as gravity drainage reduce the internal salinity ($\partial S/\partial t < 0$). As in section 7.2.4, the bulk salinity field is continuous across the ice–ocean interface, so $\Delta S = 0$. Therefore

$$F_{S\,\mathrm{dyn.}} = \int_0^h -\frac{\partial S}{\partial t}\,dz, \tag{8.13}$$

so there is a positive salt flux to the ocean, raising its salinity.

In basal-melting ice, $\dot{h} < 0$ but $\Delta S > 0$. If we neglect changes to the internal salinity, then

$$F_{S\,\mathrm{dyn.}} = \dot{h}\Delta S, \tag{8.14}$$

so there is a negative salt flux to the ocean, freshening it.

In conclusion, this section offers a brief explanation of the appropriate definition of salt fluxes in climate model and justifies our choice in section 7.2.4. The CICE definition represents the rate of change of the mass of salt in the ocean, whereas our definition represents the rate of change of the salinity of the ocean.

8.3 Comparison of model predictions with CICE

8.3.1 Laboratory-experiment calculations

We first compare models with laboratory experiments to assess their effectiveness. It is important to note that CICE was not designed to simulate small-scale experiments in which the sea ice is relatively salty and formed under largely quiescent conditions, whereas, in the ocean, the first few centimetres of sea ice are often formed under turbulent conditions (Weeks, 2010). Nevertheless the comparison proves an instructive starting point because we can compare the underlying thermodynamics of growth. We initially use the standard CICE fixed-salinity profile (equation 8.3) for calculating thermodynamic growth. For ice–ocean salt exchange, we use a constant reference salinity $S_i = 4$ ppt. Together, this is the default CICE option (CICE–def), as discussed in section 8.1.2. We later consider the effect of using uniform salinities $S_i = 4$ ppt (CICE–4) and $S_i = 25$ ppt (CICE–25) for both thermodynamic and ice–ocean salt exchange calculations. The latter is the average ice–salinity after 30 hours in the experiment of figure 8.2.

For a fixed cold-plate temperature, all the models do a reasonable job of predicting sea-ice thickness (figure 8.2a), but this is only because growth depends weakly on salinity (section 8.4.1), with a progressively worse agreement for low ice salinity. Indeed for the very desalinated profiles typically used in CICE, the under prediction is 5–10%. We show below (section 8.4.2) that CICE is principally sensitive to salinity through changes to the ocean salinity, so much of this discrepancy is explained by the very large over prediction of ocean salinity (figure 8.2b).

Ocean salinity is a proxy for salt fluxes to the ocean, so the over prediction of ocean salinity in the CICE calculations corresponds to an over prediction of the initial salt flux, which arises from excessively high brine rejection at the ice–ocean interface. Although it is possible to choose a value of the ice salinity S_i to match an experimental result of ocean salinity at a given time, CICE predictions are fundamentally inconsistent with the evolution of the salinity. Note that the CICE–def and CICE–4 profiles give indistinguishable predictions. This suggests

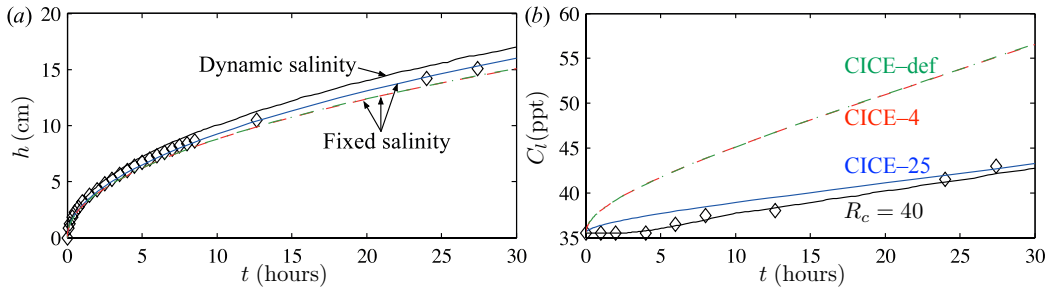

Figure 8.2: Experimental results of Wettlaufer *et al.* (1997*a*) at fixed $T_B = -20°\text{C}$ (diamonds) compared to predictions of our dynamic-salinity model (solid black curve) and fixed-salinity models at uniform CICE–25 (solid blue curve), CICE–4 (dashed red curve) and the default CICE–def (dot-dashed orange curve).

that using depth-dependent salinity profiles does not affect the initial growth of sea ice, although for late times the salinity at the interfaces matters. We also tested the variable cold-plate temperature scenario of section 7.3.5, which had a similar pattern of discrepancies, which were slightly greater, suggesting that our dynamic-salinity model copes better with varying heat fluxes (*cf.* figure 8.5*b*).

In conclusion, the differences in predictions of sea-ice thickness are relatively small and have a similar magnitude to the uncertainties in experiments and material properties. However, the differences in predictions of salt fluxes are large and systematic. Therefore, the greater success of our dynamic-salinity model strongly suggests that it would improve the representation of salt fluxes into the polar oceans.

8.3.2 Deep-ocean calculations

Results for solidification into a deep ocean (mixed layer) are arguably more important than into a tank. However, lacking sufficient experimental data to assess which model is superior, in this section we show that our dynamic-salinity model gives substantially different predictions of ice growth and discuss possible implications for climate models.

To compare models, we assume the ocean is very deep and hence that its temperature $T_l = -1.9°\text{C}$ and salinity $C_l = 35.5$ ppt are constant. This is an considerable idealization compared to typical mixed layers in the Arctic ocean,

which evolve significantly. These conditions impose a constant ocean heat flux of 2.25 W/m^2. Thus we explicitly neglect changes to the salinity of ocean (which would otherwise cause further differences between models in terms of ice growth). A more detailed ocean model is needed to assess these feedbacks properly.

Initially, our dynamic-salinity model predicts greater growth than in CICE, as shown in figure 8.3*a*. This is exactly as we found in our tank experiments. The variation with ice salinity observed is caused by the change in physical properties (*cf.* section 8.4.1).

However, after longer periods (several weeks), this trend is reversed and the CICE model predicts greater growth than our dynamic-salinity model. At late times, growth depends dominantly on the thermal conductivity near the ice–ocean interface (*cf.* section 8.4.3). In our dynamic model, this is always equal to the conductivity of the liquid phase (since $\phi = 0$ at the interface, independent of, say, the mean ice salinity) whereas in a fixed-salinity model (in which $\phi > 0$ at the interface) the conductivity will always be higher. Therefore, our model's continuous bulk salinity profile at the ice–ocean interface makes a measurable difference to predictions. In practice, the effect of thermal conductivity would need to be considered alongside the effect of high-frequency forcing and snow cover.

The difference in sea-ice thickness is in addition to the difference between the models in average sea-ice salinity (figure 8.3*b*), which is a measure of the total salt flux into the ocean. Note that the predicted salinities in our model are rather high for first-year ice (Weeks, 2010), even for the smaller values of R_c suggested by the experiments of (Notz, 2005), which is partly a consequence of our constant atmosphere temperature. In reality, periods of warming and solar radiation would result in a lower solid fraction and hence a more permeable mushy layer that could desalinate further, as was observed in the simulations of Turner *et al.* (2013) and Griewank & Notz (2013) with realistic forcing.

8.4 Physical mechanisms affecting ice growth

In order to justify the explanations made previously, we now present simplified calculations at fixed, uniform ice salinity S_i, used in both the thermodynamic

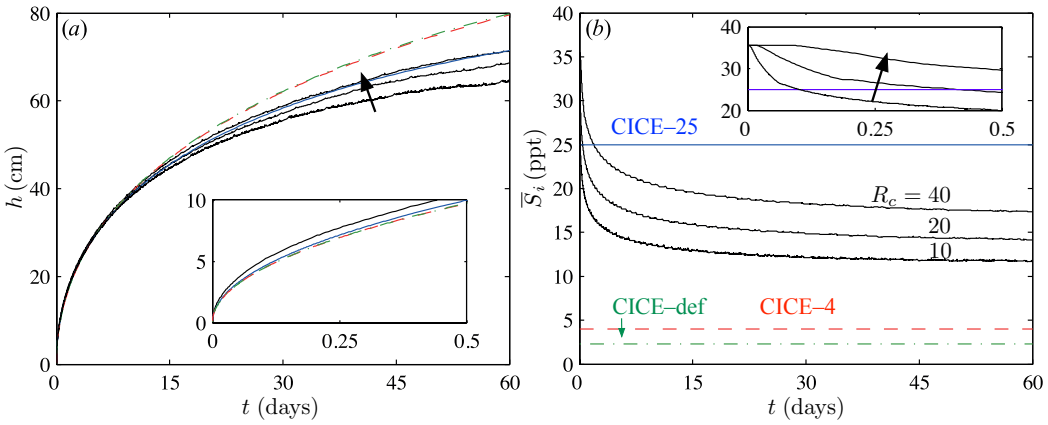

Figure 8.3: Comparison between fixed and dynamic-salinity models for a deep ocean at constant $T_B = -20°\mathrm{C}$, $T_l = -1.9°\mathrm{C}$ and $C_l = 35.5$ ppt. Note the much longer time scale compared to previous figures. We additionally include model calculations with $R_c = 20$ and $R_c = 10$, except in the inset for (a), which are indicated by an arrow in the direction of increasing R_c and labelled in (b). This compensates for the fact that the processed laboratory measurements of Wettlaufer *et al.* (1997*a*) that suggest $R_c = 40$ may overestimate the ice salinity. The insets show initial 12 hours (0.5 days) including the delayed onset of convection in our dynamic-salinity model.

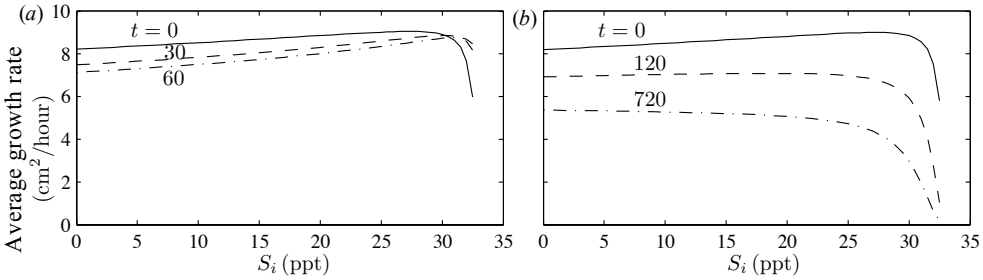

Figure 8.4: CICE calculation of sea-ice growth into (a) a tank of depth 37.6 cm and (b) a deep ocean, with $T_B = -20°\mathrm{C}$, as a function of fixed, uniform ice salinity S_i. The growth rate decreases over time (labelled in hours). The common $t = 0$ curve would apply for all times if heat and salt fluxes to the ocean were neglected. The rapid decrease at large S_i is caused by the CICE expression for the thermal conductivity of ice dropping to zero (*cf.* equation (8.2) and discussion there).

and ice–ocean salt exchange calculation. We separate the effects of variation in the thermodynamic properties with S_i and changes to the environment over time, which also depends on S_i indirectly through salt fluxes.

8.4.1 Effect of the thermodynamic properties of ice

More saline ice has a lower solid fraction and so has a lower thermal conductivity. However, there is also less latent heat of solidification, which counterbalances the decrease in conductivity. We analyze this balance systematically by considering an infinitely deep tank and neglecting the heat flux from the tank.

In the solid $t = 0$ curve in figure 8.4a (which is the same in figure 8.4b), we show that the average growth rate, measured in cm^2/hour to reflect the fact that the growth of ice is exactly diffusive in this scenario, depends only very weakly on the prescribed salinity of the ice. Indeed, this scenario can be analyzed asymptotically and this asymptotic analysis shows that this graph is representative of a wide class of similar situations in which the thermal properties of a material vary with salinity. In particular, the weak increase in growth rate with increasing salinity is generic across the entire range of T_B relevant to sea-ice formation. Therefore, vertical salinity variation is not particularly important for the growth rate of first-year ice. Our analysis constitutes a general explanation of this effect

noticed for first-year ice by Vancoppenolle *et al.* (2005) and observed by Griewank & Notz (2013) in their calculations.

8.4.2 Effect of changing ocean salinity over time

In a finite tank, using a lower ice salinity for the ice–ocean salt exchange means that the ocean becomes more saline over time because there is more segregation at the interface. This depresses the freezing temperature of the ocean T_L (C_l), which is the temperature of the ice–ocean interface, and thereby reduces the temperature difference across the sea ice. The reduction decreases the conduction of heat across the ice and causes slowing growth rates over time as shown in figure 8.4*a*. Thus the dependence on ice salinity caused by changes to the physical properties of ice is still present, but at later times that effect is dominated by changes to the ocean salinity.

8.4.3 Effect of prescribed heat flux from the ocean

We prescribe a fixed heat flux and salinity of the ocean. The situation here is more complex: at early times, the results of section 8.4.1 apply, but at late times the heat flux from the ocean will always be significant and balanced by the conductive heat flux from the relatively warm ocean. This balance gives a steady-state thickness

$$h \sim k_i(z = h)\Delta T/F_T. \tag{8.15}$$

Although a steady state is certainly not achieved in (say) 30 days of growth, the balance of fluxes represented by equation (8.15) is nevertheless important over this timescale. Conversely, latent heat is somewhat less important. Therefore, the dependence of the thermal conductivity near the ice–ocean interface on salinity determines the growth rate: k_i decreases with S_i (equation 8.2, reflecting the fact that more saline ice has a lower solid fraction) so h decreases with S_i. Since the steady-state thickness is lower for higher S_i, the average growth rate at sufficiently late times must also must also be lower, as shown in figure 8.4*b*. The trend is only enhanced at later times (figure 8.3). Note that although this effect was reported in terms of the bottom growth by Vancoppenolle *et al.* (2005) for multi-year ice

at a few values of S_i, in their calculations the effect was more than counteracted by changes in surface melting, which we do not consider in our test calculations. This suggests that our dynamic-salinity model will cause additional differences when the ice starts to melt in the summer.

8.5 Conclusions

The treatment of the thermodynamics of sea-ice growth in our one-dimensional model is based on mushy-layer theory, accounting for a nonlinear liquidus relationship, and is a consistent new development of previous sea-ice models such as CICE. Our model can be solved with a variety of boundary conditions; in particular, the atmospheric and ocean heat fluxes ocean can be imposed. Thus our model could be incorporated into a coupled climate model.

The definition of salt fluxes used in such models needs to be chosen consistently between sea ice and ocean components. We showed that the definition used in CICE represents the rate of change of the total mass of salt in the ocean, which counterintuitively is negative when sea ice grows and is not intrinsically important. Therefore, we propose a definition of dynamic salt flux that represents how the salinity of ocean changes due to changes in the salinity of sea ice caused by, for example, convective desalination. Such a definition is particularly important if our dynamic-salinity model is to be used.

We have assessed the likely direct, physical implications of using our dynamic-salinity model in coupled climate models in terms of thermal considerations that affect sea-ice thickness and salt fluxes that affect ocean salinity. We showed that our dynamic parameterization of ice salinity causes some differences from established, fixed-salinity models in terms of predicted ice thickness and much more significant differences in terms of the qualitative pattern and quantitative magnitude of salt fluxes (shown in figure 8.5).

The insensitivity of sea-ice thickness to salinity is an important feature that we were able to explain systematically in terms of the competition between latent heat release and ice conductivity. However, secondary effects through salinity affecting thermal conductivity and hence surface and basal melting in warmer periods may still cause greater sensitivity in some situations.

By contrast, salt fluxes are very sensitive to calculations of sea-ice salinity. Prescribing a low sea-ice salinity when calculating ice–ocean salt exchange in climate models is equivalent to predicting an excessive salt flux due to segregation at the interface and is inappropriate for thinner, first-year ice. Thus accounting for salt transport reduces salt fluxes, consistent with the pattern found in previous studies (*e.g.* Vancoppenolle *et al.*, 2009*b*).

We have presented the different predictions between older, fixed-salinity model and our new dynamic-salinity model in a number of ideal, but representative, scenarios. The physical basis of our model, which allows it to account for important dynamical feedbacks, and the success of our model in predicting laboratory experiments in chapter 7 gives us reason to expect that it should be more successful in predicting salt fluxes in climate models. Therefore, we expect that our parameterization should improve the predictive capabilities of sea-ice models, making them more robust to climate change and more responsive to short-term variability in external forcing.

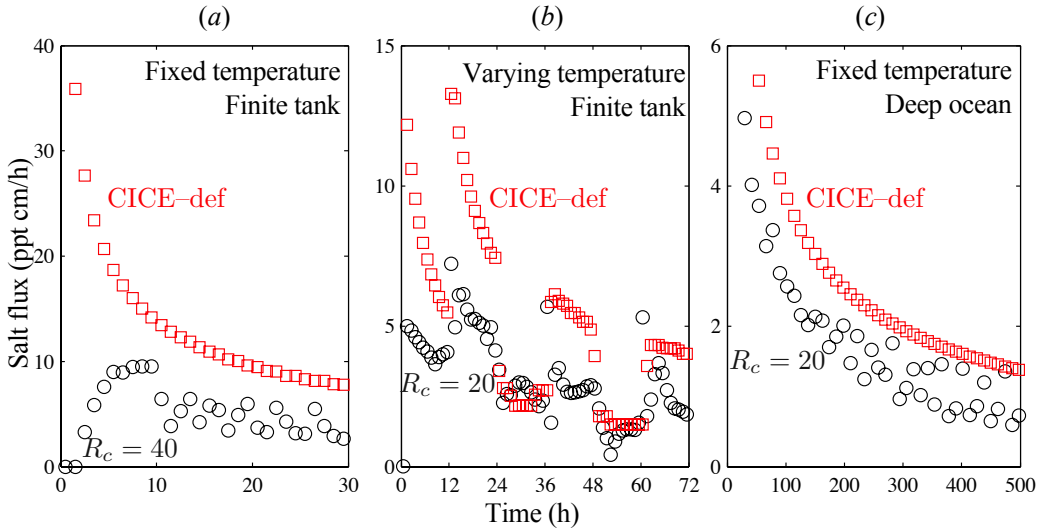

Figure 8.5: Comparison between a fixed-salinity (CICE-def, red squares) and our dynamic-salinity model (black circles) of predicted salt fluxes from sea ice. (a & c) provide an alternative interpretation of figures 8.2 & 8.3, respectively. (b) corresponds to the experiments in figure 7.10. We define the salt flux (relative to a reference salinity equal to the initial salinity of the ocean) as the rate of change with time of $(H-h)(C_l - C_0)$, or equivalently $h(C_0 - \overline{S}_i)$, and plot measurements averaged over an hour (a, b), and 12 hours (c). Note that the salt flux tends to infinity as t tends to zero for the CICE calculations and we have cropped this axis such that the first few points are removed to give a more reasonable scale for the rest of the measurements. The short-time variability in our model is usually associated with switches between full-depth and confined convection.

Chapter 9

Conclusions

Sea ice plays a crucial role in the climate, regulating the transfer of heat between the Earth's atmosphere and oceans, and causing massive fluxes of salt that drive mixing in the oceans. The dynamics of small-scale sea-ice processes can have a very significant, complex and nonlinear effect on the climate of the whole Earth.

The Earth's climate is changing, largely in response to anthropogenic greenhouse gas emissions. The Arctic is particularly sensitive and there have already been marked changes in the extent and age of its sea ice, with a transition from largely multi-year ice to predominantly first-year ice. In chapter 2, we showed how the observed and predicted changes raise important modelling challenges since many basic physical processes associated with sea ice are poorly understood, particularly those associated with first-year ice. The widespread use of prescribed salinity profiles that are more appropriate to multi-year than first-year ice, and the poor representation of salt fluxes from sea ice, are particularly problematic. This led us to study the convective desalination of sea ice, so that the salinity profiles of sea ice and salt fluxes to the ocean could be determined dynamically within a climate model.

Therefore, we used a general theory of mushy layers, which are reactive porous media, to describe convective desalination mathematically. In chapter 3, we developed general continuum equations to describe conservation of heat, salt, mass and momentum within mushy layers, such as sea ice, relevant to a number of different situations. This chapter developed a general theory rather than one specific to sea ice, which means that the models and results derived subsequently

can be applied to other mushy layers, for example those that form in the casting of metal alloys in industry and in the solidification of the Earth's inner core. The main new contribution of this section of our study was to clarify the thermodynamic and fluid dynamical boundary conditions at the interface between a porous mushy layer and a purely liquid region. One condition (marginal equilibrium) relevant to convection in mushy layers requires that lines of constant temperature (isotherms) are tangent to the fluid flow (streamlines) at the interface. However, many fluid dynamical conceptions of the boundary between a porous medium and a liquid region allow for a slip in the tangential velocity at the interface, such that there is no well-defined tangent to a streamline at the interface. This led us to explore the concept of a transition region, which we justified and illustrated in a simple, forced corner-flow configuration without resorting to the full convective mushy-layer equations. Our study highlighted the importance of a rapid change in the tangential velocity near the interface to satisfy the marginal equilibrium condition. In the corner-flow configuration, this change occurs in the transition region. In a convecting mushy layer, it occurs in the 'active region' near the chimney that we subsequently developed.

In chapter 4, we modelled convection in a mushy layer. We developed a simple Chimney-Active-Passive (CAP) model that elucidates analytically the dominant structure and driving forces of the flow. A horizontal density gradient within the mushy layer in an active region near a liquid chimney leads to baroclinic torque, which sustains the convective flow. In the passive bulk of the mushy layer, the isotherms are essentially horizontal. In this region, we imposed a vertically linear temperature field and found that the flow field is a simple corner flow. We determined the strength of the flow by finding a scaled solution to the governing mushy-layer equations in the active region. We also determined the corresponding shape of the chimney, the vertical structure of the solid fraction and the interstitial flow field. We applied this model firstly to a periodic, planar array of chimneys and showed analytically that the solute flux through the chimneys is proportional to a mush Rayleigh number. Secondly we extended the model to three dimensions and found that an array of chimneys can be characterized by the average drainage area alone. Therefore we solved the model in an axisymmetric geometry and found new, sometimes nonlinear, relationships between the solute

flux, the Rayleigh number (which is the ratio of the driving gravitational force to the dissipative forces acting on the flow) and the other dimensionless parameters of the system. The crucial difference between planar and axisymmetric geometries is that, in the latter case, the width of the chimney is important to the dynamics of the fluid flow by means of geometric constriction in the mushy layer. This means that the Darcy number, which is the dimensionless permeability of the mushy layer, affects the solute flux. By contrast, in the planar geometry the solute flux is, to leading order, independent of the Darcy number. Thus there is an additional lengthscale to the problem in axisymmetry, which gives rise to nonlinear relationships between solute flux and Rayleigh number.

Departing slightly from the main direction of the thesis, in chapter 5 we made a series of mathematical insights into convection in mushy layers and the CAP model in particular. We demonstrated the inadequacy of reduced models that effectively consider an isolated chimney and a boundary layer in an unbounded domain by showing that the boundary-layer equations (which are analogous to the equations governing the active region) have an infinite family of unstable solutions. The instability is driven by the unstable density profile in the far field. In contrast to the infinite family of both monotonic and oscillatory solutions to the boundary-layer equations, solutions of the active-region equations are all oscillatory (possessing the rapid change in tangential velocity near the chimney that we showed was necessary to satisfy the marginal equilibrium condition in chapter 3). In the limit of an infinite active region, these solutions tend to a critical monotonic solution identified in the boundary-layer analysis. We also showed why a bounded active region is essential to sustaining the convective flow by analyzing the mathematical structure of the governing boundary-value problem for the active region using asymptotic analysis, showing that there is a minimum width of the active region required to sustain convection. We then studied the asymptotic limit of large latent heat release in which convection becomes weak. This chapter gives important new physical insight into convection in mushy layers.

This first, more theoretical, half of the thesis raises a number of questions concerning convection in a mushy layer. In the planar geometry, we could compare our simple model with numerical solutions of the mushy-layer equations: they share the same structure and many features. However, there are currently

no comparable numerical solutions in axisymmetry (or three dimensions). Given the nonlinear relationships that we found between solute flux and Rayleigh number caused by geometric constriction of the flow, this could be an interesting area for future research. The numerical solution of our governing equations is only moderately more challenging in the axisymmetric geometry than in the planar geometry, so this seems entirely feasible. Furthermore, the contrasting dependence on the Darcy number between the two geometries could potentially be investigated in the asymptotic limit of small Darcy number. Our initial investigation of this issue suggests that in the planar geometry the size of the chimney tends to zero in such a way that the solute flux remains finite whereas in the axisymmetric geometry both the chimney size and solute flux tend to zero. Finding these scalings within numerical solutions would increase our confidence in their robustness. These investigations would further our theoretical understanding of convection in a mushy layer and clarify the appropriateness of using the results from the planar geometry in modelling convection. It might also be possible to parameterize the effects of geometric constriction as a function of the dimensionless parameters of the system, modifying the planar result to account for this potentially important effect.

The question as to what sets the horizontal size of the convecting region (chimney spacing) remains open. While we have used a maximum-flux criterion, this has limited explanatory power. The generic instability of the boundary-layer solutions that we found, coupled with their similarity to the CAP model at large chimney spacing, leads us to suspect that these large spacings may well be unstable to the formation of new chimneys. Therefore, investigating the stability characteristics of the CAP model may give some insight into the chimney spacing. Additionally, more developed versions of the numerical study of Katz & Worster (2008) in which the chimneys are allowed to evolve could also help to address this question.

Convective desalination through liquid brine channels (chimneys) is the dominant mechanism for the desalination of growing, first-year sea ice, in which the mechanism is also called gravity drainage. In chapter 6, we compared it with other mechanisms to demonstrate this. Then we described and determined mathematically the essential physics of gravity drainage using the CAP model. In this

context, the simplicity of the CAP model is a particular advantage over more complex approaches based on solving the mushy-layer equations numerically. We elucidated the connection between downward flow in brine channels and a convective upward flow in the rest of the porous ice, which we showed has a vertically linear structure and a strength proportional to a Rayleigh number based on the interstitial concentration difference across a convecting layer. This distinction is important because convection in sea ice is often confined to a layer at the bottom of the ice. We used our simple CAP model of this process to interpret the exponential propagation of dye fronts observed in previous laboratory experiments.

In chapter 7, we incorporated a physically derived parameterization of gravity drainage, in terms of the convective upwelling velocity determined in the previous chapter, into a one-dimensional, thermodynamic sea-ice model of the kind currently used in coupled climate models. Our parameterization uses a local Rayleigh number to represent the important feedback between ice salinity, porosity, permeability and desalination rate. It allows us to determine the evolution of the bulk salinity of the sea ice and the corresponding salt fluxes from it, in contrast to older, established models that prescribe the salinity of sea ice. This improves the predictive power of climate models in terms of buoyancy fluxes to the polar oceans, and also the thermal and mechanical properties of sea ice, which depend on its salinity. We tested our model against a series of laboratory experiments, analyzed the uncertainties involved in these, and showed that we could quantitatively predict bulk features of the experiments (the sea-ice thickness and a measure of the cumulative salt flux) to within experimental error. Some systematic biases in our predictions led us to propose changes to the relationship between porosity and permeability to be investigated in future research.

There has been considerable recent interest in gravity drainage from climate modellers, because it is a crucial missing component of sea-ice models. Therefore, in chapter 8, we compared our new parameterization of gravity drainage to the existing fixed-salinity sea-ice model used in CICE: the Los Alamos Sea Ice Model. Our study focused on growing first-year ice. We showed that the direct effect of salinity on sea-ice thickness was small. However, there were substantial differences compared to fixed-salinity models in the qualitative pattern and quantitative magnitude of salt fluxes into the polar oceans. Theoretically, we also clarified

the appropriate definition of salt fluxes for climate modelling and explained the weak dependence of sea-ice thickness on salinity in terms of the balance between latent heat release and the thermal conductivity of sea ice. In conclusion, we expect that our dynamic model of gravity drainage for sea ice, which respects the underlying physics of convective desalination, is likely to be more robust to changes in polar climate and more responsive to rapid changes in the oceanic and atmospheric conditions that drive the advance and retreat of sea ice.

This second, more applied, half of the thesis also raises several questions, principally about how such a model would interact with other components of a coupled climate model. While some modelling studies have shown that different parameterizations of salt fluxes from sea ice lead to differences in the predicted salinity structure of oceans, it is not yet known how the physically based parameterization that we have developed would affect the salinity structure through the significant changes to salt fluxes that we demonstrated in chapter 8. The salt fluxes in our model are a boundary condition for the ocean, but the complete response involves many nonlinear processes and requires a detailed understanding of ocean mixing, which is also not well understood. Furthermore, although we found that changes to sea-ice thickness were small, there may be additional sensitivity in terms of basal and surface melting caused by the dependence of thermal conductivity on salinity. Likewise, gravity drainage may interact with other mechanisms of desalination. For example, the brine channels associated with gravity drainage may facilitate more rapid desalination by flushing from meltponds that form in the summer. Our parameterization therefore needs to be assessed over a longer period than a few months of growth in the winter. Given both the similarity of our model to CICE, and the recent inclusion of an alternative parameterization of gravity drainage within CICE (version 5), it seems feasible to implement our model in CICE thereby allowing others to investigate its impact within the context of climate models.

The simulations that we performed were all conducted with rather idealized boundary conditions, both at the ice–atmosphere and at the ice–ocean boundary. Within the context of a one-dimensional scenario, it could be well be profitable to investigate these further. For example, a heat flux could be prescribed at the ice–atmosphere interface, or, more nonlinearly, its temperature could be used to

calculate the radiative heat flux from ice to atmosphere. Particularly for Antarctic sea ice, it would be interesting to investigate the effect of a snow layer. Likewise the temperature and salinity of the mixed layer change over the course of the growing season. All these effects could also be investigated using meteorological and oceanographic data to force our model (data which is often not available at the same location) or using synthetic forcings. It seems plausible that our dynamic-salinity model could cause greater changes compared to fixed-salinity models in these scenarios, and it is important to assess this.

In spite of these open questions, the developments made in modelling convective desalination in a mushy layer, applied to gravity drainage in sea ice, address a major missing component of climate models. They will cause direct changes to predictions of ocean circulation and indirect changes to predictions of atmospheric circulations. Therefore, these developments offer substantial improvements in our attempts to model the changing climate of the Earth.

References

Aagaard, K. & Carmack, E. C. 1989 The role of sea ice and other fresh water in the Arctic circulation. *J. Geophys. Res.* **94** (C10), 14485–14498.

Amberg, G. & Homsy, G. M. 1993 Nonlinear analysis of buoyant convection in binary solidification with application to channel formation. *J. Fluid Mech.* **252**, 79–98.

Ames, W. F. 1977 *Numerical Methods for Partial Differential Equations (2nd edn.)*. Academic.

Arndt, J. E. & Schenke, H. W. 2012 IBCSO version 1.0: The first release of the International Bathymetric Chart of the Southern Ocean. In *American Geophysical Union: Fall Meeting*. AGU.

Assur, A. 1958 Composition of sea ice and its tensile strength. In *Arctic sea ice*, pp. 106–138. U.S. Natl. Acad. Sci.

Aussillous, P., Sederman, A. J., Gladden, L. F., Huppert, H. E. & Worster, M. G. 2006 Magnetic resonance imaging of structure and convection in solidifying mushy layers. *J. Fluid Mech.* **552**, 99–125.

Batchelor, G. K. 1967 *An Introduction to Fluid Dynamics*. Cambridge University Press.

Batchelor, G K 1974 Transport properties of two-phase materials with random structure. *Ann. Rev. Fluid Mech.* **6** (1), 227–255.

Beckermann, C., Gu, J. P. & Boettinger, W. J. 2000 Development of a freckle predictor via Rayleigh number method for single-crystal nickel–base superalloy castings. *Metall. and Mat. Trans. A* **31** (10), 2545–2557.

Beckermann, C. & Wang, C.Y. 1995 Multiphase/-scale modeling of alloy solidification. In *Annual Reviews of Heat Transfer* (ed. C. L. Tien), vol. 6, pp. 115–198. Begell House.

Bennington, K. O. 1963 Some crystal growth features of sea ice. *J. Glaciol.* **4** (36), 669–688.

Bitz, C. M. & Lipscomb, W. H. 1999 An energy-conserving thermodynamic model of sea ice. *J. Geophys. Res.* **104** (C7), 15669–15677.

Boettinger, W. J., Warren, J. A., Beckermann, C. & Karma, A. 2002 Phase-field simulation of solidification. *Ann. Rev. Mater. Res.* **32** (1), 163–194.

Chen, C. F. 1995 Experimental study of convection in a mushy layer during directional solidification. *J. Fluid Mech.* **293**, 81–98.

Cheng, P. & Minkowycz, W. J. 1977 Free convection about a vertical flat plate embedded in a porous medium with application to heat transfer from a dike. *J. Geophys. Res.* **82** (14), 2040–2044.

Chung, C. A. & Worster, M. G. 2002 Steady-state chimneys in a mushy layer. *J. Fluid Mech.* **455**, 387–411.

Coachman, E. K. & Aagaard, K. 1974 Physical oceanography of Arctic and subarctic seas. In *Marine geology and oceanography of the Arctic seas* (ed. Y. Herman), pp. 1–72. Berlin; New York: Springer-Verlag.

Cokelet, E. D., Tervalon, N. & Bellingham, J. G. 2008 Hydrography of the West Spitsbergen Current, Svalbard Branch: Autumn 2001. *J. Geophys. Res.* **113** (C01006).

Comiso, J. C., Parkinson, C. L., Gersten, R. & Stock, L. 2008 Accelerated decline in the Arctic sea ice cover. *Geophys. Res. Lett.* **35** (1).

Conroy, D. & Worster, M. G. 2006 Mush–liquid interfaces with cross flow. Geophysical Fluid Dynamics Program report, Woods Hole Oceanographic Institute.

Copley, S. M., Giamei, A. F., Johnson, S. M. & Hornbecker, M. F. 1970 The origin of freckles in unidirectionally solidified castings. *Metall. Trans.* **1**, 2193–2204.

Cottier, F., Eicken, H. & Wadhams, P. 1999 Linkages between salinity and brine channel distribution in young sea ice. *J. Geophys. Res.* **104** (C7), 15859–15871.

Cox, G. F. N. & Weeks, W. F. 1975 Brine drainage and initial salt entrapment in sodium chloride ice. *CCREL Res. Rept.* **345**.

Cox, G. F. N. & Weeks, W. F. 1988 Numerical simulations of the profile properties of undeformed first-year sea ice during the growth season. *J. Geophys. Res.* **93** (C10), 12449–12460.

Davaille, A. & Jaupart, C. 1993 Transient high-Rayleigh-number thermal convection with large viscosity variations. *J. Fluid Mech.* **253**, 141–166.

Eicken, H. 1992 Salinity profiles of Antarctic sea ice: Field data and model results. *J. Geophys. Res.* **97** (C10), 15545–15557.

Eicken, H., Bock, C., Wittig, R., Miller, H. & Poertner, H.-O. 2000 Magnetic resonance imaging of sea-ice pore fluids: methods and thermal evolution of pore microstructure. *Cold Reg. Sci. Technol.* **31** (3), 207–225.

Eicken, H., Grenfell, T. C., Perovich, D. K., Richter-Menge, J. A. & Frey, K. 2004 Hydraulic controls of summer Arctic pack ice albedo. *J. Geophys. Res.* **109** (C08007).

Eide, L. I. & Martin, S. 1975 The formation of brine drainage features in young sea ice. *J. Glaciol.* **14**, 137–154.

Fearn, D. R., Loper, D. E. & Roberts, P. H. 1981 Structure of the Earth's inner core. *Nature* **292** (5820), 232–233.

Feltham, D. L. & Worster, M. G. 2000 Similarity solutions describing the melting of a mushy layer. *J. Crystal Growth* **208** (1–4), 746–756.

Feltham, D. L., Untersteiner, N., Wettlaufer, J. S. & Worster, M. G. 2006 Sea ice is a mushy layer. *Geophys. Res. Lett.* **33** (14).

Fowler, A. C. 1985 The formation of freckles in binary alloys. *IMA J. Appl. Maths* **35** (2), 159–174.

Freitag, J. 1999 Hydraulic properties of Arctic sea ice – implications for the small scale particle transport. *Rep. Polar Res.* **325**.

Gent, P. R. 2012 Coupled climate and earth system models. In *Climate Change Modeling Methodology: Selected Entries from the Encyclopedia of Sustainability Science and Technology* (ed. P. J. Rasch), chap. 2, pp. 5–30. Springer New York.

Golden, K. M., Eicken, H., Heaton, A. L., Miner, J., Pringle, D. J. & Zhu, J. 2007 Thermal evolution of permeability and microstructure in sea ice. *Geophys. Res. Lett.* **34** (16).

Griewank, P. J. & Notz, D. 2013 Insights into brine dynamics and sea ice desalination from a 1-D model study of gravity drainage. *J. Geophys. Res.*.

Harrison, J. D. 1965 Measurement of brine droplet migration in ice. *Journal of Applied Physics* **36** (12), 3811–3815.

Hills, R. N., Loper, D. E. & Roberts, P. H. 1983 A thermodynamically consistent model of a mushy zone. *Q. J. Mech. Appl. Mech.* **36** (4), 505–540.

Holland, M. M. & Bitz, C. M. 2003 Polar amplification of climate change in coupled models. *Climate Dyn.* **21** (3-4), 221–232.

Holland, M. M., Curry, J. A. & Schramm, J. L. 1997 Modeling the thermodynamics of a sea ice thickness distribution: 2. Sea ice/ocean interactions. *J. Geophys. Res.* **102** (C10), 23093–23107.

Holland, P. R. & Kwok, R. 2012 Wind-driven trends in Antarctic sea-ice drift. *Nature Geosci.* **5** (12), 872–875.

Holloway, G., Dupont, F., Golubeva, E., Häkkinen, S., Hunke, E. C., Jin, M., Karcher, M., Kauker, F., Maltrud, M., Morales Maqueda, M. A., Maslowski, W., Platov, G., Stark, D., Steele, M., Suzuki, T., Wang, J. & Zhang, J. 2007 Water properties and circulation in Arctic Ocean models. *J. Geophys. Res.* **112** (C4).

Hunke, E. C. & Lipscomb, W. H. 2008 CICE: The Los Alamos sea ice model user's manual, version 4. *Los Alamos National Laboratory Tech. Rep.* **LA-CC-06-012**.

Hunke, E. C., Notz, D., Turner, A. K. & Vancoppenolle, M. 2011 The multiphase physics of sea ice: a review for model developers. *Cryosphere* **5** (4), 989–1009.

Huppert, H. E. 1990 The fluid mechanics of solidification. *J. Fluid Mech.* **212**, 209–240.

Huppert, H. E. 2000 Geological fluid mechanics. In *Perspectives in Fluid Dynamics: a Collective Introduction to Current Research* (ed. G. K. Batchelor, H. K. Moffatt & M. G. Worster), pp. 447–506. Cambridge University Press.

Huppert, H. E. & Worster, M. G. 2012 Flows involving phase change. In *Handbook of Environmental Fluid Dynamics* (ed. H. J. Fernando), vol. 1, pp. 467–477. Taylor and Francis.

Hurrell, J. W., Holland, M. M., Gent, P. R., Ghan, S., Kay, J. E., Kushner, P. J., Lamarque, J. F., Large, W. G., Lawrence, D., Lindsay, K., Lipscomb, W. H., Long, M. C., Mahowald, N., Marsh, D. R., Neale, R. B., Rasch, P., Vavrus, S., Vertenstein, M., Bader, D., Collins, W. D., Hack, J. J., Kiehl, J. & Marshall, S. 2013 The Community Earth System Model: a framework for collaborative research. *Bull. Am. Met. Soc.*.

Jakobsson, M., Mayer, L., Coakley, B., Dowdeswell, J. A., Forbes, S., Fridman, B., Hodnesdal, H., Noormets, R., Pedersen, R., Rebesco, M., Schenke, H. W., Zarayskaya, Y., Accettella, D.,

Armstrong, A., Anderson, R. M., Bienhoff, P., Camerlenghi, A., Church, I., Edwards, M., Gardner, J. V., Hall, J. K., Hell, B., Hestvik, O., Kristoffersen, Y., Marcussen, C., Mohammad, R., Mosher, D., Nghiem, S. V., Pedrosa, M. T., Travaglini, P. G. & Weatherall, P 2012 The International Bathymetric Chart of the Arctic Ocean (IBCAO) version 3.0. *Geophys. Res. Lett.* **39** (12).

Jardon, F. P., Vivier, F., Vancoppenolle, M., Lourenço, A., Bouruet-Aubertot, P. & Cuypers, Y. 2013 Full-depth desalination of warm sea ice. *J. Geophys. Res.* **118** (1), 435–447.

Jeffery, N., Hunke, E. C. & Elliott, S. M. 2011 Modeling the transport of passive tracers in sea ice. *J. Geophys. Res.* **116** (C7).

Katz, R. F. & Worster, M. G. 2008 Simulation of directional solidification, thermochemical convection, and chimney formation in a Hele-Shaw cell. *J. Comp. Phys.* **227** (23), 9823 – 9840.

Kerr, R. C., Woods, A. W., Worster, M. G. & Huppert, H. E. 1990 Solidification of an alloy cooled from above. Part 1. Equilibrium growth. *J. Fluid Mech.* **216**, 323–342.

Kwok, R., Cunningham, G. F. & Pang, S. S. 2004 Fram Strait sea ice outflow. *J. Geophys. Res.* **109** (C1).

Lake, R. A. & Lewis, E. L. 1970 Salt rejection by sea ice during growth. *J. Geophys. Res.* **75** (3), 583–597.

Lange, N. A. & Forke, G. M. 1952 *Handbook of Chemistry*, 8th edn. Handbook Publ., Sandusky, Ohio.

Lapwood, E. R. 1948 Convection of a fluid in a porous medium. *Proc. Camb. Phil. Soc.* **44** (04), 508–521.

Le Bars, M. & Worster, M. G. 2006 Interfacial conditions between a pure fluid and a porous medium: implications for binary alloy solidification. *J. Fluid Mech.* **550**, 149–173.

Lighthill, M. J. 1953 Theoretical considerations on free convection in tubes. *Quart. J. Mech. Appl. Math.* **6** (4), 398–439.

Lipscomb, W. H., Bitz, C. M. & Hunke, E. C. 2008 CICE module: 'ice_therm_vertical', release 4.1.

Maksym, T. & Jeffries, M. O. 2000 A one-dimensional percolation model of flooding and snow ice formation on Antarctic sea ice. *J. Geophys. Res.* **105** (C11), 26313–26331.

Malmgren, F. 1927 On the properties of sea ice. In *The Norwegian North Polar Expedition with the 'Maud' 1918–1925* (ed. H. U. Sverdrup), vol. 1a, pp. 1–67. John Griegs Boktr., Bergen, Norway.

Maykut, G. A. & McPhee, M. G. 1995 Solar heating of the Arctic mixed layer. *J. Geophys. Res.* **100** (C12), 24691–24703.

Maykut, G. A. & Untersteiner, N. 1971 Some results from a time-dependent thermodynamic model of sea ice. *J. Geophys. Res.* **76** (6), 1550–1575.

Maykut, G. A. A. 1978 Energy exchange over young sea ice in the central Arctic. *J. Geophys. Res.* **83** (C7), 3646–3658.

McIntyre, M. E. 2000 On global–scale atmospheric circulations. In *Perspectives in Fluid Dynamics: a Collective Introduction to Current Research* (ed. G. K. Batchelor, H. K. Moffatt & M. G. Worster), pp. 557—624. Cambridge University Press.

Mullins, W. W. & Sekerka, R. F. 1964 Stability of a planar interface during solidification of a dilute binary alloy. *J. Appl. Phys.* **45**, 444–451.

Nakawo, M. & Sinha, N. K. 1981 Growth rate and salinity profile of first-year sea ice in the High Arctic. *J. Glaciol.* **27**, 315–330.

Neumann, G. 1966 *Principles of physical oceanography*. Englewood Cliffs, N.J.: Prentice-Hall.

Nguyen, A. T., Menemenlis, D. & Kwok, R. 2009 Improved modeling of the Arctic halocline with a subgrid-scale brine rejection parameterization. *J. Geophys. Res.* **114** (C11).

Niedrauer, T. M. & Martin, S. 1979 An experimental study of brine drainage and convection in young sea ice. *J. Geophys. Res.* **84** (C3), 1176–1186.

Nield, D. A. & Bejan, A. 2006 *Convection in Porous Media*. Springer.

Notz, D. 2005 Thermodynamic and fluid-dynamical processes in sea ice. Ph.D. thesis, University of Cambridge, Cambridge, U. K.

Notz, D. & Marotzke, J. 2012 Observations reveal external driver for Arctic sea-ice retreat. *Geophys. Res. Lett.* **39** (8).

Notz, D., Wettlaufer, J. S. & Worster, M. G. 2005 A non-destructive method for measuring the salinity and solid fraction of growing sea ice in situ. *J. Glaciol.* **51** (172), 159–166.

Notz, D. & Worster, M. G. 2006 A one-dimensional enthalpy model of sea ice. *Ann. Glaciol.* **44** (1), 123–128.

Notz, D. & Worster, M. G. 2008 In situ measurements of the evolution of young sea ice. *J. Geophys. Res.* **113** (C3).

Notz, D. & Worster, M. G. 2009 Desalination processes of sea ice revisited. *J. Geophys. Res.* **114** (C5).

Nowlin, W. D. & Klinck, J. M. 1986 The physics of the Antarctic Circumpolar Current. *Rev. Geophys.* **24** (3), 469–491.

Oertling, A. B. & Watts, R. G. 2004 Growth of and brine drainage from NaCl–H_2O freezing: A simulation of young sea ice. *J. Geophys. Res.* **109** (C4).

Ono, N. 1968 Thermal properties of sea ice, IV, Thermal constants of sea ice. *Low Temp. Sci.* **A26**, 329–349.

Ozbek, H., Fair, J. A. & Phillips, S. L. 1977 Viscosity of aqueous sodium chloride solutions from $0 - 150°$C. *Am. Chem. Soc. 29th Southeast Regional Meeting, Tampa, FL, November 9-11, 1971*.

Peppin, S. S. L., Aussillous, P., Huppert, H. E. & Worster, M. G. 2007 Steady-state mushy layers: experiments and theory. *J. Fluid Mech.* **570**, 69–77.

Perkin, R. G. & Lewis, E. L. 1984 Mixing in the West Spitsbergen Current. *J. Phys. Oceanogr.* **14** (8), 1315–1325.

Perovich, D. K 1996 The optical properties of sea ice. *CCREL Mon.* **96** (1).

Petrich, C., Langhorne, P. & Eicken, H. 2011 Modelled bulk salinity of growing first-year sea ice and implications for ice properties in spring. In *Proc. 21st Int. Conf. Port and Ocean Engineering under Arctic Conditions (POAC), Montreal, Canada*, pp. 1–10. POAC11–187.

Petrich, C., Langhorne, P. & Sun, Z. F. 2006 Modelling the interrelationships between permeability, effective porosity and total porosity in sea ice. *Cold Reg. Sci. Technol.* **44** (2), 131 – 144.

Phillips, O. M. 1991 *Flow and Reactions in Permeable Rocks*. Cambridge University Press.

Pringle, D. J., Eicken, H., Trodahl, H. J. & Backstrom, L. G. E. 2007 Thermal conductivity of landfast Antarctic and Arctic sea ice. *J. Geophys. Res.* **112** (C4).

Rees Jones, D. W. & Worster, M. G. 2013*a* Fluxes through steady chimneys in a mushy layer during binary alloy solidification. *J. Fluid Mech.* **714**, 127–151.

Rees Jones, D. W. & Worster, M. G. 2013*b* A simple dynamical model for gravity drainage of brine from growing sea ice. *Geophys. Res. Lett.* **40** (2), 307–311.

Rees Jones, D. W. & Worster, M. G. 2013*c* A physically based parametrization of gravity drainage for sea-ice modelling (submitted). *J. Geophys. Res.*

Ruddick, B.R. & Shirtcliffe, T.G.L. 1979 Data for double diffusers: Physical properties of aqueous salt-sugar solutions. *Deep Sea Research Part A. Oceanographic Research Papers* **26** (7), 775 – 787.

Saenz, Benjamin T. & Arrigo, Kevin R. 2012 Simulation of a sea ice ecosystem using a hybrid model for slush layer desalination. *J. Geophys. Res.* **117** (C5), C05007.

Schulze, T. P. & Worster, M. G. 1998 A numerical investigation of steady convection in mushy layers during the directional solidification of binary alloys. *J. Fluid Mech.* **356**, 199–220.

Schulze, T. P. & Worster, M. G. 1999 Weak convection, liquid inclusions and the formation of chimneys in mushy layers. *J. Fluid Mech.* **388**, 197–215.

Schulze, T. P. & Worster, M. G. 2005 A time-dependent formulation of the mushy-zone free-boundary problem. *J. Fluid Mech.* **541**, 193–202.

Screen, J. A. 2013 Influence of Arctic sea ice on European summer precipitation. *Environ. Res. Lett.* **8** (4), 041002.

Screen, J. A. & Simmonds, I. 2010 The central role of diminishing sea ice in recent Arctic temperature amplification. *Nature* **464** (7293), 1334–1337.

Semtner, A. J. 1976 A model for the thermodynamic growth of sea ice in numerical investigations of climate. *J. Phys. Oceanogr.* **6**, 379–389.

Slack, Glen A. 1980 Thermal conductivity of ice. *Phys. Rev. B* **22**, 3065–3071.

Sverdrup, H. U., Johnson, M. W. & Fleming, R. H. 1942 *The Oceans: Their Physics, Chemistry, and General Biology*. Prentice–Hall, New York.

Thomas, L. H. 1949 Elliptic problems in linear differential equations over a network: Watson scientific computing laboratory. *Columbia Univ., NY*.

Tietsche, S., Notz, D., Jungclaus, J. H. & Marotzke, J. 2011 Recovery mechanisms of Arctic summer sea ice. *Geophys. Res. Lett.* **38** (L02707).

Tiller, W.A, Jackson, K.A, Rutter, J.W & Chalmers, B 1953 The redistribution of solute atoms during the solidification of metals. *Acta Met.* **1** (4), 428–437.

Tiller, W. A. 1963 Migration of a liquid zone through a solid: Part I. *J. Appl. Phys.* **34** (9), 2757–2762.

Turner, A. K., Hunke, E. C. & Bitz, C. M. 2013 Two modes of sea-ice gravity drainage: A parameterization for large-scale modeling. *J. Geophys. Res.* **118** (5).

Untersteiner, N. 1968 Natural desalination and equilibrium salinity profile of perennial sea ice. *J. Geophys. Res.* **73** (4), 1251–1257.

Vancoppenolle, M., Fichefet, T. & Bitz, C. M. 2005 On the sensitivity of undeformed Arctic sea ice to its vertical salinity profile. *Geophys. Res. Lett.* **32** (16).

Vancoppenolle, M., Fichefet, T., Goosse, H., Bouillon, S., Madec, G. & Morales Maqueda, M. A. 2009*a* Simulating the mass balance and salinity of Arctic and Antarctic sea ice. 1. Model description and validation. *Ocean Model.* **27** (1—2), 33–53.

Vancoppenolle, M., Fichefet, T. & Goosse, H. 2009*b* Simulating the mass balance and salinity of Arctic and Antarctic sea ice. 2. Importance of sea ice salinity variations. *Ocean Model.* **27** (1–2), 54–69.

Vancoppenolle, M., Goosse, H., de Montety, A., Fichefet, T., Tremblay, B. & Tison, J.-L. 2010 Modeling brine and nutrient dynamics in Antarctic sea ice: The case of dissolved silica. *J. Geophys. Res.* **115** (C2).

Weast, R. C. 1971 *Handbook of Chemistry and Physics*, 52nd edn. Chemical Rubber Co., Cleveland, OH.

Weeks, W. F. 2010 *On Sea Ice*. University of Alaska Press, Fairbanks, AK.

Wells, A. J., Wettlaufer, J. S. & Orszag, S. A. 2010 Maximal potential energy transport: A variational principle for solidification problems. *Phys. Rev. Lett.* **105**, 254502.

Wells, A. J., Wettlaufer, J. S. & Orszag, S. A. 2011 Brine fluxes from growing sea ice. *Geophys. Res. Lett.* **38** (L04501).

Wells, A. J., Wettlaufer, J. S. & Orszag, S. A. 2013 Nonlinear mushy-layer convection with chimneys: stability and optimal solute fluxes. *J. Fluid Mech.* **716**, 203–227.

Wettlaufer, J. S., Worster, M. G. & Huppert, H. E. 1997*a* Natural convection during solidification of an alloy from above with application to the evolution of sea ice. *J. Fluid Mech.* **344**, 291–316.

Wettlaufer, J. S., Worster, M. G. & Huppert, H. E. 1997*b* The phase evolution of young sea ice. *Geophys. Res. Lett.* **24** (10), 1251–1254.

Wettlaufer, J. S., Worster, M. G. & Huppert, H. E. 2000 Solidification of leads: Theory, experiment, and field observations. *J. Geophys. Res.* **105** (C1), 1123–1134.

Whitman, W. G. 1926 Elimination of salt from sea-water ice. *Am. J. Sci. Ser. (5)* **11** (62), 126–132.

Widell, K., Fer, I. & Haugan, P. M. 2006 Salt release from warming sea ice. *Geophys. Res. Lett.* **33** (12).

Worster, M. G. 1986 Solidification of an alloy from a cooled boundary. *J. Fluid Mech.* **167**, 481–501.

Worster, M. G. 1991 Natural convection in a mushy layer. *J. Fluid Mech.* **224**, 335–359.

Worster, M. G. 1992*a* The dynamics of mushy layers. In *Interactive Dynamics of Convection and Solidification*, *NATO ASI Ser.* E219:113–38. Dordrecht: Kluwer.

Worster, M. G. 1992*b* Instabilities of the liquid and mushy regions during solidification of alloys. *J. Fluid Mech.* **237**, 649–669.

Worster, M. G. 1997 Convection in mushy layers. *Ann. Rev. Fluid Mech.* **29** (1), 91–122.

Worster, M. G. 2000 Solidification of fluids. In *Perspectives in Fluid Dynamics: a Collective Introduction to Current Research* (ed. G. K. Batchelor, H. K. Moffatt & M. G. Worster), pp. 393–446. Cambridge University Press.

Zhong, J.-Q., Fragoso, A. T., Wells, A. J & Wettlaufer, J. S. 2012 Finite-sample-size effects on convection in mushy layers. *J. Fluid Mech.* **704**, 89.

Zhu, J., Jabini, A., Golden, K. M., Eicken, H. & Morris, M. 2006 A network model for fluid transport through sea ice. *Ann. Glaciol.* **44** (1), 129–133.